UNIVERSITY OF LJUBLJANA
FACULTY OF MATHEMATICS AND PHYSICS
DEPARTMENT OF PHYSICS

Victor Guada

FALSE VACUUM DECAY WITH MULTIPLE SCALAR FIELDS

Doctoral thesis

ADVISER: Dr. Miha Nemevšek

Ljubljana, 2021

UNIVERZA V LJUBLJANI
FAKULTETA ZA MATEMATIKO IN FIZIKO
ODDELEK ZA FIZIKO

Victor Guada

RAZPAD LAŽNEGA VAKUUMA Z VEČ SKALARNIMI POLJI

Doktorska disertacija

MENTOR: Dr. Miha Nemevšek

Ljubljana, 2021

To my parents.

Acknowledgements

First and foremost, I would like to deeply thanks my advisor Miha Nemevšek for his guidance, patience and encouragement throughout my entire stay at the institute. I really enjoyed working with him. I learned a lot from the plenty of discussions and collective reasoning about the understanding of nature. I would like to thank him for his constant disposition to talk and his always kind and friendly treatment. I feel fortunate to study under his supervision and pleasant environment.

I cannot forget to mention all my colleagues at F1, in particular those participating in the daily coffee breaks for the interesting talks. I consider them as a very kind and sociable group, which makes me feel welcome from my first days of work at the institute. I would like to thanks Borut Bajc, Svjetlana Fajfer, Jernej Kamenik, Nejc Košnik and Saša Prelovšek for their great attitude and attention. I admire each of them in both their academic and personal aspects. It was my great pleasure to undertake part of my research in collaboration with Alessio Maiezza, Matevž Pintar, Lorenzo Ubaldi, Rok Medveš and Aleksandar Ivanov. I thanks them for the valuable discussions and persistence in the projects. I would like to extend my thanks to Darius Faroughy and Luis Valle Silva for answering my questions, sharing their experiences and for the interesting discussions.

My gratitude goes also to the many other friends which occupy the fondest memories I keep from my happy stay in Ljubljana. I also would like to thank my good friend and colleague Manuel Vielma for his constant support and wise advice.

This work would not have been possible without the enormous sustenance I got from my previous institute ICTP. My sincere gratitude to those that have made possible that support. I would also like to thank my former professors at Los Andes University, Venezuela, especially to Alejandra Melfo and Nelso Pantoja. They patiently guided and inspiring me to become a particle physicist.

Last but not least, I am deeply indebted to my sister Carely and my parents Elydes and Carlos for their love and unconditional support. They are largely responsible for the part of me of which I could feel proud. They were indispensable for this to happen.

Razpad lažnega vakuuma z več skalarnimi polji

Izvleček

Kot pri vrenju pregretih tekočin, je razpad lažnega vakuuma fazni prehod prvega reda. Lokalno osnovno stanje preide v energetsko bolj ugoden nižji minimum energije, ki se zgodi zaradi termičnih in kvantnih fluktuacij polj.

V tem delu predstavimo učinkovito semi-analitično metodo, ki izračuna razpadni čas takšnega stanja za poljubno število skalarnih polj in prostorsko-časovnih dimenzij. Osnovana je na naboru poljubnega števila linearnih segmentov, ki opišejo potencial z več minimi. Eksaktne rešitve razvoja polja za vse segmente so združene v popoln opis konfiguracije odbojnega polja, ki dá vodilni prispevek k razpadni širini. S povečevanjem števila segmentov, dobimo odbojno akcijo do željene natančnosti. Ujemane enačbe, ki se pri tem pojavijo, se reši analitično, posplošitev na več polj pa je izračunana iterativno s pomočjo linearnih analitičnih perturbacij.

Na osnovi te konstrukcije smo ustvarili robusten in uporabniku prijazen `Mathematica` paket, imenovan `FindBounce`, ki implementira našo metodo. Zaradi semi-analitične strukture, računska zahtevnost raste linearno s številom polj in segmentov. Predstavimo nekaj aplikacij in primerjav z drugimi orodji, pri katerih je izvajalni čas v grobem manj kot 1 (2) sekundi za 10 (20) polj z 0.5% natančnostjo akcije.

Za konec opišemo postopek, ki izvrednoti prispevke višjega reda k razpadni širini za poljuben gladek potencial, in ga posplošimo tako, da zaobjame tudi potenciale z nezveznimi prvimi odvodi. Posledično dobimo točno razpadno širino na nivoju ene zanke za realno in kompleksno skalarno polje v dvojnem kvartičnem potencialu z dvema minima na drevesnem redu. Izračunamo produkt lastnih vrednosti, odstranimo translacijske ničelne načine in renormaliziramo divergence s formalizmom zeta funkcije. Ostane nam zaključena oblika celotne razpadne širine.

Ključne besede:

Kvantno tuneliranje, instantoni, razpad lažnega vakuuma, stabilnost vakuuma, fazni prehodi, kozmologija, bariogeneza, gravitacijski valovi.

False vacuum decay with multiple scalar fields

Abstract

As in boiling super-heated liquids, the decay of a false vacuum is a first-order phase transition. A local ground state decays to an energetically more favorable minimum of lower energy due to the thermal and quantum fluctuations of the fields.

In this work, we present an efficient semi-analytic method that computes the decay rate of such a state for any number of scalar fields and space-time dimensions. It is based on the collection of an arbitrary number of linear segments that describe a potential with several minima. The exact evolution of the field for each segment to provide the complete description of the bounce field configuration, which provides the leading contribution of the decay rate. By increasing the number of segments, one obtains the bounce action up to the desired precision. The resulting matching equations are solved semi-analytically and the generalization to more fields is computed iteratively via linear analytic perturbations.

Based on this construction, we provide a robust and user-friendly `Mathematica` package that implements our method, named `FindBounce`. As it preserves the semi-analytic structure of the method, its computational time grows linearly with the number of fields and segments. We present several applications and comparisons with other tools, where typical running time is roughly less than 1 (2) seconds for 10 (20) fields with 0.5% accuracy of the action.

Finally, we describe a procedure that computes subleading contributions of the decay rate for any smooth potentials and extend it to include potentials with discontinuous first derivatives. As a consequence, we exhibit an exact decay rate at one loop for a real and complex scalar field in a bi-quartic potential with two tree-level minima. We compute the product of eigenvalues, remove the translational zero modes and renormalize the divergences with the zeta function formalism. We end up with a complete decay rate in a closed-form.

Keywords:

Quantum tunneling, Instantons, False vacuum decay, Vacuum stability, Phase transitions, Cosmology, Baryogenesis, Gravitational waves.

Contents

List of figures **15**

List of tables **21**

List of abbreviations and symbols **23**

1 Introduction **25**

2 False vacuum decay: the bounce **31**
2.1 Tunneling in quantum mechanics 31
2.2 Single field bounce 33
2.3 The thin wall approximation 36
2.4 Re-scaling properties and Derrick's Theorem 38
2.5 Exact solutions of the bounce 38
2.5.1 The triangular potential 39
2.5.2 The bi-quartic potential 40
2.6 Evolution of the bubble in Minkowski space 41

3 Polygonal bounce: from single to multifield decay rate **45**
3.1 Introduction 45
3.2 Single field polygonal bounces 45
3.3 Evaluating polygonal bounces 48
3.3.1 Implementation 48
3.3.2 Examples, convergence and comparisons 50
3.4 Extending polygonal bounces 52
3.5 Multi-field polygonal bounces 55
3.5.1 Constructing multi-field polygonal bounces 57
3.5.2 Examples and path convergence 60
3.6 Conclusions and outlook 61

4 `FindBounce`: A package for multifield bounce action **63**
4.1 Introduction 63
4.2 Installation and running guide 64
4.2.1 Download and installation 64
4.2.2 Running 64
4.2.3 Contributing 65
4.3 Using the `FindBounce` and its output 65
4.3.1 `FindBounce` options 65
4.3.2 Bounce function output and manipulation 68
4.4 Examples 69

4.4.1 Single field benchmark . . . 69
4.4.2 Bi-quartic potential . . . 72
4.4.3 Intermediate minima and disappearing instantons . . . 73
4.4.4 Potentials unbounded from below . . . 74
4.4.5 Two field benchmark . . . 75
4.4.6 Thermal corrections and nucleation temperature . . . 77
4.4.7 Beyond two fields . . . 79
4.5 Conclusions and outlook . . . 82

5 The decay rate at one loop: An exact solution . . . 83
5.1 Introduction . . . 83
5.2 Loop corrections . . . 84
5.2.1 The prefactor . . . 84
5.2.2 Evaluation of the prefactor . . . 86
5.3 Functional determinants . . . 87
5.3.1 Radial mode separation and exact product of eigenvalues . . . 87
5.3.2 Removing the zero modes . . . 89
5.3.3 Finite sum . . . 90
5.4 Zeta function regularization . . . 91
5.4.1 Zeta function via contour integral . . . 92
5.4.2 Renormalization of the functional determinant . . . 94
5.5 Summary of decay rates . . . 97
5.5.1 Real quartic . . . 97
5.5.2 Complexified quartic . . . 99
5.6 Conclusions and outlook . . . 100

6 Concluding remarks . . . 103

Bibliography . . . 105

Appendix A Appendix to Chapter 2 . . . 119
A.1 On $D = 2, 6, 8$ dimensions . . . 119
A.2 Multi-field $N = 3$ in D dimensions . . . 120
A.3 Real radii and root finding . . . 120

Appendix B Appendix to Chapter 3 . . . 123
B.1 One-Loop effective potential . . . 123
B.2 Multi field potential parameters . . . 123

Appendix C Appendix to Chapter 4 . . . 127
C.1 A example of the Gel'fand Yaglom theorem in a $D = 1$ potential well 127
C.2 The prefactor for polygonal bounce . . . 128
C.3 Bessel, Saddle-point and Zeta function approximations . . . 129
C.4 Derivation of the high-l expansion of f_l . . . 130

Razširjeni povzetek . . . 133
7.1 Uvod . . . 133
7.2 Poligonski odboj . . . 135
7.3 FindBounce: Paket za večpoljsko odbojno akcijo . . . 138

7.4 Kvantne fluktuacije 141
7.5 Sklepne opombe 144

List of publications related to this doctoral thesis 145

List of figures

1.1 Left: A single field potential with two non-degenerate minima. Center: A multi-field interpretation of the potential on the left. The red path underlines the bounce trajectory in field space, while the black path stands for the trajectory of the bounce if there were no interactions among the fields. Right: Spontaneous creation of bubbles transforming the false state into the true one. 25

2.1 An example of a particle that tunnels from q_+ to the materialization point σ at the time $\tau = 0$. Left: Potential with two non-degenerate minima. Center: The potential on the left inverted after the analytic continuation to Euclidean space. Right: The evolution of the particle subjected to the potential on the left. 32

2.2 Left: An example of a potential with two minima with unstable false vacuum state at φ_+ and a stable true one at φ_-. Right: The potential on the left after an analytic continuation into Euclidean space. The field starts in a non-trivial value of the field φ_0, such that it ends up at the false vacuum at infinity. 33

2.3 Left: An example of a potential with a small energy difference $\Delta V = \epsilon$. Center: Bounce field configuration for the potential on the left. The wall of the bubble is highlighted in pink. Right: The bounce field in a region of space: inside (outside) the bubble the value of the field is φ_- (φ_+), while on the thin wall it is φ_w. 36

2.4 Left: The piece-wise linear potential with two segments in blue, superimposed on the potential in gray. Right: The bi-quartic potential. 39

2.5 Left: The triangular potential with an extra segment with slope a_{-1} at the true vacuum to include the downward movement of the classical field. Right: The classical field configuration after the materialization of the bubble corresponding to the potential on the left. 42

2.6 Left: The expansion of the bubble in Minkowski space-time for particular values of the classical solution φ. Right: The expansion of the bubble for any space, time and field values. 43

3.1 Left: Linearly off-set quartic potential in gray and the polygonal approximation with $N = 7$ in blue. Right: The bounce field configuration corresponding to the potential on the left, computed with the polygonal bounce approximation. 46

3.2 Schematic overview of finding the PB. The segment with the solution (in this example $s = 2$ and $R_{in} = R_2$) can be found by evaluating the PB on the boundaries of $R_2^{\min} = 0$ and $R_2^{\max}$ and checking that the imaginary part of the final radius R_{N-1} becomes non-zero. Finally, the solution of R_2 is found such that the scaling parameter $\lambda \to 1$. . . 49

3.3 The initial radius $R_0^{(N)}$ of case b) and $D = 4$ for the uniform segmentation with N points, normalized to the minimal $N = 3$ setup. Similar behavior appears for $D = 3$. Different lines correspond to the range of ϵ, which controls the separation between the minima in (3.18), see text for details. 51

3.4 The bounce action $\mathcal{S}_0^{(N)}$ normalized to the maximal $N = 400$ uniform segmentation with $D = 4$. The solid lines show the PB method for different ϵ that defines the input potential. The inset shows the same, for a smaller number of segments. The dotted lines show the comparison to other methods and tools, see text for details. 52

3.5 Left: The linearly off-set quartic potential in gray, the linear polygonal approximation with $N = 7$ in dashed blue and the 2^{nd} order quadratic correction in solid blue. Right: The field solution in the PB approximation in dashed and the 2^{nd} order improved solution in solid orange. 53

3.6 The bounce action of the improved bounce calculation including the second order correction. The lower colored lines correspond to the corrected action, while the upper gray ones show the leading PB for comparison. 55

3.7 An example of a multifield potential with two fields, trajectory of the bounce in blue and its projection on the bottom. Red dashed line is the path in the absence of the potential or interactions among fields, while the solid red one is the path that minimizes the potential. . . . 56

3.8 The PB solution for two fields in $D = 4$ with $N = 7$ segment points. Left: Path in field space with the initial straight line ansatz $\bar{\varphi}$ with empty circles and the first iteration of the PB solution in solid blue and full circles; the result from shooting is shown in purple. Right: Iterations of the evolution in Euclidean time for $\varphi_1(\rho)$. 58

3.9 Multi-field polygonal solution in $D = 4$ with $N = 15$ segmentation points. The starting ansatz is the straight dashed line connecting the two minima, shown as black dots, together with the saddle point. The solid lines are subsequent iterations that converge to the final path that solves the bounce equations. Insets show the action compared to other approaches. Left: The case a) set-up with the initial endpoint, which is free to move. Right: The case b) potential of the thin wall type with fixed endpoints in the minima. 60

4.1 Left: The benchmark potential from Eq. (4.1) for different values of α going from thick $\alpha = 0.6$ to thin wall $\alpha = 0.99$. Right: The bounce action $\mathcal{S}_s$ for each potential configuration and a given number of field points s, normalized to $s = 400$ and computed in $D = 4$. 70

4.2 Left: Evaluation time with respect to the number of field points, averaged over two intervals of α corresponding to thin and thick wall regimes. Right: The bounce field configuration and action with $N = 31$ (default) field points for different tolerance value of the action controlled by `"ActionTolerance"`. Reference values of the action for `"FieldPoints"->` 10 and 100 field points with `"ActionTolerance"->` 10^{-6} (default) are shown on the green background. 71

4.3 Left: The piecewise quartic potential for different values of the potential difference between the vacua, going from the thin wall $\Delta V = -0.1$ to thick wall $\Delta V = -20$ regime. Right: The bounce action $\mathcal{S}_s$ for different number of field points, normalized to the exact result $\mathcal{S}_0$ of the bi-quartic potential. 72

4.4 Left: The minimal example of a potential with an intermediate minimum. The inset shows the bounce solution with the typical double bubble wall shape in orange. Right: Decay rates for the direct (ABC) and the two subsequent (AB, BC) transitions, together with the total decay rate (4.2). 73

4.5 Left: Potential unbounded from below. The pure quartic, polygonal-quartic and input potentials are shown in red, solid blue and black, respectively. The dashed blue line is the pure quartic potential that is joined to the piece-wise polygonal potential. Right: The bounce field configuration with its bounce action. The solid lines show the field configuration with PB+quartic estimate, the dashed are the pure polygonal solutions and the dotted black line is the numerical result obtained with over-under-shooting. 75

4.6 Left: Potential contours in solid gray lines, the final trajectory of the bounce field in solid blue line and three different initial paths in dashed. Black dot-dashed line is the default straight line ansatz, the straight dashed blue line includes the intermediate point at {6,6}, while the red dashed line is a parabola, set by hand. Right: The field configuration $(h(\rho), s(\rho))$ of the final iteration and the associated bounce action in the caption. 77

4.7 Left: The multi-field bounce action $\mathcal{S}_s$ average, normalized to the one with $N = 400$ field points. Right: Multi-field time measure with respect to number of fields for several field points. The solid lines were obtained by `FindBounce` with `"ActionTolerance"` $\to 10^{-4}$. The dashed lines with dots are the time measurements from other existing tools, see text for details. 81

5.1 Deformation of the integration contour of eq. (5.36) from the positive real axis to the negative one. The red dots represent the location of the poles such that $\psi(\infty, \gamma) = 0$. 93

5.2 The FV decay rate for the bi-quartic potential in (2.39). The black solid line shows the total rate, while the dashed ones show the semi-classical part $\mathcal{S}_0$ in red and the finite renormalized prefactor $\mathcal{S}_1$ in dark yellow. The dotted lines correspond to the TW leading expansion, where we set $y = \lambda_1/\lambda_2 = 1$ and expand up to $(x-1)^{-3}$ in dark green, additional corrections up to $(x-1)^0$ in light green and the flat potential limit $x = v_1/v_2 \gg 1$ in blue. The shaded regions show the variation of $\lambda_2 \in \{0.1, 1\}$ in purple and $\lambda_1/\lambda_2 \in \{0.5, 1\}$ in light brown. 98

A.1 Left: The final radius dependence on R_0 for $N = 50$ and $\varepsilon = 0.03$, showing the real and imaginary part, as well as the corresponding value obtained from R_{N-1} in the matching condition in (3.15). Right: The continuous version of Derrick's theorem (2.27) with $\mathcal{T}$ computed with the PB and $\mathcal{V}$ from the input potential in (3.18). The normalized quantity acts as a test of convergence and goodness of approximation. 121

A.2 Left: The initial field value φ_0 normalized to the position of the false minimum in $\tilde{\varphi}_1$. Right: The final radius R_{N-1}, normalized to the $N = 3$ approximation. 122

C.1 The ratio of determinants $\mathcal{R}_l$ for a given multipole. Left: The ρ dependence for shooting in solid and the PB solution with $N = 3$ ($N = 50$) in dotted (dashed) lines. Right: The ratio at $\rho \to \infty$ with solid (empty) squares denoting the $N = 3$ ($N = 50$) PB approximation, while the solid line connects the results from the shooting procedure. 128

7.1 Levo: Primer potenciala z dvema minima z nestabilnim lažnim vakuumskim stanjem pri φ_+ in stabilnim pravim pri φ_-. Desno: Potencial z leve po analitičnem nadaljevanju v evklidski prostor. Polje začne v netrivialni vrednosti φ_0, tako da v neskončnosti doseže pravi vakuum. 135

7.2 Levo: Linearno zamaknjen kvartični potencial v sivem, linearna poligonska aproksimacija $N = 7$ v črtkano modrem in kvadratični popravki drugega reda v polnem modrem. Desno: Rešitev polja v aproksimaciji PO v črtkanem oranžnem in izboljšana rešitev drugega reda v polnem oranžnem. 135

7.3 Odbojna akcija izboljšanega izračuna odboja, ki vključuje popravke drugega reda. 137

7.4 Levo: Primer potenciala z dvema poljema, trajektorija odboja v modrem in njena projekcija na dnu. Rdeča črtkana črta je pot, izračunana brez interakcij med polji, polna rdeča črta pa je pot, ki minimizira potencial. Polna modra črta predstavlja večpoljsko poligonsko rešitev v $D = 4$ z $N = 15$ segmentacijskimi točkami. Desno: Nivojnice potenciala na levi. Ravna črtkana črta je izhodiščni nastavek, ki povezuje dva minima s sedlom. Oba minima in sedlo so označeni s črnimi pikami, polne črte so kasnejše iteracije, ki konvergirajo h končni poti, ki reši odbojne enačbe. Vstavljena tabela prikazuje akcijo v primerjavi z drugimi pristopi. 138

7.5 Levo: Povprečje večpoljske odbojne akcije $\mathcal{S}_s$, normalizirano na povprečje z $N = 400$ točkami polja. Desno: Meritve časa v večpoljskem primeru v odvisnosti od števila polj za več točk polja. Polne črte smo dobili s `FindBounce` z `"ActionTolerance"` $\to 10^{-4}$. Črtkane črte s pikami so meritve časa za druga obstoječa orodja, glej besedilo za podrobnosti. 140

List of tables

4.1 Comparison of the bounce action obtained by different methods in the literature for various number of fields n_φ. It includes `FindBounce` with 10, 30 and 100 field points and `CosmoTransition`, `AnyBubble`, `BubbleProfile` and `SimpleBounce`. 81

B.1 Multi-field potential parameters c_i that define the potential in (4.9). . 124
B.2 The bounce action of the single and multi-field potential in Eq. (B.6) and (4.9), respectively computed using `FindBounce` with 10, 30 and 100 number of field points. 125

C.1 The total prefactor contribution at one-loop, computed using the numerical shooting procedure and compared with the polygonal method with $N = 3, 10, 50$ and 100 segmentation points. The rate is normalized to $(1-\alpha)^3$ and agrees with the analytical thin wall limit result that gives $9/32(1 - 2\pi/(9\sqrt{3})) \sim 0.17$. 129

List of abbreviations and symbols

Abbreviations

BBO Big Bang Observer

DECIGO Deci-hertz Interferometer Gravitational Wave Observatory

FV False vacuum

LISA Laser Interferometer Space Antenna

PB Polygonal bounce

QFT Quantum Field Theory

SM Standard Model

TV True vacuum

TW Thin wall

WKB Wentzel, Kramers and Brillouin

Symbols

Γ Decay rate

$\mathcal{S}_0$ Euclidean bounce action

V Potential

A Prefactor

D Space-time dimension

Chapter 1

Introduction

It is well known among particle physicists that quantum field theory (QFT) is a powerful tool that has led to one of the most fantastic agreements between the theoretical predictions and the experiment in the history of science. In this framework, particles are treated as excited states of some more fundamental objects called quantum fields. As in quantum mechanics, the state with the lowest possible energy is the ground state or vacuum energy, which in QFT is identified as the minimum of the potential.

In general, a model might have several non-degenerate minima as on the left panel of fig. 1.1, where the lowest one is a stable state, known as the true vacuum (TV) while the local ones are metastable. The latter ones are false vacuum (FV) states as they will eventually decay into a more favorable lower state of energy by a process of barrier penetration analogous to alpha decay in quantum mechanics. It is caused by quantum and thermodynamic fluctuations of the fields, where the state tunnels through or passes over the potential barrier respectively.

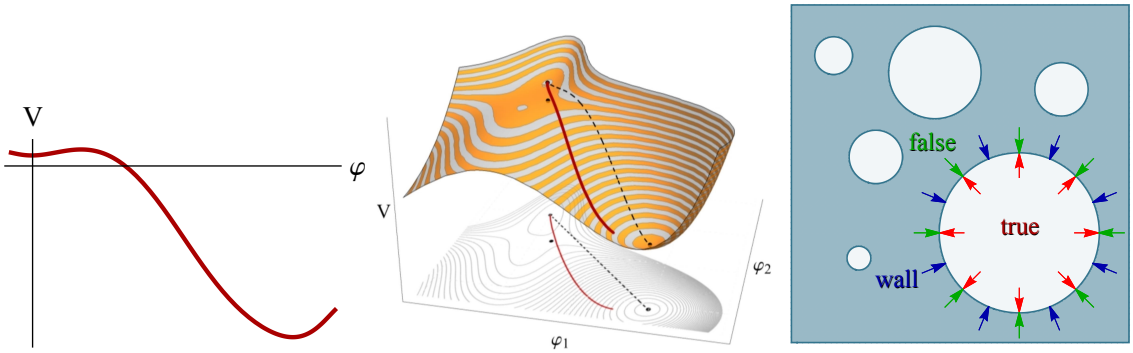

Figure 1.1: Left: A single field potential with two non-degenerate minima. Center: A multi-field interpretation of the potential on the left. The red path underlines the bounce trajectory in field space, while the black path stands for the trajectory of the bounce if there were no interactions among the fields. Right: Spontaneous creation of bubbles transforming the false state into the true one.

This tunneling effect in QFT is a first-order phase transition due to the abrupt changes of state, analogous to the boiling of a super-heated/cooled fluid or nucleation process in statistical physics. We might have seen the qualitative features of this phenomenon in a super-cooled bottle of pure liquid water that we have let chill in the freezer. As the water is in an unstable state, after banging the bottle or a

nucleation event, a piece of ice crystal is formed and will seed the rest of the ice crystal, the true ground state.

Similar pictures describe the decay of a false vacuum where, due to the fluctuation of the fields, small bubbles of true vacuum are eventually created spontaneously somewhere in the universe, as sketched on the right panel of fig. 1.1. This first step in the formation of the new phase is called a nucleation event. Once they are formed, they expand either to almost the speed of light in the vacuum or at a terminal speed at high temperatures, transforming the entire space into the new phase of a true vacuum. In chapter §4, we will show how to compute the nucleation temperature of a particular model as the universe is cooling down and in section §2.6, we will explain more about the subsequent evolution of the bubble.

In principle, we could be living in a metastable ground state as long as it is sufficient long-lived with respect to the age of the universe. This is actually the case if we assume that there is no physics beyond the Standard Model (SM), which is the theory that has best described all the known fundamental particles in the universe. The recent discovery of the Higgs boson in 2012 [1, 2], the only fundamental scalar, has remarkably shown us that its ground state does not reside in the lowest minimum of energy, but in a local one. This fact has been the motivation of a large number of papers and had played an important role in the Higgs mass bounds [3, 4, 5]. Due to its fascinating and fundamental consequences, the instability of the Higgs vacuum has deserved accurate calculations and dedicated studies. Recent works can be found in [6, 7, 8] and references therein, providing a prediction of the lifetime of our universe of $\sim 10^{139^{+102}_{-51}}$ years [9, 10].

It is well known that we must go beyond the SM and the above picture might change dramatically. Although SM has shown huge successes in providing experimental predictions, it leaves some phenomena unexplained and whose explanations will unavoidably affect the predictions of the fate of our vacuum state [11]. To mention a few of the fundamental problems, we have: the baryon asymmetry of the universe [12, 13, 14, 15], the viable dark matter particles required by cosmological observations [16, 17, 18, 19, 20], the accelerating expansion of the universe as possibly described by dark energy [21, 22], and the incorporation of gravity [23]. Besides, it also cannot generate neutrino masses, which is in direct contradiction with experimental results on neutrino oscillations [24, 25]. Vacuum stability is thus indispensable and a significant constraint to consider in the development of any theory beyond SM.

This process can not be observed in laboratories, but it can produce exotic cosmological consequences that may be detected in future experiments. In the early universe, particles form a hot plasma, whose thermal effects can drive the phase transition [26, 27, 28, 29]. Here, spontaneous bubbles of TV start emerging in different regions of the universe, as sketched on the right panel of fig. 1.1. As they expand, they eventually collide releasing an enormous amount of energy and thus, provides a possible source of gravitational waves [30, 31, 32, 33, 34, 35, 36, 37] and primordial magnetic fields [38, 39, 40, 41, 42]. Moreover, they can dynamically generate the observed dominance of matter over anti-matter, e.g. in electroweak baryogenesis [43, 44, 45, 46, 47, 48, 49], (see the review in [50]). The features of such processes is a function of the bubble wall velocity relative to the plasma and other quantities that can be determined from the model at the nucleation temperature, which has been the subject of intense study [51, 52, 53, 54, 55, 56, 57, 58, 59].

Gravitational waves were directly detected for the first time in 2015 [60] and have brought a new era for astronomy and the intriguing possibility to probe high energy physics. Current aLIGO [61] and aVIRGO [62] observatories are operating at frequencies that are mostly insensitive to TeV scale first order phase transitions. However, space-based gravitational wave detectors such as LISA [63], DECIGO [64] and BBO [65, 66] are scheduled to launch in over a decade from now and look for evidence of cosmological phase transitions, for a recent review on LISA capabilities see [63].

The features of such decay processes have long been understood and studied by the seminal works [67, 68, 69] for single scalar[1] field theories at zero temperature. From a similar approach, the probability of the phase transition of the vacuum due to thermodynamic fluctuations of the field at high temperatures was developed by [26, 27, 28]. They found that the probability of decay of a false vacuum per unit volume is of the form

$$\frac{\Gamma}{\mathscr{V}} = A\, e^{-\mathcal{S}_0/\hbar}\,(1 + \mathcal{O}(\hbar))\,, \tag{1.1}$$

where $\mathcal{S}_0$ is the Euclidean action and A is a dimensionful pre-factor. A more formal and extended derivation has been provided recently [72], aside from alternative approaches [73, 74, 75, 76, 77, 78]. The expression above is general, as it is valid for any number of fields and space-time dimensions.

The aim is to obtain the so-called bounce solution, which is the dominant semi-classical field configuration that extremize the Euclidean action in the exponential factor. It provides the leading contribution of the decay rate and it is thus the fundamental topic of my entire work. Finding the bounce field configuration in a closed form is in general impossible for an arbitrary potential and in most occasions, the calculation of the bounce is thus performed numerically. For particular potentials, analytic solutions can be found. We dedicate an entire section §2.5 to describe them since it turns out that they constitute the pillars of this work.

The problem of vacuum decay complicates significantly when an arbitrary number of fields is considered, as on the center panel of fig. 1.1. As mentioned above, most new physics beyond SM contain models with additional scalar fields and such theories usually possess a nontrivial vacuum structure with several metastable and potentially long-lived ground states. Finding the path in field space and computing the bounce with non-analytic potentials are still challenging. When there are interactions among the fields, the trajectory in field space of the bounce is in general non-trivial, as shown by the red line in the fig. 1.1. Existing approaches to this problem [79, 80, 81, 82, 83, 84, 85, 86, 87, 88, 89, 90, 91] address these challenges in various ways. However, they have in common that they become either too imprecise or impractical for potentials with a large number of fields, in particular when the energy difference between minima is small. Besides, they provide purely numerical outputs of the bounce field configuration, which makes it difficult to understand the subsequent evolution of the bubble.

In this work, we overcome a number of shortcomings regarding the bounce field, which are listed in detail in section §2.2 and provide an efficient approach to obtain

[1] As we want to preserve Lorentz invariance, the vacuum expectation value can only be provided by a scalar field. Although it is also possible to form Lorentz invariant objects with fermionic and gluon condensates, for instance [70, 71].

the decay rate of any multi-scalar field potentials. The main contribution is that we reformulate the problem from the single field bounce and avoid the use of the usual shooting method. We do it by collecting a set of analytic solutions that together describe any potential. We move on semi-analytically to multi-fields by iterative perturbation around the single field bounce. As a result, we present a `Mathematica` package called `FindBounce` that stands out in speed and efficiency and provide the first semi-analytic bounce for a general potential, which allows for further simplifications. This package is not only competitive and robust but it is also user-friendly, with the native `Mathematica` look and feel, together with well documented examples.

To complete the calculation of the decay rate, we must obtain the pre-exponential factor A in eq. (1.1), which is associated with one-loop field theory calculations. The evaluation of A and the renormalization of its ultraviolet divergence are well understood [69, 92, 93], but they are notoriously more difficult to compute than the bounce, since A is proportional to functional determinants that describe quantum fluctuations around a non-trivial background.

As the pre-factor is exponentially suppressed by $e^{-\mathcal{S}_0}$, it does not have a dramatic dependence on the parameters of the theory, so it can be estimated by dimensional arguments on many occasions. However, a precise and consistent calculations of the pre-factor are needed in several contexts of physics. This is the case of the lifetime of the Higgs vacuum in the SM [9, 10], where the most likely energy scale of decay $\sim 10^{17}$ GeV is way above the electroweak scale and loop corrections are indispensable. Moreover, in the early universe the phase transition occurs due to thermal fluctuations, which appear first at one loop. If A is not estimated properly, the nucleation temperature may be erred by orders of magnitudes, as it has been shown recently [94]. In general, the total decay rate Γ is a physical quantity, so it must be independent of the renormalization scale μ that comes from the running of the parameters of $\mathcal{S}_0$ at one-loop [95, 96], that is $\mu\, \mathrm{d}\Gamma/\mathrm{d}\mu = 0$. Thus, for a consistent one-loop calculation of Γ, the pre-factor must be computed as it will provide explicit μ terms that compensate the one-loop μ dependence from $\mathcal{S}_0$. In short, precise and consistent evaluation of the vacuum instabilities demand a deeper understanding of the pre-factor calculation, in particular for future measurements of the physics beyond the SM.

A precise calculation of the prefactor can be obtained numerically for any renormalizable and smooth potential [69, 97, 98, 99, 100, 101]. Although closed-form results of the prefactor exist, but only for very few special cases such as: in the thin wall limit [102, 103] (see also [104]) and the unstable quartic potential [9, 105]. To my knowledge, the first complete closed-form solution of the sub-leading one-loop quantum fluctuations for a potential with two separate tree-level minima appear to be missing. In this work, we fill this gap by obtaining the decay rate in a closed-form at one loop for a particular model in chapter §5. In this way, we set a new benchmark and the basics for future works related to the prefactor. It belongs to an intermediate step in our aim of obtaining a general procedure that computes A for general multi scalar field potentials.

This work is organized as follows. In the upcoming chapter §2, I provide an overview of the false vacuum decay regarding the semi-classical approximation and its bounce field configuration. I contribute with my interpretation of these well-known results, where I introduce the notation and convention used throughout the

entire work. I end up with an analytic description of the evolution of the bubble after it is materialized. In chapter §3 I present a new semi-classical method to compute the bounce field configuration for any potential up to an arbitrary desired precision, called Polygonal Bounce (PB). Then in section §3.5 we move on to multifields and compute the bounce via analytic perturbation of the single field bounce solution. In chapter §4 we provide a `Mathematica` package that implements PB with examples that include benchmarks, performance, timing, and comparisons to other existing tools. We will assume that the prefactor A in (1.1) can be well estimated on dimensional grounds until we compute it rigorously in chapter §5. There, I present a general procedure to compute those quantum fluctuations and a closed-form solution of the decay rate at one loop for a potential with two tree-level minima. We leave the concluding remarks and outlook for §6 and the technical details for the appendix.

Chapter 2

False vacuum decay: the bounce

The phase transition of a local ground state via barrier penetration in QFT has long been studied since the seminal works by [28, 30, 67, 68, 69]. They found that the decay probability per unit volume of space and time is given by

$$\frac{\Gamma}{\mathscr{V}} \approx A\, e^{-\mathcal{S}_0}\,, \tag{2.1}$$

in the limit when $\hbar$ is small. Here, $\mathcal{S}_0$ is the action in Euclidean space evaluated from the bounce field $\bar{\varphi}$ and A is a dimensionfull quantity. The bounce field is a non-trivial scalar field configuration that extremizes the Euclidean action and describes the phase transition among vacua states. The $\mathcal{S}_0$ term, commonly called the bounce action, usually dominates the decay rate due to its exponential dependence and constitutes the main subject of my work. The coefficient A is related to one-loop calculation and represents sub-leading contributions to the decay rate. Before we compute it rigorously in chapter §5, we would assume it is approximately given by $A \approx v^4$, where v is some characteristic mass scale of the theory under study.

In this chapter, we present a brief introduction of the bounce field configuration and the evaluation of the bounce action. We start with a heuristic derivation of the false vacuum decay from a well-known process of barrier penetration in quantum mechanics in section §2.1. Then we discuss the exponential factor $\mathcal{S}_0$ in section §2.2 and a closed-form solution in the well-known thin wall approximation in section §2.3. Throughout the entire work, we will make use of the rescaled properties of the bounce action and some of its closed-form solutions, so we describe them in detail in sections §2.4 and §2.5 respectively. In section §2.6, we complete our description by presenting the evolution of the bubble in real time after it is materialized, by the exclusive use of exact solutions. The introduction of these well-known results is presented in my notation and interpretation of the subject.

2.1 Tunneling in quantum mechanics

As it is instructive to start with a brief quantum mechanics description [68], let us consider the tunnel effect of a particle of unit mass and energy $E = V(q_+)$ through a potential $V(q)$ with two minima, sketched in the left panel of fig. 2.1. Its materialization point is denoted by σ, such that $V(\sigma) = V(q_+)$, which corresponds to the classical turning point. It is well known that the wave functions of the Schrödinger equation can be well approximated by the WKB method [106, 107]

when $\hbar$ is small. In this semi-classical approximation, the wave function ψ falls off exponentially between q_+ and σ by an amount $T \equiv \psi(\sigma)/\psi(q_+)$, such that the decay rate is given by

$$\Gamma \sim |T|^2 \implies \Gamma \approx \Omega\, e^{-2\int_{q_+}^{\sigma} \mathrm{d}q\sqrt{2(V-V(q_+))}}\,, \tag{2.2}$$

where Ω is related to the classical frequency of oscillations of the particle around the local minimum, while the exponefigactor describes how much of the wave-function gets through the barrier.

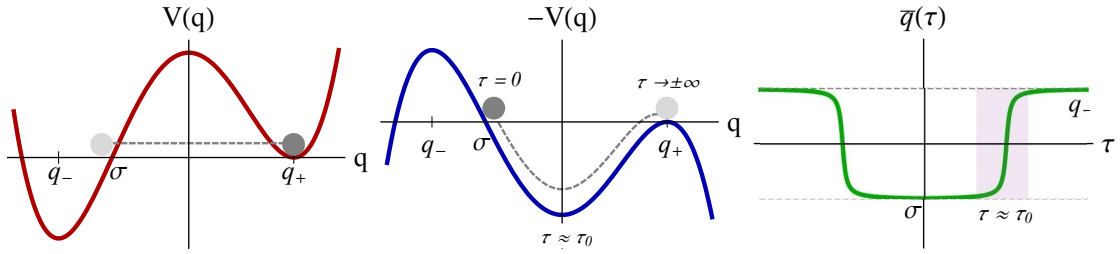

Figure 2.1: An example of a particle that tunnels from q_+ to the materialization point σ at the time $\tau = 0$. Left: Potential with two non-degenerate minima. Center: The potential on the left inverted after the analytic continuation to Euclidean space. Right: The evolution of the particle subjected to the potential on the left.

In order to get closer to field theory, let us recast the WKB factor more conveniently in terms of the minimal classical Euclidean action as,

$$\int_{q_+}^{\sigma} \mathrm{d}q\sqrt{2\left(V - V\left(q_+\right)\right)} = \min_{q(\tau)} \int \mathrm{d}\tau \left(\frac{1}{2}\left(\frac{\mathrm{d}q}{\mathrm{d}\tau}\right)^2 + V - V\left(q_+\right)\right). \tag{2.3}$$

To see this, let us compute the function $\bar{q}(\tau)$ that extremizes the action, which can be obtained from the Euler-Lagrange equation,

$$\frac{\delta \mathcal{S}}{\delta q} = 0 \implies \frac{\mathrm{d}^2 q}{\mathrm{d}\tau^2} = \frac{\mathrm{d}V}{\mathrm{d}q}\,. \tag{2.4}$$

This equation corresponds to the classical equation of motion of a particle moving under the influence of a valley $-V$. After a change of variable $U = \mathrm{d}q/\mathrm{d}\tau$ and the use of the chain rule we get

$$\dot{U} = \frac{\mathrm{d}U}{\mathrm{d}q}U = \frac{\partial V}{\partial q}\,, \tag{2.5}$$

which can be integrated

$$\frac{1}{2}\left(\frac{\mathrm{d}q}{\mathrm{d}\tau}\right)^2 = V - V(q_+). \tag{2.6}$$

Note that the constant of integration $V(q_+)$ has been chosen conveniently to achieve (2.3). This implies that the classical equilibrium point q_+ can only be reached asymptotically, as $\tau_{q_+} = \pm\infty$; while by time translation invariance, the materialization of the particle σ can be chosen to be $\tau_\sigma = 0$.

From (2.5) and $V(\sigma) = V(q_+)$ we can extract the following boundary conditions

$$\left.\frac{\mathrm{d}q}{\mathrm{d}\tau}\right|_{\tau=0,\pm\infty} = 0\,. \tag{2.7}$$

Thereby equations (2.5) and (2.7) describe the motion of a particle that starts rolling from rest at q_+ at $\tau = -\infty$, then stops in σ at $\tau = 0$ and bounces back to q_+ at $\tau = +\infty$, as shown in the center and right panels of fig. 2.1. This motion is called **the bounce** and is described by the solution $\bar{q}\,(\tau)$.

We conclude that the decay rate is

$$\Gamma \sim e^{-2\int_{q_+}^{\sigma} \mathrm{d}t\sqrt{2(V-V(q_+))}} = e^{-\int_{-\infty}^{\infty}\mathrm{d}\tau\left(\frac{1}{2}\left(\frac{\mathrm{d}\bar{q}}{\mathrm{d}\tau}\right)^2+V(\bar{q})\right)} = e^{-\mathcal{S}_0}\,, \tag{2.8}$$

This is indeed the correct result at leading exponential order, according to a more rigorous derivation [108]. This expression can be generalized to multiple dimensions and derived from the path integral approach in the saddle point approximation or semi-classical limit [109, 110].

2.2 Single field bounce

Let us move on to field theory and consider a scalar field potential V with two non-degenerate minima, where the scalar field expectation value is assumed to be at the local minimum in φ_+, as shown on the left panel of fig. 2.2. Because of the

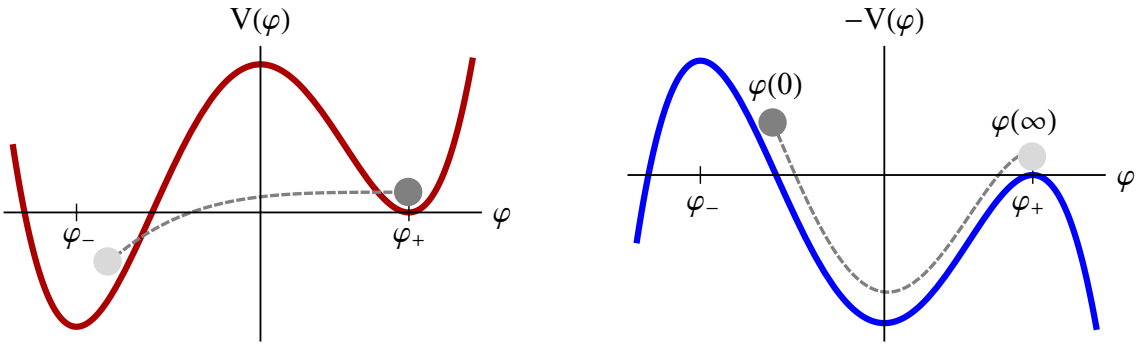

Figure 2.2: Left: An example of a potential with two minima with unstable false vacuum state at φ_+ and a stable true one at φ_-. Right: The potential on the left after an analytic continuation into Euclidean space. The field starts in a non-trivial value of the field φ_0, such that it ends up at the false vacuum at infinity.

quantum and thermal fluctuations, such state of false vacuum (FV) is metastable and eventually decays into the true vacuum (TV), which corresponds to the lowest and stable minimum of the potential at φ_-. That is, to compute the decay rate in (2.1) for any number of space-time dimensions D, we will concentrate on the Euclidean action

$$\mathcal{S}_0 = \int_{-\infty}^{\infty} \mathrm{d}^{D-1}x \int_{-\infty}^{\infty} \mathrm{d}\tau \left(\frac{1}{2}\partial_0\varphi^2 + \frac{1}{2}\nabla\varphi^2 + V(\varphi)\right)\,, \tag{2.9}$$

where it is assumed that the potential is shifted as $V(\varphi_+) = V_{FV} = 0$, so the action is finite. The integral is performed over the fields that satisfy the boundary conditions,

$$\varphi(\pm\infty, \mathbf{x}) = \varphi(\tau, \pm\infty) = \varphi_+ \,, \tag{2.10}$$

As proven by [111, 112], the solution $\bar{\varphi}$ is invariant under $O(D)$ rotations for any dimensions $D > 2$. This implies that one can recast and simplify eq. (2.9) by using spherical coordinates in a D-dimensional Euclidean space. Thus, φ becomes a function of the radial coordinate only,

$$\varphi(t, \mathbf{x}) = \varphi(\rho) \qquad \text{with} \qquad \rho = \sqrt{(\tau - \tau_0)^2 + (\mathbf{x} - \mathbf{x_0})^2} \,, \tag{2.11}$$

and the remaining $D-1$ angles can be integrated out. Hence

$$\mathcal{S}_0 = \frac{2\pi^{\frac{D}{2}}}{\Gamma\left(\frac{D}{2}\right)} \int_0^\infty \rho^{D-1} \mathrm{d}\rho \left(\frac{1}{2}\dot{\varphi}^2 + V \right) = \mathcal{T}_D + \mathcal{V}_D \,, \tag{2.12}$$

where the dot stands for the derivate with respect to ρ and the last two terms represent the integrated kinetic and potential terms, respectively. The field configurations that extremize the action must solve the classical equation

$$\frac{\delta \mathcal{S}_0}{\delta \varphi} = 0 \implies \ddot{\varphi} + \frac{D-1}{\rho}\dot{\varphi} = \frac{\partial V}{\partial \varphi} \,, \tag{2.13}$$

where we must require the solution to satisfy (2.10) and to be an analytic function at $\rho = 0$. Thus the corresponding boundary conditions are

$$\varphi(0) = \varphi_0, \qquad \varphi(\infty) = \varphi_+, \qquad \dot{\varphi}(0) = \dot{\varphi}(\infty) = 0 \,. \tag{2.14}$$

Because of these conditions, the solution of this equation is called the **bounce**. Other solutions are not $O(D)$ invariant, but they contribute with higher values of the action and are exponentially suppressed by $\sim e^{-\mathcal{S}_0}$. Some of the corrections will be included in the prefactor, as we will see in section §5. Nevertheless, we have not just a single bounce solution but a continuum, characterized by the collective coordinates τ_0 and $\mathbf{x_0}$ in eq. (2.11). As we must integrate over these parameters it yields the factor of $\mathscr{V}$ in (2.1).

As in quantum mechanics, equation (2.13) has the analog interpretation of a particle moving along a hyper-surface $-V$, with position $\varphi_i(\rho)$ at time ρ, and subject to a somewhat peculiar viscous damping force, whose coefficient is inversely proportional to ρ.

The initial value of the field φ_0 represents the field value at the center of the bubble, located at $(\tau_0, \mathbf{x_0})$ as defined in (2.11). It admits a trivial solution $\varphi_0 = \varphi_+$, where the value of the field remains constant. This solution is not of interest, unless we are dealing with non-interacting multi-field potentials, as explained in §3.5. The relevant initial condition for the decay process is when φ_0 is somewhere near the TV, below the local minimum of energy, as shown in the right panel of fig. 2.2.

As the particle starts at rest, if φ_0 is released sufficiently far from the TV, the particle will undershoot due to the damping term, i.e. it will not reach the FV at $\rho \to \infty$. Otherwise, if it is released too close to the TV, the damping term

becomes too small and the particle will overshoot the FV at some finite time. By continuity [68], there must be an intermediate non-trivial φ_0 such that satisfies eqs. (2.13).

In principle, this intermediate initial value can be obtained numerically up to any desired precision: by trying various φ_0 until one finds the proper value such that the particle will come to rest at infinity at φ_+. This is called the **shooting** method. However, this method presents several difficulties:

- The coefficient $\sim 1/\rho$ in (2.13) makes the value $\rho = 0$ singular. So when numerically solving the equation, we have to start at some small value $\rho_0 > 0$. But this brings numerical instabilities if we consider $\varphi(\rho_0) = \varphi_0$ and $\dot{\varphi}(\rho_0) = 0$ as boundary conditions. This can be overcome by expanding the potential around φ_0 in (2.13) as $\partial V/\partial\varphi \approx V'(\varphi_0) + (\varphi - \varphi_0) V''(\varphi_0)$ and imposing the conditions (2.14). That is, we get

$$\varphi(\rho_0) = \varphi_0 - \frac{V'}{V''}\left(1 - \Gamma\left(\frac{D}{2}\right)\left(\sqrt{V''}\rho_0\right)^{\frac{1-D}{2}} I_{\frac{D}{2}-1}\left(\sqrt{V''}\rho_0\right)\right)\Big|_{\varphi=\varphi_0}, \quad (2.15)$$

$$\dot{\varphi}(\rho_0) = \frac{V'}{\sqrt{V''}}\Gamma\left(\frac{D}{2}\right)\left(\sqrt{V''}\rho_0\right)^{\frac{1-D}{2}} I_{\frac{D}{2}}\left(\sqrt{V''}\rho_0\right)\Big|_{\varphi=\varphi_0}, \quad (2.16)$$

  where Γ and I are the Euler gamma and modified Bessel functions respectively. The solution computed in this way is less sensitive to the arbitrary choice of ρ_0.

- Another numerical difficulty arises when $\rho \to \infty$. In numerical evaluations, we have to consider infinity as an arbitrary large finite value $\rho_f < \infty$. To get the boundary condition less sensitive to the arbitrary choice of ρ_f, we can shoot backwards from a field value φ_f close to φ_+. As before, expanding the potential around φ_+ in (2.13) as $\partial V/\partial\varphi \approx (\varphi - \varphi_+) V''_{FV}$, the corresponding boundary conditions are given by

$$\varphi(\rho_f) = \varphi_f, \quad \text{and} \quad \dot{\varphi}(\rho_f) = (\varphi_+ - \varphi_f)\frac{\sqrt{V''_{FV}} K_{\frac{d}{2}}\left(\sqrt{V''_{FV}}\rho_f\right)}{K_{\frac{d}{2}-1}\left(\sqrt{V''_{FV}}\rho_f\right)}. \quad (2.17)$$

- The time consumption increases extremely fast with the number of fields since φ_0 must be found in a n_φ-dimensional hyper-surface, with n_φ as the number of fields.

- It requires a large amount of precision when the minima are nearly degenerate. This is the case when the field $\varphi(\rho)$ must remain very close to φ_- until an arbitrary large ρ; so the damping term becomes almost negligible as it depends inversely proportional to ρ and the particle has enough energy to reach φ_+. To appreciate the required accuracy of φ_0, let us consider the evolution of the field around the vicinity of the TV, which given by eq. (2.13) and $V \approx V_{TV} + \frac{1}{2}V''_{TV}(\varphi - \varphi_-)^2$ as

$$\varphi(\rho) - \varphi_- = (\varphi_0 - \varphi_-)\,\Gamma\left(\frac{D}{2}\right)\left(2\sqrt{V''_{TV}}\rho\right)^{\frac{D}{2}-1} I_{\frac{D}{2}-1}\left(\sqrt{V''_{TV}}\rho\right). \quad (2.18)$$

  This implies that φ_0 can be arranged to be as arbitrary close to φ_- for any large value of ρ but it requires an exponential fine-tuning, which in general presents

severe difficulties for numerical methods. Fortunately, for such scenarios, there exists a closed-form approximation, which is presented in the next section §2.3. Nevertheless, as it has a very limited range of validity, a more robust method is needed.

In chapter §3, we address each of these difficulties by providing a new approach that computes the bounce action for any number of fields.

2.3 The thin wall approximation

At some limit, it is possible to compute the Euclidean action in a closed-form. This is the case in which the energy of the FV is slightly below the energy of the TV and the maximum of the potential is positive and not small, as shown in fig. 2.3.

Here, the field must spend a large moment of "time" very close to the TV, such that the damping term becomes so small that the field can reach the FV and stay there. Within the accuracy of our approximation, let us assume that the bounce can be approximated into three regions:

$$\varphi(\rho) = \begin{cases} \varphi_-, & \rho \ll R_w\,, \\ \varphi_w, & \rho \approx R_w\,, \\ \varphi_+, & \rho \gg R_w\,. \end{cases} \tag{2.19}$$

Initially, the field resides exactly at $\varphi_0 = \varphi_-$, then evolves at some large value $\rho \approx R_w$ and finally ends up in φ_+, as sketched in fig. 2.3.

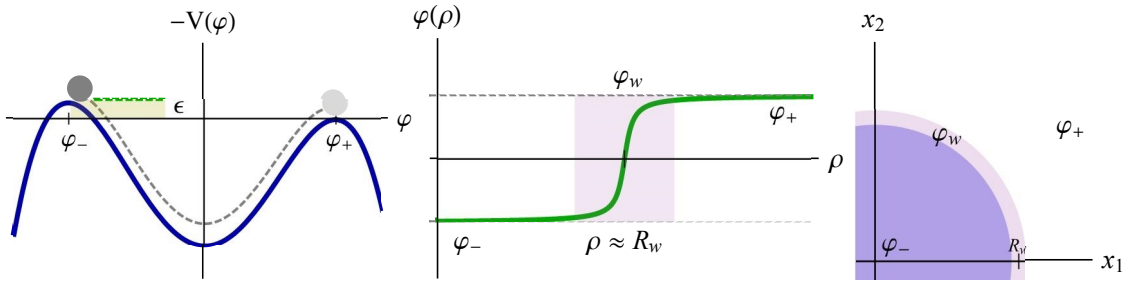

Figure 2.3: Left: An example of a potential with a small energy difference $\Delta V = \epsilon$. Center: Bounce field configuration for the potential on the left. The wall of the bubble is highlighted in pink. Right: The bounce field in a region of space: inside (outside) the bubble the value of the field is φ_- (φ_+), while on the thin wall it is φ_w.

Hence the associated action becomes[1]

$$\begin{aligned} \mathcal{S}_0 &= \frac{2\pi^{\frac{D}{2}}}{\Gamma\left(\frac{D}{2}\right)} \left(\int \mathrm{d}\rho \rho^{D-1} V_{TV} + \int \mathrm{d}\rho \rho^{D-1} \left(\frac{1}{2}\dot{\varphi}_w^2 + V \right) - \int \mathrm{d}\rho \rho^{D-1} V_{FV} \right), \\ &= \frac{2\pi^{\frac{D}{2}}}{\Gamma\left(\frac{D}{2}\right)} \left(-\frac{1}{D} R_w^D \epsilon + R_w^{D-1} \mathcal{S}_0^{D=1} \right), \end{aligned} \tag{2.20}$$

[1]Note the missing factor of two in the last term of eq. (4.15) of the original work [68], realized in $D = 4$.

where $\mathcal{S}_0^{D=1} = \int \mathrm{d}\rho \left(\frac{1}{2}\dot{\varphi}_w^2 + V\right)$ and $\epsilon = V_{TV} - V_{FV}$ is assumed to be positive and small. The first term represents the energy gained from going to a lower state of energy, while the second one is the energy expended in creating the bubble. The latter one can be considered as the energy from the surface tension of the bubble in analogy with bubbles from super-heated fluids.

As the aim is to extremize the action, the radius of the bubble can be obtained by a variation of the action in (2.22) as

$$\frac{\mathrm{d}\mathcal{S}_0}{\mathrm{d}R_w} = 0 \implies R_w = \frac{D-1}{\epsilon}\mathcal{S}_0^{D=1}. \tag{2.21}$$

The smaller the difference in energy, the larger is the radius of the bubble, which justifies our approximation. That is why this limit is called "the thin wall approximation", although I am personally in concordance with Weinberg [93], in the sense that a better term could have been "the big bubble approximation". The final value of the action is given by

$$\mathcal{S}_0 = \frac{\left(\sqrt{\pi}\,\mathcal{S}_0^{D=1}\right)^D}{\Gamma\left(1+\frac{D}{2}\right)}\left(\frac{D-1}{\epsilon}\right)^{D-1}. \tag{2.22}$$

As expected, the action increases for small ϵ^{D-1}, so the decay rate is strongly suppressed.

In what follows, we proceed to obtain $\mathcal{S}_0^{D=1}$ and the value of the action for a particular potential. As the damping term in eq. (2.13) is inversely proportional to ρ, the evolution of the field (2.13) around R_w can be approximated to

$$\ddot{\varphi}_w(\rho) \approx \frac{\partial V}{\partial \varphi_w} \implies \frac{1}{2}\dot{\varphi}_w^2 = V - V_{FV}\,, \tag{2.23}$$

where V_{FV} is the constant of integration, such that the last term of eq. (2.14) is satisfied and the last term has been obtained as in (2.5)[2]. This implies that

$$\frac{\mathrm{d}\varphi}{\mathrm{d}\rho} = \sqrt{2\left(V - V_{FV}\right)} \implies \mathcal{S}_0^{D=1} = \int_{\varphi_-}^{\varphi^+} \mathrm{d}\varphi\sqrt{2\left(V - V_{FV}\right)}, \tag{2.24}$$

which can be computed before obtaining $\varphi_w(\rho)$.

To move on and provide an explicit expression for φ_w, we have to define a specific form of the potential. For this purpose, let us consider for instance a general renormalizable potential in $D = 4$, the linear off-set quartic:

$$V(\varphi) = \frac{\lambda}{8}\left(\varphi^2 - v^2\right)^2 + \epsilon\left(\frac{\varphi - v}{2v}\right), \tag{2.25}$$

where λ and v are positive parameters of the model and $V_{FV} = 0$. On the wall, the small off-set can be neglected $V(\varphi_w) \approx V|_{\epsilon=0}$. Thus, from (2.22), (2.24) and (2.25) we get[3]

$$\varphi_w = v\tanh\left(\frac{1}{2}v\sqrt{\lambda}\,(\rho - R_w)\right), \quad \mathcal{S}_0^{D=1} = \frac{2v^3\sqrt{\lambda}}{3}, \quad \mathcal{S}_0 = \frac{8\pi^2 v^{12}\lambda^2}{3\epsilon^3}, \tag{2.26}$$

This concludes our thin wall example. Note that when the energy difference $\epsilon \to 0$, the action $\mathcal{S}_0 \to \infty$, and the decay rate $\Gamma \to 0$. This implies that there is no tunneling when the minima are degenerate.

[2]In section 2.2 we saw that we can always redefine the potential such that $V_{FV} = 0$ without loss of generality.

[3]The author of the original work [68] also missed a factor of two in $\mathcal{S}_0^{D=1}$, eq. (4.12).

2.4 Re-scaling properties and Derrick's Theorem

Since $\bar{\varphi}(\rho)$ is the solution of the equation of motion that extremizes the action, it must be stationary with respect to any perturbation. Then from the re-scaling properties of the bounce action, we can obtain a non-trivial relation between the integrated kinetic and potential parts in (2.12).

For this purpose, we use a similar argument that was used to prove Derrick's theorem [113] and consider the action (2.12) for a modified bounce field $\bar{\varphi}(\rho) \equiv \varphi_\lambda(\rho/\lambda)$. After rescaling the variable of integration, we get

$$\mathcal{S}_0^{(\lambda)} = \frac{2\pi^{\frac{D}{2}}}{\Gamma\left(\frac{D}{2}\right)} \int_0^\infty \rho^{D-1} \mathrm{d}\rho \left(\frac{\lambda^{D-2}}{2} \left(\frac{\mathrm{d}\varphi_\lambda}{\mathrm{d}\rho} \right)^2 + \lambda^D V \right) \quad = \lambda^{D-2}\mathcal{T} + \lambda^D \mathcal{V}. \tag{2.27}$$

The variation with respect to λ must vanish at the bounce solution, i.e. when $\lambda = 1$. That is, for the action to remain minimal upon rescaling the argument of the solution to $\varphi(\rho/\lambda)$, the following identity has to hold

$$\left. \frac{\delta \mathcal{S}_0^{(\lambda)}}{\delta \lambda} \right|_{\lambda=1} = 0 \implies \mathcal{T} = -\frac{D}{D-2}\mathcal{V}\,, \tag{2.28}$$

from which follows that

$$\mathcal{S}_0 = \frac{2\mathcal{T}}{D} > 0\,. \tag{2.29}$$

We will use these results in chapter §3 to obtain the bounce field using our new method and test the goodness of our results.

Going a bit further, we can see that the second variation of the bounce action with respect to λ is

$$\left. \frac{\delta^2 \mathcal{S}_0^{(\lambda)}}{\delta \lambda^2} \right|_{\lambda=1} = 2(2-D)\mathcal{T}, \tag{2.30}$$

which is negative[4] for $D > 2$. This means that the bounce is not a minimum of the action but rather a saddle point. We will come back to this result in more detail in section §5 when we compute A explicitly.

2.5 Exact solutions of the bounce

The bounce field configuration (2.13) cannot be solved analytically in general, not only because the potential is non-linear in general, but also because of the friction term proportional to $D-1$. In fact, there are very few models that are simple enough to be solved in a closed-form. This includes the Fubini-Lipatov instanton [114, 115], its generalization [116], the pure quartic potential [117], the binomial and logarithmic one [118, 119, 120].

There are also other types of closed-form solutions that can be obtained from the merging of two or more exact solutions, describing a potential with two minima. For

[4] This is the essence of Derrick's theorem about the non-existence of stable localized stationary solutions for a real scalar field in three and higher space-time dimensions.

instance, one linear segment with a quartic potential or bi-quadratic potential [121], bi-linear segments [122] or bi-quartic potential [123].

These last two simple models constitute the building blocks of my research and are briefly described in detail below.

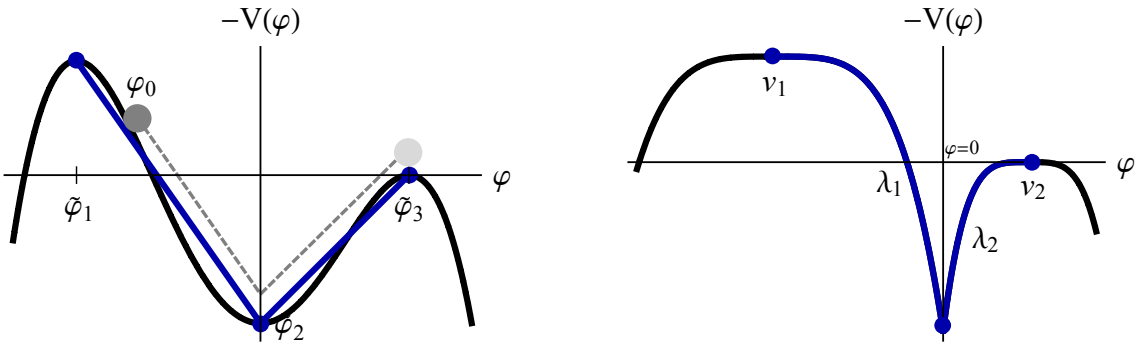

Figure 2.4: Left: The piece-wise linear potential with two segments in blue, superimposed on the potential in gray. Right: The bi-quartic potential.

2.5.1 The triangular potential

One of the simplest exact bounce solutions that describes a potential with two minima is the triangular potential. It consists on two linear potentials that join the TV $\tilde{\varphi}_1$, a middle point $\tilde{\varphi}_2$ and the FV $\tilde{\varphi}_3$. It is shown by the blue line on the left panel of fig. 2.2. The solution of eq. (2.13) for each linear segment in $D = 4$, with slope $dV_s/d\varphi = 8a_s$ is

$$\varphi_s(\rho) = v_s + a_s\rho^2 + \frac{b_s}{\rho^2}, \qquad 8a_s = \frac{\tilde{V}_{s+1} - \tilde{V}_s}{\tilde{\varphi}_{s+1} - \tilde{\varphi}_s}, \tag{2.31}$$

Here, $\tilde{V}_s = V(\tilde{\varphi}_s)$, and b's and v's are the constant of integration. We now proceed by rewriting the boundary conditions (2.14) and then solving the system of equations to get the bounce field configuration.

Since the potential is not infinitesimally smooth in the vicinity of the TV, the solution at the first segment either starts from φ_0 at $\rho = R_0 = 0$ or waits at $\tilde{\varphi}_N$ until some initial radius $\rho = R_0$ with $\dot{\varphi}_1(R_0) = 0$. That is,

$$\text{case a):}\ v_1 = \varphi_0, \qquad b_1 = 0, \tag{2.32}$$
$$\text{case b):}\ v_1 = \tilde{\varphi}_1 - 2a_1R_0^2, \qquad b_1 = a_1R_0^4. \tag{2.33}$$

Then the field evolves and reaches the intersection point $\tilde{\varphi}_2$ at some value $\rho = R_1$, where we require the field to be continuous and differentiable,

$$\varphi_1(R_1) = \varphi_2(R_1) = \tilde{\varphi}_2, \qquad \dot{\varphi}_1(R_1) = \dot{\varphi}_2(R_1)\ . \tag{2.34}$$

Finally, the field stops in $\tilde{\varphi}_3$ at some final radius R_3 such that $\varphi_2(R_3) = \tilde{\varphi}_3$ and $\dot{\varphi}(R_3) = 0$, which imply

$$v_2 = \tilde{\varphi}_3 - 2a_1R_2^2, \qquad b_2 = 2a_2R_2^4. \tag{2.35}$$

These sets of equations are simple and solvable in a closed-form. The three matching conditions in (2.34) are used to solve the remaining unknowns:

$$\text{case a): } \varphi_0 = \frac{\tilde{\varphi}_3 + c\,\tilde{\varphi}_2}{1+c}, \qquad R_1^2 = \left(\frac{\tilde{\varphi}_2 - \varphi_0}{a_1}\right), \quad R_2^2 = R_1^2\left(\frac{a_2 - a_1}{a_2}\right)^{\frac{1}{2}}, \tag{2.36}$$

$$\text{case b): } R_0^2 = R_1\left(R_1 - \Delta_2\right), \quad R_2^2 = R_1\left(R_1 + \Delta_3\right), \quad R_1 = \frac{1}{2}\frac{a_1\Delta_2^2 + a_2\Delta_3^2}{a_1\Delta_2 + a_2\Delta_3}, \tag{2.37}$$

with $c = -2 + \left(1 - \sqrt{1 - \frac{a_1}{a_2}}\right)\frac{2a_2}{a_1}$ and $\Delta_s^2 = \left(\tilde{\varphi}_s - \tilde{\varphi}_{s-1}\right)/|a_{s-1}|$. Demanding that all the radii must be positive and real, we end up with a simple unique solution such that: if $R_0 > 0$ we are in case b), otherwise it is case a).

The associated action can be obtained from (2.12) and (2.31) as

$$\mathcal{S}_0 = 2\pi^2 \sum_{s=1}^{2}\left[\frac{5}{3}a_s^2\rho^6 - \frac{2}{3}a_s b_s \rho^2 - \frac{b_s^2}{\rho^2} + \frac{\rho^4}{4}\left(8a_s\left(v_s - \tilde{\varphi}_s\right) + \tilde{V}_s - \tilde{V}_N\right)\right]_{R_{s-1}}^{R_s}. \tag{2.38}$$

These results can be used to estimate the decay rate of any potential. It was proved that it reproduces the result of Coleman [68] in the thin wall limit [122]. However, it might not be a good approximation in general as it was claimed by [124] for a single field and [125] for multi-field potentials.

In the next chapter, we will show how to generalize this result to any type of potential and space-time dimensions up to desired precision by using an analogous derivation.

2.5.2 The bi-quartic potential

Let us consider two quartic potentials, joined at $\varphi = 0$ with the minima located at $-v_1$ and v_2,

$$V = \frac{1}{4}\left(\lambda_2 v_2^4 - \lambda_1 v_1^4 + \lambda_1\left(\varphi + v_1\right)^4\right)H(-\varphi) + \frac{\lambda_2}{4}\left(\varphi - v_2\right)^4 H(\varphi), \tag{2.39}$$

where H is the step function, $\lambda_{1,2} > 0$ and $v_2 > 0$ is the FV with $V(v_2) = 0$, as shown on the right panel of fig. 2.2. For $v_1 > 0$ to be the TV, we require $\lambda_1 v_1^4 > \lambda_2 v_2^4$ such that $V(v_1) < 0$. The potential derivative and its bounce solution for each segment is given by

$$V_s' = \lambda_s\left(\varphi_s - (-1)^s v_s\right)^3, \qquad \overline{\varphi}_s = (-1)^s v_s + \sqrt{\frac{8}{\lambda_s}}\frac{R_s}{R_s^2 - \rho^2}. \tag{2.40}$$

Before solving the boundary conditions, let us define for convenience two dimensionless quantities x and y from $v_1 = x\,v_2 = x\,v$, and $\lambda_1 = y\,\lambda_2 = y\,\lambda$, with its associated constraints $x > 0$, $y > 0$ and $x^4 y > 1$.

Near the equality $x^4 y \simeq 1$, we approach the TW limit, where the minima are degenerate and the rate vanishes. The bounce parameters $R_{1,2,T}$ are obtained by matching the solution to $\varphi = 0$, and requiring $\overline{\varphi}$ to be continuous and differentiable at $\rho = R_T$. The resulting Euclidean radii are

$$R_{1,2,T} = \frac{2}{v}\sqrt{\frac{2}{\lambda}}\frac{1+x}{x^4 y - 1}\left(x^2\sqrt{y}, 1, \sqrt{\frac{x(1+x^3 y)}{1+x}}\right). \tag{2.41}$$

Their size is set by the factorized $1/v$, as expected on dimensional grounds since v is the relevant mass scale. Moreover, the radii are positive and diverge in the TW limit of $x^4 y \to 1^+$ as expected.

The bounce action is

$$\mathcal{S}_0 = \left(\frac{8\pi^2}{3\lambda}\right) \frac{1 + y + x^3 y \left(4 + xy \left(-3 + 6x^2 + (3 + 4x)x^4 y\right)\right)}{y(x^4 y - 1)^3}\,, \tag{2.42}$$

where the factor of $8\pi^2/(3\lambda)$ is the well known single quartic result, which gets multiplied by a function that diverges in the TW when $x^4 y \to 1$.

In the next chapters, this bounce solution will be used as an additional test of the polygonal method. This solution is also of fundamental importance for the chapter §5.3, as we show that we can go even further analytically and compute one loop corrections in a closed-form.

2.6 Evolution of the bubble in Minkowski space

Before we move on to more general bounce solutions, let us examine the real time evolution of the classical field after the false vacuum decay has taken place. In other words, we would like to obtain the behavior of the field after it materializes at φ_0 and evolves according to the Minkowskian field equation,

$$\left(\nabla^2 - \partial_0^2\right) \varphi = V'(\varphi)\ . \tag{2.43}$$

The initial boundary conditions are provided by the bounce field $\bar{\varphi}$ at a given time t_0,

$$\varphi(t_0, \mathbf{x}) = \bar{\varphi}(|\mathbf{x}|)\,, \qquad\qquad \partial_0 \varphi(t_0, \mathbf{x}) = 0\,. \tag{2.44}$$

Solving this set of equations might seem a difficult task. However, these specific boundary conditions do not break Lorentz invariant. The $O(4)$ invariance of the bounce leads to a $O(1,3)$ Lorentz symmetry solution φ. Thus, similar to ρ in the bounce equation, we can conveniently define the parameters $\tau_\pm^2 = \pm(-t^2 + \mathbf{x}^2)$. Then the differential equation (2.43) splits into two possible situations: when $x > t$ space-like events and when $t > x$ time-like events. In the former case we choose τ_+, where the equation of motions (2.43) become simply the analytic continuation of the Euclidean bounce equation (2.13) with $\rho \to \tau_+$. That is,

$$\frac{d^2\varphi}{d\tau_+^2} + \frac{D-1}{\tau_+}\frac{d\varphi}{d\tau_+} = \frac{dV}{d\varphi}. \tag{2.45}$$

Thereby, the solution is then the analytic continuation of the bounce field configuration

$$\bar{\varphi}\left(\tau_+ = \sqrt{-t^2 + x^2}\right), \tag{2.46}$$

where we assumed that $\tau_+ > 0$.

In the latter case τ_+ is imaginary, so we consider τ_-. The field equations (2.43) are given by

$$\frac{\mathrm{d}^2\varphi}{\mathrm{d}\tau_-^2} + \frac{D-1}{\tau_-}\frac{\mathrm{d}\varphi}{\mathrm{d}\tau_-} = -\frac{dV}{d\varphi}\,, \tag{2.47}$$

which correspond to the bounce equation with $\rho \to i\tau_+$.

Here, the sign of $\tau_\pm$ does not affect the field equations. However, we defined the sign conveniently such that we can drop the index and consider a single real parameter τ. This definition of τ defines the light cone to be at the center of the bubble $\bar{\varphi}(\tau = 0) = \varphi_0$.

In both cases, the classical field is subjected to a damping term as a consequence of this intrinsic symmetry. This is not preserved in general for other types of initial conditions or Euclidean solutions that are not rotationally invariant. They correspond to sub-dominant contributions and are not subject to this section.

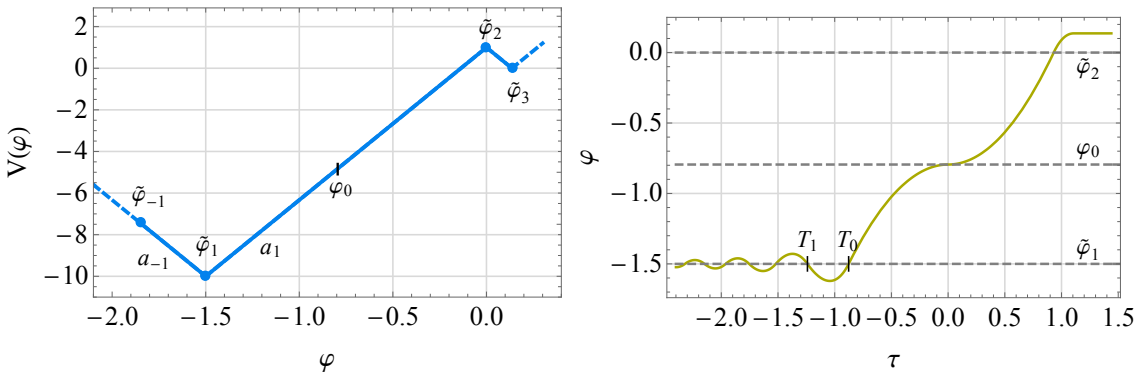

Figure 2.5: Left: The triangular potential with an extra segment with slope a_{-1} at the true vacuum to include the downward movement of the classical field. Right: The classical field configuration after the materialization of the bubble corresponding to the potential on the left.

Each value of the field described by eq. (2.45) and (2.47) must look the same for any Lorentz observer. Thereby, the growth of the bubble will trace out a hyperboloid in space-time, as shown on the left panel of fig. 2.6. This implies that after the bubble is created, it will expand quickly to almost the speed of light.

In short, after the materialization, the evolution of the field inside the light cone is described by the bounce continued to Minkowski space, while outside the light cone, it is given by the subsequent evolution of the field rolling down the hill and oscillating around the true minimum.

Let us proceed with an explicit example by the use of the triangular closed-form solution in $D = 4$, described in section §2.5 and assume that the field tunnels "far" from the true minimum. The potential is shown in the left panel of fig. 2.5, where we have included an extra segment, joined to the true vacuum to include the damped oscillations of the classical field.

The bounce field configuration obtained in (2.13) describes the space-like connected events $\tau > 0$ of an observer at the center of the bubble in φ_0. The other part of the space-time $\tau < 0$, is defined by the field rolling downwards to $\tilde{\varphi}_1$ described by (2.47) and with the initial conditions $\varphi(\tau = 0) = \varphi_0$ and $\dot{\varphi}_0 = 0$. As in section §2.5, we can get the evolution of the field by simply connecting solutions of a linear potential, as developed in [121]. The classical field reaches the true vacuum $\tilde{\varphi}_1$ repeatedly at $\varphi(T_s) = \tilde{\varphi}_1$, given by

$$T_0 = -\sqrt{\frac{\tilde{\varphi}_1 - \varphi_0}{a_1}}\,, \qquad T_{s-1} = -\sqrt{T_s^2 - \frac{\dot{\tilde{\varphi}}_s T_s}{2a_s}}\,, \qquad \dot{\tilde{\varphi}}_{s-1} = -\dot{\tilde{\varphi}}_s \frac{T_s}{T_{s-1}}\,, \tag{2.48}$$

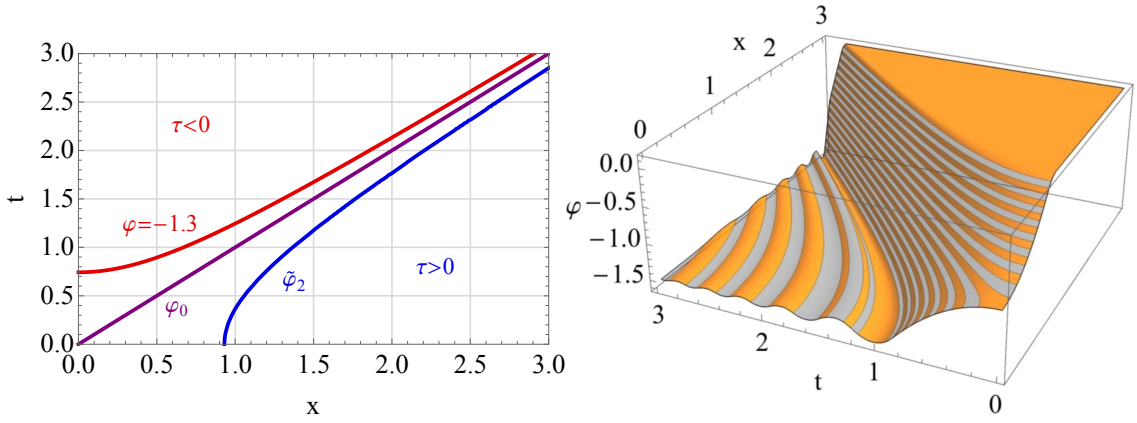

Figure 2.6: Left: The expansion of the bubble in Minkowski space-time for particular values of the classical solution φ. Right: The expansion of the bubble for any space, time and field values.

with $a_{-2s-1} = a_1 > 0$ and $a_{-2s} = a_0 < 0$, defined by $8a_s = \left(\tilde{V}_{s+1} - \tilde{V}_s\right) / (\tilde{\varphi}_{s+1} - \tilde{\varphi}_s)$. The other coefficients of the classical solution are obtained after solving the continuity and differentiability conditions at T_s,

$$b_{s-1} = a_s T_s^4 - \frac{1}{2}\dot{\tilde{\varphi}}_s T_s^3\,, \qquad v_{s-1} = \tilde{\varphi}_1 - 2a_s T_s^2 + \frac{1}{2}\dot{\tilde{\varphi}}_s T_s\,, \tag{2.49}$$

where the even(odd) numbers of s stand for the bounce solution on the right(left) side of the minimum. The complete evolution of the classical field is given in a closed-form

$$\varphi_s(\tau) = \begin{cases} v_s + a_s\tau^2 + b_s\tau^{-2}, & T_{s-1} \le \tau < T_s\,, \\ \varphi_0 + a_1\tau^2, & T_0 \le \tau < 0\,, \\ \bar{\varphi}(\tau)\,, & 0 \le \tau < \infty\,. \end{cases} \tag{2.50}$$

as it is shown on the right panel of fig. 2.5. The left panel of fig. 2.6 shows the evolution of particular values of the classical field in space-time, while the right panel displays the complete evolution of the classical solution in space-time for any value of the field. As expected, the oscillations around the true vacuum $\bar{\varphi}_1$ are damped. If the initial conditions (2.44) were not $O(1,3)$ invariant, equation (2.43) might allow harmonic oscillations. In this case, it could drive interesting phenomena such as resonant tunneling [126, 127, 128, 129, 130].

In the next chapter, we will obtain a generalization of this triangular solution to different space-time dimensions, multiple segments, and number of fields. There, the ρ dependence is also given explicitly, which allows us to analytic continue the solution to Minkowski space, as achieved in the previous example.

Chapter 3

Polygonal bounce: from single to multifield decay rate

3.1 Introduction

As pointed out in §2.2, the main difficulty with the usual shooting approach is finding the fine-tuned initial field value φ_0, which is even more challenging in the multidimensional field space.

We solve these issues by developing a new semi-analytical approach for computing tunneling rates in quantum or thermal field theory with multiple scalar fields [131]. It is based on gluing an arbitrary number of linear segments into a polygonal potential and solving the resulting system for any dimension and number of fields. As we will see, by increasing the number of segments one can approximate any potential that admits a bounce solution and obtain the bounce action with arbitrary precision.

The method is first developed in §3.2 for the single field case in D space-time dimensions. We discuss how this approach is implemented, show its validity on well known examples and compare it with existing tools in §3.3. Then a systematic expansion of the potential beyond the linear order is considered, taking into account higher-order corrections, which sets the basics for the multiple scalar fields developed in §3.5. We conclude with an outlook in §3.6 and leave details to appendices: dimensions other than $D = 3, 4$ are covered in A.1, the two segments calculation is expanded in A.2 and further details on root finding can be found in A.3.

3.2 Single field polygonal bounces

In this section we present the polygonal bounce (PB) with an arbitrary number of segments and space-time dimensions by extending the triangular potential described in §2.5.1.

To establish the notation, let us consider a generic potential with two minima $V(\varphi)$, to be approximated by piecewise linear potentials, as shown in fig. 3.1. The segment index for the field values $\tilde{\varphi}_s, s = 1, \ldots, N$, are such that the FV is at $\tilde{\varphi}_1$, the TV at $\tilde{\varphi}_N$ and the values of the potential are $\tilde{V}_s = V(\tilde{\varphi}_s)$. The linear segments

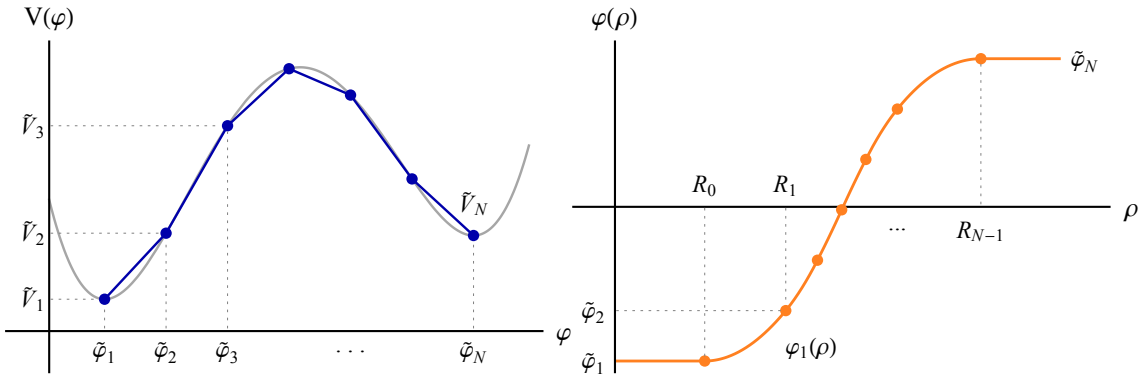

Figure 3.1: Left: Linearly off-set quartic potential in gray and the polygonal approximation with $N = 7$ in blue. Right: The bounce field configuration corresponding to the potential on the left, computed with the polygonal bounce approximation.

are simple

$$V_s(\varphi) = \underbrace{\left(\frac{\tilde{V}_{s+1} - \tilde{V}_s}{\tilde{\varphi}_{s+1} - \tilde{\varphi}_s}\right)}_{8\,a_s} (\varphi - \tilde{\varphi}_s) + \tilde{V}_s, \tag{3.1}$$

where each segment admits an exact solution in $D > 2$ space-time dimensions as,

$$\varphi_s(\rho) = v_s + \frac{4}{D} a_s \rho^2 + \frac{2}{D-2} \frac{b_s}{\rho^{D-2}}. \tag{3.2}$$

The case for two dimensions requires minor modifications and is derived in A.1.

As in §2.5.1 the polygonal potential is not smooth at the minima either, which implies that the solution either starts from φ_0 at $\rho = 0$ or or waits at $\tilde{\varphi}_1$ until $\rho = R_0$[1]. That is,

$$\text{case a):}\ v_1 = \varphi_0, \qquad b_1 = 0, \tag{3.3}$$

$$\text{case b):}\ v_1 = \tilde{\varphi}_1 - \frac{4}{D-2} a_1 R_0^2, \qquad b_1 = \frac{4}{D} a_1 R_0^D\,. \tag{3.4}$$

Regardless of the initial condition, the field stops in the second minimum $\tilde{\varphi}_N$ at some final radius R_{N-1} such that

$$v_{N-1} = \tilde{\varphi}_N - \frac{4}{D-2} a_{N-1} R_{N-1}^2, \qquad b_{N-1} = \frac{4}{D} a_{N-1} R_{N-1}^D, \tag{3.5}$$

where $a_0 = a_N = 0$, because the first derivatives are zero in the minima. Note that there is no issue when $\rho \to 0$: In case a) the singularity of the friction term is regulated by $b_1 = 0$, while in the case b) there is no singularity as R_0 is non-zero.

Now we proceed to join the set of exact solutions and demonstrate that PB is a single variable problem. Once the segmentation of $\{\tilde{\varphi}_s\}$ is set up, the a_s parameters are fixed by (3.1), as described in the next section §3.3.1. The other bounce parameters v_s, b_s and the unknown radii $R_s, s = 0, \ldots, N-1$ are fixed by the matching

[1]We could have had a single case if the initial segment were quadratic or other function such that $V''(\tilde{\varphi}_1) \neq 0$.

conditions. Requiring the bounce to be a single smooth solution, as in fig. 3.1, we get three conditions per segment: two for the field value to match onto the initial segmentation at R_s and another one for its derivative:

$$\varphi_s(R_s) = \tilde{\varphi}_{s+1} = \varphi_{s+1}(R_s), \qquad \dot{\varphi}_s(R_s) = \dot{\varphi}_{s+1}(R_s). \tag{3.6}$$

This set of conditions precisely determines the unknown v_s, b_s and R_s and they are analogous to (2.34). Thereby, one can increase the number of sections at will without introducing additional free parameters. Solving this system of equations per segment we get,

$$v_{s+1} = v_s - \frac{4}{D-2}\left(a_{s+1} - a_s\right) R_s^2, \qquad b_{s+1} = b_s + \frac{4}{D}\left(a_{s+1} - a_\sigma\right) R_s^D, \tag{3.7}$$

with the individual radii given by

$$a_s R_s^D - \frac{D}{4}\delta_s R_s^{D-2} + \frac{D}{2(D-2)} b_s = 0, \tag{3.8}$$

with $\delta_s = \tilde{\varphi}_{s+1} - v_s$. Resulting Eq. (3.8) is a fewnomial with simple closed form solutions

$$D = 3: \qquad 2R_s = \frac{1}{\sqrt{a_s}}\left(\frac{\delta_s}{\xi} + \xi\right) \quad \text{with} \quad \xi^3 = \sqrt{36 a_s b_s^2 - \delta_s^3} - 6\sqrt{a_s} b_s\,, \tag{3.9}$$

$$D = 4: \qquad 2R_s^2 = \frac{1}{a_s}\left(\delta_s + \sqrt{\delta_s^2 - 4 a_s b_s}\right). \tag{3.10}$$

The radii corresponding to $D = 2, 6, 8$ can be found in Eqs (A.7)-(A.9) of A.1. These equations guarantee that we are dealing with a single variable problem: once the initial condition R_0 or the final one R_N radius is given, the whole solution is known. As anticipated, so far we have solved analytically each constant of integration except for one, which we conveniently choose it to be the initial radius R_0. In section §3.3 we will show how to obtain this parameter numerically.

The associated Euclidean action of the bounce becomes a sum of linear parts

$$\mathcal{S}_0 = \mathcal{T} + \mathcal{V}, \tag{3.11}$$

with the integrated kinetic and potential pieces

$$\mathcal{T} = \frac{2\pi^{\frac{D}{2}}}{\Gamma\left(\frac{D}{2}\right)} \sum_{s=0}^{N-1} \left[\rho^2 \left(\frac{32 a_s^2 \rho^D}{D^2(D+2)} - \frac{8}{D} a_s b_s - \frac{2 b_s^2}{\rho^D (D-2)}\right)\right]_{R_{s-1}}^{R_s}, \tag{3.12}$$

$$\mathcal{V} = \frac{2\pi^{\frac{D}{2}}}{\Gamma\left(\frac{D}{2}\right)} \sum_{s=0}^{N-1} \left[\frac{\rho^D}{D}\left(8 a_s \left(v_s - \tilde{\varphi}_s\right) + \tilde{V}_s - \tilde{V}_N\right) + \rho^2 \left(\frac{32 a_s^2 \rho^D}{D(D+2)} + \frac{8 a_s b_s}{D-2}\right)\right]_{R_{s-1}}^{R_s}, \tag{3.13}$$

which is valid for $D > 2$ and both cases a) and b), with the understanding that $R_{-1} = 0$ in case b) and $R_0 = 0$ for case a). This concludes the analytic setup of the PB construction.

Derrick's theorem for piecewise actions. We will apply the same idea that was used to prove Derrick's theorem, described in §2.4, to find the PB solution and to test the goodness of the approximation. For piecewise actions, such as the PB under consideration, the above identity is modified because (3.11) becomes a sum of finite integration intervals. Unlike the continuous limit (2.27), the rescaling $\rho \to \rho/\lambda$ affects the finite integration limits $R_s \to R_s/\lambda$ in (3.11), which introduces a manifest λ dependence. As a result,

$$\mathcal{S}^{(\lambda)}_{0,\mathrm{PB}} = \sum_s \left(\lambda^{D-2}\mathcal{T}^{(\lambda)}_s + \lambda^D \mathcal{V}^{(\lambda)}_s\right), \qquad \mathcal{T}^{(\lambda)}_s \propto \int_{\frac{R_{s-1}}{\lambda}}^{\frac{R_s}{\lambda}} \rho^{D-1} \mathrm{d}\rho\, \dot{\varphi}_s^2, \tag{3.14}$$

and similarly for $\mathcal{V}^{(\lambda)}_s$. Imposing the vanishing derivative of the polygonal $\mathcal{S}^{(\lambda)}_{0,\mathrm{PB}}$ over λ, one obtains a complicated finite version of the identity in (2.27), modifying the relation between $\mathcal{T}^{(\lambda)}_s$ and $\mathcal{V}^{(\lambda)}_s$. However, with a sufficiently large number of segments, the relation (2.27) with $\mathcal{T} \to \sum_s \mathcal{T}^{(\lambda)}_s$ and $\mathcal{V} \to \sum_s \mathcal{V}^{(\lambda)}_s$ is quickly recovered.

Inversely, one can use the continuous version of (2.27) with the input potential $V(\varphi)$ to verify the goodness of the polygonal solution. This is shown on the right side of fig. A.1 in A.3, where about a permille level precision of the action is achieved with $N = 400$ segments.

3.3 Evaluating polygonal bounces

3.3.1 Implementation

Overview. Let us turn to the implementation of the PB method. In the work of [122], the bounce equations were cast into an algebraic system and solved in a closed form. The approach followed here instead is to recursively compute the bounce parameters and solve a single boundary condition equation.

The boundary equation is obtained by combining (3.5) with (3.7) and setting $s = N - 1$, which leads to

$$\sum_{\sigma=0}^{N-1} (a_{\sigma+1} - a_\sigma)\, R_\sigma^D = 0, \tag{3.15}$$

valid for all D. Because the R_s are already solved for, the final condition for v_{N-1} holds automatically. Alternatively, one can use the relation in (2.27) with the polygonal potential, and look for the solution of

$$\lambda = \sqrt{\frac{(2-D)\mathcal{T}}{D\mathcal{V}}} = 1. \tag{3.16}$$

In order to solve the boundary equation, either (3.15) or (3.16), one has to find the initial radius R_s from which the subsequent v_s, b_s, R_s are computed recursively until the boundary condition is satisfied. This is the algebraic analog of the shooting method used to solve (3.35) directly.

Adding more segmentation points improves the accuracy of the approximation, but does not exponentially increase the computational burden, timing scales linearly with N.

Segmentation. To set up the polygonal potential approximation, one first chooses a set of field values $\{\tilde{\varphi}_s\}$ that interpolate between the positions between which the tunneling happens, as exemplified in fig. 3.1. Throughout this work we assume the original potential $V(\varphi)$ to be non-pathological in the sense that it admits at least one bounce solution between these two values[2].

To describe an arbitrary potential, enough segments should be taken to capture all the non-linearities with desired precision. In addition, the action converges faster if the segmentation is tailored to a specific potential, i.e. if the density of points increases close to the extrema. This geometrical insight is a particular feature of the polygonal approach and allows for intuitive understanding of the problem prior to the actual calculation of the bounce.

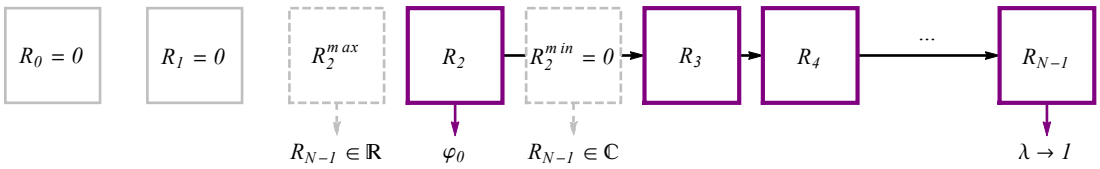

Figure 3.2: Schematic overview of finding the PB. The segment with the solution (in this example $s = 2$ and $R_{in} = R_2$) can be found by evaluating the PB on the boundaries of $R_2^{\min} = 0$ and $R_2^{\max}$ and checking that the imaginary part of the final radius R_{N-1} becomes non-zero. Finally, the solution of R_2 is found such that the scaling parameter $\lambda \to 1$.

For a sufficiently large N, the specific choice of coverage is not relevant. The naïve uniform distribution reproduces any reasonable potential when $N \to \infty$ and converges smoothly to the final value. In this limit, the resolution of $\Delta\tilde{\varphi}_s$ is small enough such that φ_0 always falls above $\tilde{\varphi}_1$ and only case a) persists. This is to be expected because such limit is equivalent to the original problem in (3.35) where $R_0 \to 0$ and only φ_0 matters.

Computing the initial bounce radius. With a given segmentation at hand, one has to find the initial radius R_{in} that solves the boundary equation. Actually, the task can be simplified by a priori isolating the field segment on which the solution exists.

One can see from the right panel of fig. 3.1 that the list of Euclidean radii $\{R_s\}$, must be real, positive and growing (the true minimum is on the left by convention). On the other hand, Eq. (3.15) contains a number of nested roots and becomes progressively non-linear as N grows and generically admits complex solutions for the radii.

Let us demonstrate that the final radius R_{N-1} becomes imaginary as R_{in} is varied across the true solution. This can be understood by noticing that the discriminant $\delta_{N-1}^2 - 4a_{N-1}b_{N-1}$ in (3.10) vanishes due to the boundary conditions in (3.5), likewise for $D = 3$. Thus, when one expands the discriminant around the true solution, only the linear term remains, which will flip the sign of the discriminant and thereby the

[2]The polygonal approach can also be applied to unbounded potentials with a local minimum at $\tilde{\varphi}_N$. In such instance, case b) does not exist, since the field cannot wait at the true minimum. Instead, the choice of the exit point, i.e. $\tilde{\varphi}_1$ must be deep enough for the field, starting from φ_0, to roll down to the false minimum.

imaginary part of the final radius appears, as seen on the left panel of fig. A.1 and shown schematically on fig. 3.2.

Furthermore, note that in both cases a) and b) one only needs to solve for R_{in}, from which the initial field value φ_0 can be determined. In case b) this is merely the position of the minimum $\varphi_0 = \tilde{\varphi}_1$, while in case a), it is obtained from R_{in} and (3.6)

$$\varphi_0 = \tilde{\varphi}_{in+1} - \frac{4}{D} a_{in} R_{in}^2. \tag{3.17}$$

From here one can infer the interval for $R_{in} \in [0, R_{in}^{\max}]$ by setting φ_0 to the lower and upper boundary of the segment in (3.17). The way to find the segment with the solution a priori is therefore to evaluate the final radius from these two limiting R_{in} and checking whether it becomes imaginary, as illustrated in fig. 3.2.

Once the segment containing the solution has been found, one can proceed to solve the polygonal bounce by solving either (3.15) or (3.16). Another approach is to take advantage of the fact that the bounce solution depends solely on R_{in}. This is a dimensional parameter, which can therefore be rescaled by the optimal amount computed from (3.16), which essentially aims to minimize the action. For example, one may begin with $R_{in}^{\max}$, compute the corresponding λ from eq. (3.16), which in general will be different from 1, and proceed by iteration from $R_{in} = \lambda R_{in}^{\max}$. This procedure converges in a few iterations to a permille level. Alternatively, one can solve (3.16) with standard root finding algorithms.

By increasing the number of segments, the initial radius (e.g. R_0 in case b)) decreases until $R_{in} = 0$, when the domain of the solution disappears and one has to switch to the next segment. This agrees with (3.35), as does the fact that the final radius R_{N-1} grows steadily to infinity when $N \to \infty$, see fig. A.2.

3.3.2 Examples, convergence and comparisons

Linearly displaced quadratic potential is the benchmark potential to test the PB method. For this potential the bounce action was obtained in the thin wall approximation in section §2.3. It is defined as in the work of Coleman [68]

$$V(\varphi) = \frac{\lambda}{8}\left(\varphi^2 - v^2\right)^2 + \epsilon\left(\frac{\varphi - v}{2v}\right), \tag{3.18}$$

and shown on the left panel of fig. 3.1. For convenient numerical evaluation, we set $\lambda = 0.25, v = 1$; other points in parameter space can be obtained by rescaling [132]. For such choice of parameters, varying ϵ from 0.01 to 0.08 covers all the regions of interest, starting from thin wall regime of small ϵ, going to well separated minima until the second minimum disappears.

We now apply the PB method to the potential in (3.18), employing the homogeneous segmentation for simplicity. The first results are the φ_0 and R_0 that attempt to solve (3.15). The solution for R_0 varies with N, therefore we show the behavior of $R_0^{(N)}/R_0^{(3)}$ in fig. 3.3, where $R_0^{(N)}$ is the initial radius corresponding to some fixed N. For any choice of ϵ, the R_0 decreases with N and eventually drops to zero, as seen in fig. 3.3. At this point, one has to switch from b) to a)[3].

[3]This is true in general when N is sufficiently large. The reverse transition from a) to b) is also possible when N is small enough and a particular segmentation is chosen. This happens for $\epsilon = 0.07$ in $D = 4$, as shown on the right panel of fig. 3.3.

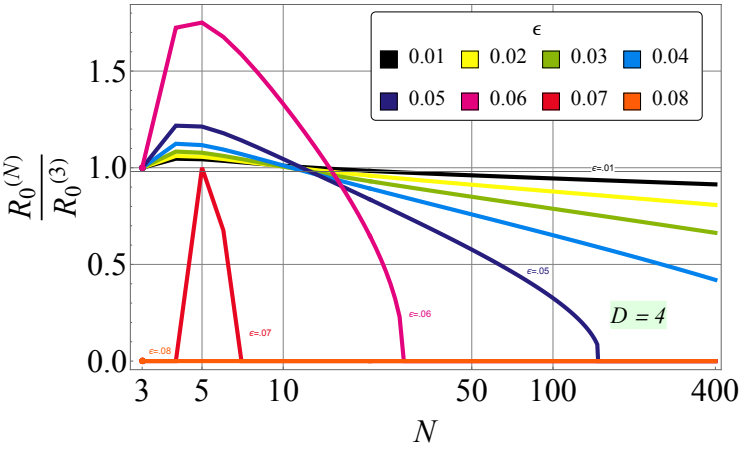

Figure 3.3: The initial radius $R_0^{(N)}$ of case b) and $D = 4$ for the uniform segmentation with N points, normalized to the minimal $N = 3$ setup. Similar behavior appears for $D = 3$. Different lines correspond to the range of ϵ, which controls the separation between the minima in (3.18), see text for details.

The smaller ϵ is, the closer one goes towards the thin wall regime, where the field needs to wait close to the minimum. This means R_0 remains sizeable for higher values of N and one needs to introduce many segments for R_0 to reach zero, as clear from fig. 3.3. On the other hand, the transition from b) to a) happens faster when ϵ increases. Finally, when ϵ is large enough, the transition eventually disappears and we are left with case a) right from the start at $N = 3$.

The number of dimensions also has an impact on the transition from b) to a), as seen in fig. 3.3. Keeping ϵ fixed, the transition in $D = 4$ occurs for higher N with respect to $D = 3$. This is expected because the damping term in (3.35) is proportional to D and thus becomes more important in higher dimensions.

The final step after obtaining R_0 or φ_0 is to compute the main object of interest: the Euclidean action $\mathcal{S}_0$ in (3.11) that sets the bubble nucleation rate. fig. 3.4 shows the main point of this work: the convergence of $\mathcal{S}_0^{(N)}$, the action for N segments with $D = 4$ (the results are basically the same for $D = 3$). The $\mathcal{S}_0^{(N)}$ is normalized to the large $N = 400$ value in order to ease the comparison between different ϵ.

In the limit of $\epsilon \simeq 0$ one ends up in the thin wall regime, and therefore $N = 3$ has to produce the correct result of [122], in agreement with the inset of fig. 3.4. With increasing ϵ, the potential in (3.18) will eventually lose the second minimum. For any potential close to this threshold, the resolution of the homogeneous segmentation has to be precise enough to describe the local maximum, otherwise the solution cannot exist a priori. This is precisely what happens in fig. 3.4 for $\epsilon = 0.08$, the $N = 4$ segmentation is too rough to possess an intermediate maximum. In general, the approximation worsens for $4 \leq N < \mathcal{O}(10)$, which is an artefact of the assumed uniform segmentation. Conversely, for higher N, the action starts to converge rapidly and the rate is faster in case b) for smaller ϵ, where the shooting method instead becomes increasingly unstable.

The initial approximations with small Ns, shown in the inset, are already quite close to the end result and are valid at about 10% level. It is clear that the $N = 3$ segmentation always *underestimates* the action and this simple approximation becomes progressively better as ϵ decreases. On the other hand, as N increases,

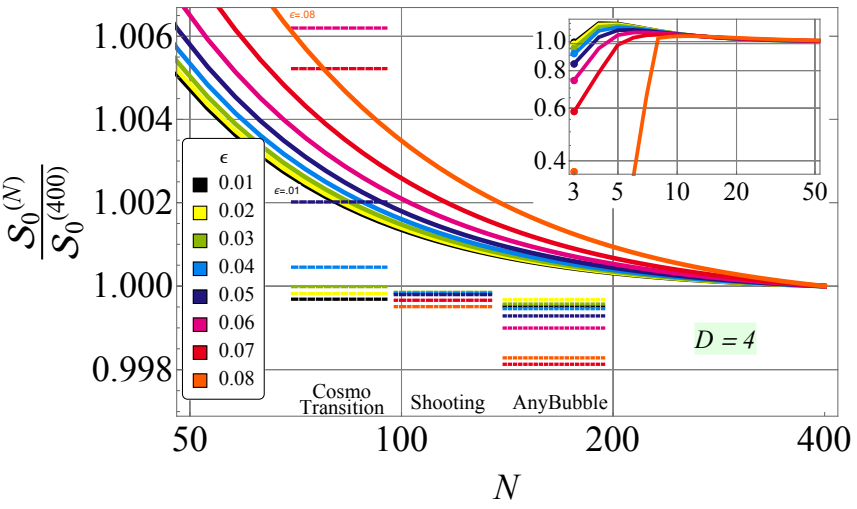

Figure 3.4: The bounce action $\mathcal{S}_0^{(N)}$ normalized to the maximal $N = 400$ uniform segmentation with $D = 4$. The solid lines show the PB method for different ϵ that defines the input potential. The inset shows the same, for a smaller number of segments. The dotted lines show the comparison to other methods and tools, see text for details.

the method starts to *overestimate* the bounce and converges to the final result from above. Even for moderate $N = 10$ the accuracy of the estimation is below 10% and goes below the permille level when $N = 200$. The convergence is slightly faster for $N = 3$, moreover the rate of convergence can be improved by choosing an appropriate segmentation.

To compare the PB method to existing methods, we show the results of other approaches in fig. 3.4. The other three calculations are the usual shooting method of Eq. (3.35) and the out-of-the-box results from CosmoTransitions [82] and AnyBubble [86] packages. Note that in these examples all the methods agree within a few permille level.

In the next chapter, we will provide the reader with more examples and comparisons after presenting our proper tool that implements PB, called `FindBounce`. Before that, let us focus on the main concepts of this method and move on to an analytic extension of PB, which will improve the convergence as we will go beyond the linear segment of potential.

3.4 Extending polygonal bounces

Here we develop a general procedure of including non-linear corrections to the PB. This is done by setting up a systematic procedure based on the Taylor expansion of the potential and then building the new bounce solution perturbatively on the PB ansatz.

Higher order corrections describe non-linear features that are not there in the leading approximation, for example around the extrema of V where the linear part of the potential vanishes. Although the PB solution is formally exact when $N \to \infty$, the nonlinear corrections may enhance the convergence of the action, depending on the type of the potential and the order to which we correct.

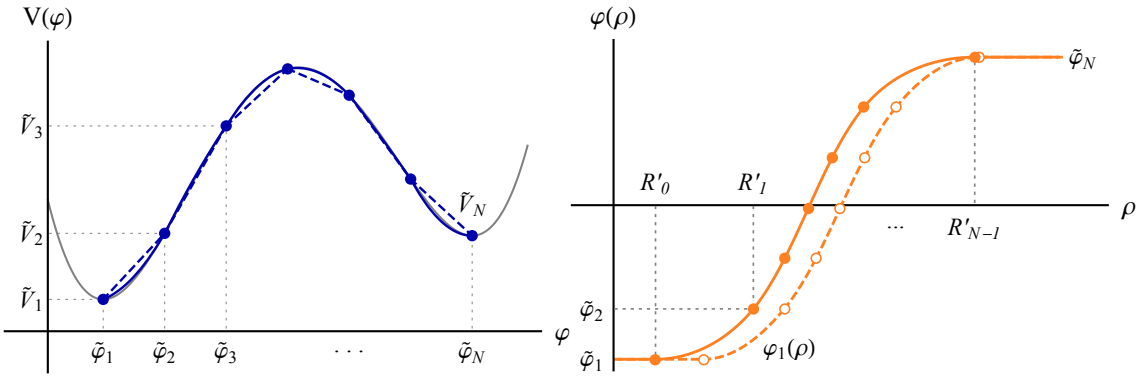

Figure 3.5: Left: The linearly off-set quartic potential in gray, the linear polygonal approximation with $N = 7$ in dashed blue and the 2nd order quadratic correction in solid blue. Right: The field solution in the PB approximation in dashed and the 2nd order improved solution in solid orange.

Generalities. Consider the complete bounce solution expanded around the PB: $\varphi = \varphi_{\rm PB} + \xi$, such that the correction to the potential is evaluated on the PB background and the bounce equation becomes

$$\ddot{\varphi} + \frac{D-1}{\rho}\dot{\varphi} = 8\,(a+\alpha) + \delta dV\,(\varphi_{\rm PB}(\rho))\,, \tag{3.19}$$

$$\ddot{\xi} + \frac{D-1}{\rho}\dot{\xi} = 8\alpha + \delta dV(\rho), \tag{3.20}$$

$$\delta dV = dV(\varphi_{\rm PB}(\rho)) - 8\,(a+\alpha)\,, \tag{3.21}$$

where α is an arbitrary linear part. The bounce correction ξ is then given by

$$\xi = \nu + \frac{2}{D-2}\frac{\beta}{\rho^{D-2}} + \frac{4}{D}\alpha\rho^2 + \mathcal{I}(\rho), \tag{3.22}$$

$$\mathcal{I}(\rho) = \int_{\rho_0}^{\rho} {\rm d}y\, y^{1-D} \int_{\rho_1}^{y} {\rm d}x\, x^{D-1}\delta dV(x). \tag{3.23}$$

Evaluating the above integral $\mathcal{I}$ for an arbitrary δdV and computing the unknown parameters of ξ is involved and basically equivalent to the numerical integration of (3.35). However, a systematic expansion of the potential and linearization simplify this approach considerably.

Perturbation. On a given segment, the potential can be expanded in Taylor series around $\tilde{\varphi}_s$

$$\tilde{V}_s - \tilde{V}_N + \partial\tilde{V}_s\,(\varphi_s - \tilde{\varphi}_s) + \frac{\partial^2\tilde{V}_s}{2}\,(\varphi_s - \tilde{\varphi}_s)^2 + \ldots\,, \tag{3.24}$$

where the constants $\partial V_s, \partial^2 V_s, \ldots$ are determined by matching the values and (higher) derivatives of V. When N increases, the segmentation becomes arbitrarily dense and thus the terms beyond the linear one in (3.24) become progressively negligible.

To illustrate this point, we expand V to second order

$$\partial\tilde{V}_s = 8\,(a_s + \alpha_s)\,, \quad 8\alpha_s = 8a_s - d\tilde{V}_{s+1}, \tag{3.25}$$

$$\partial^2\tilde{V}_s = \frac{d\tilde{V}_{s+1} - \partial\tilde{V}_s}{\tilde{\varphi}_{s+1} - \tilde{\varphi}_s} = \frac{d\tilde{V}_{s+1} - 8\,(a_s+\alpha_s)}{\tilde{\varphi}_{s+1} - \tilde{\varphi}_s}, \tag{3.26}$$

where $d\tilde{V}_s$ stands for the derivative of the original potential evaluated at $\tilde{\varphi}_s$. This is the additional information required from the original potential in order to get to the next-to-leading order. The α_s coefficients are thereby fixed and the inclusion of the quadratic correction improves the fit of the potential near the extrema, as seen from fig. 3.5. Moreover, with a large N, one has $\alpha_s \ll a_s$ as clear from (3.25), which is consistent with the assumption of perturbativity.

With this approximation of the potential, the non-homogeneous part of the correction is

$$\mathcal{I}_s = \int_{\rho_0}^{\rho} \mathrm{d}y\, y^{1-D} \int_{\rho_1}^{y} \mathrm{d}x\, x^{D-1} \partial^2 \tilde{V}_s \left(\varphi_{\mathrm{PB}s} - \tilde{\varphi}_s\right), \tag{3.27}$$

which can be evaluated for $D = 3, 4$

$$\mathcal{I}_s^{D=3} = \partial^2 \tilde{V}_s \left(\frac{v_s - \tilde{\varphi}_s}{6}\rho^2 + b_s\rho + \frac{a_s}{15}\rho^4\right), \tag{3.28}$$

$$\mathcal{I}_s^{D=4} = \partial^2 \tilde{V}_s \left(\frac{v_s - \tilde{\varphi}_s}{8}\rho^2 + \frac{b_s}{2}\ln\rho + \frac{a_s}{24}\rho^4\right), \tag{3.29}$$

where the arbitrary integration constants ρ_0, ρ_1 were chosen to simplify the expression for $\mathcal{I}_s$ without loss of generality because they can be absorbed in ν_s, β_s. The remaining task is to compute the unknown coefficients ν_s, β_s and the new matching radii by requiring the solution to be continuous and differentiable as in the PB case.

Given that φ_{PB} and its matching radii are already close to the actual solution, the new radii have to be close to the previous ones

$$R_s \to R_s\left(1 + r_s\right), \qquad\qquad r_s \ll 1. \tag{3.30}$$

Following the same procedure as in the PB construction above, we set up the modified initial, final and matching conditions for the correction ξ. These conditions are then perturbatively linearized in r_s to get the recursion relations for the parameters

$$\nu_s = \nu_1 - \sum_{\sigma=1}^{s-1} \left(\frac{2}{D-2}\frac{\beta_{\sigma+1} - \beta_\sigma}{R_\sigma^{D-2}} + \frac{4}{D}\left(\alpha_{\sigma+1} - \alpha_\sigma\right)R_\sigma^2 + \mathcal{I}_{\sigma+1} - \mathcal{I}_\sigma\right), \tag{3.31}$$

$$\beta_s = \beta_1 + \sum_{\sigma=1}^{s-1} \left(\frac{4}{D}\left(\alpha_{\sigma+1} - \alpha_\sigma\right) + 4r_\sigma\left(a_{\sigma+1} - a_\sigma\right) + \frac{\dot{\mathcal{I}}_{\sigma+1}\dot{\mathcal{I}}_\sigma}{2R_\sigma}\right) R_\sigma^D, \tag{3.32}$$

and similarly a linear equation for the radius correction at each segment is

$$r_s = \frac{\beta_s + \frac{D-2}{2}\left(\nu_s + \mathcal{I}_s + \frac{4}{D}\alpha_s R_s^2\right) R_s^{D-2}}{(D-2)\left(b_s - \frac{4}{D}a_s R_s^D\right)}. \tag{3.33}$$

Following the same logic as in the PB case above, we compute the initial radius correction r_{in} by solving the linear equation that satisfies the final matching condition. Being a linear equation, this additional step does not require significant computing time but improves the accuracy of the action and speeds up convergence.

Improved action. To understand the effect of second order corrections, we reconsider the usual displaced quartic potential and show the improved action in fig. 3.6.

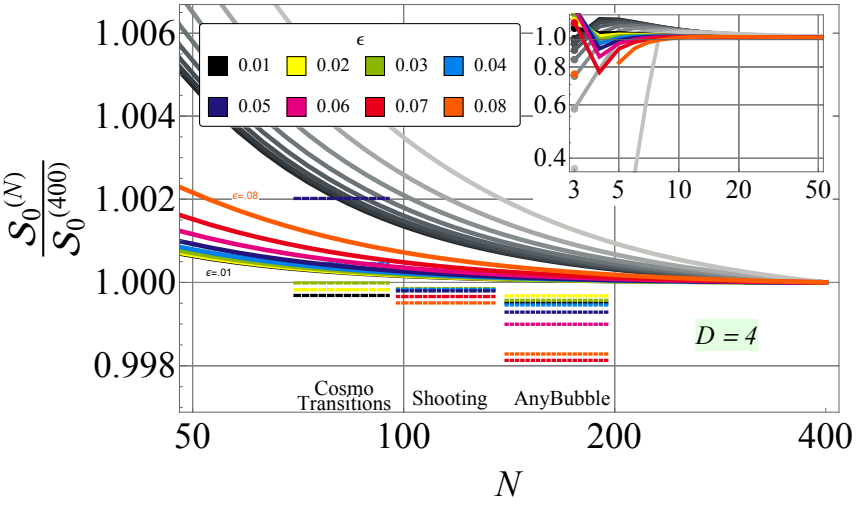

Figure 3.6: The bounce action of the improved bounce calculation including the second order correction. The lower colored lines correspond to the corrected action, while the upper gray ones show the leading PB for comparison.

The correction significantly improves the approximation of the action by nearly an order of magnitude improvement for any given N and ϵ. In other words, to achieve the same level of accuracy one needs to consider half as many segments.

Because the polygonal bounce perturbation requires only to solve a linear equation, the computational cost of computing the bounce solution with a given accuracy is reduced significantly. Moreover, the final result of the bounce field configuration is again given in the form of segmented analytical functions, which allows for further manipulation.

3.5 Multi-field polygonal bounces

The probability of decay of a false ground state in a model with an arbitrary number of real scalar fields φ_i is also proportional to the Euclidean action $\mathcal{S}_0$ and given by (2.1). As shown recently [112], the bounce in the presence of more scalar fields preserves the $O(D)$ invariance, so the Euclidean action (2.12) is naturally extended to more fields,

$$\mathcal{S}_0 = \frac{2\pi^{\frac{D}{2}}}{\Gamma\left(\frac{D}{2}\right)} \int_0^\infty \rho^{D-1}\, \mathrm{d}\rho \left(\frac{1}{2} \sum_i^{n_\varphi} \dot{\varphi}_i^2 + V(\varphi_i) \right), \tag{3.34}$$

where n_φ stands for the number of fields. The bounce fields obey the classical equation and boundary conditions

$$\ddot{\varphi}_i + \frac{D-1}{\rho}\, \dot{\varphi}_i = \partial_i V, \qquad \varphi_i(0) = \varphi_{i0}, \qquad \varphi_i(\infty) = \tilde{\varphi}_{iN}, \qquad \dot{\varphi}_i(0,\infty) = 0, \tag{3.35}$$

where $\partial_i V$ is the derivative of V with respect to φ_i. The analogy of these equations to the motion of a particle in a hypersurface $-V(\varphi_i)$ with a damping terms remains. However, the bounce on multi-field potentials is significantly more challenging as we have to integrate a system of coupled differential field equations.

In principle, once the trajectory in field space is known, the multifield problem reduces to a single field problem. When there are no interactions among the fields, the path in field space is simply a straight line that connects both minima. After a global rotation of the fields, the set of differential equations decouple such that $n_\varphi - 1$ of them are trivially solved by a constant value, while the remaining one becomes an effective single field bounce equation. On the other hand, when there are interactions, the bounce traces a non-trivial curvature in field space and the effective single field bounce becomes a non-trivial combination of the fields. As the bounce extremizes simultaneously the potential and the kinetic terms, the path in field space of the bounce is a trajectory between the straight line that connects both minima and the minimum energy path of the potential, as shown in the fig. 3.7.

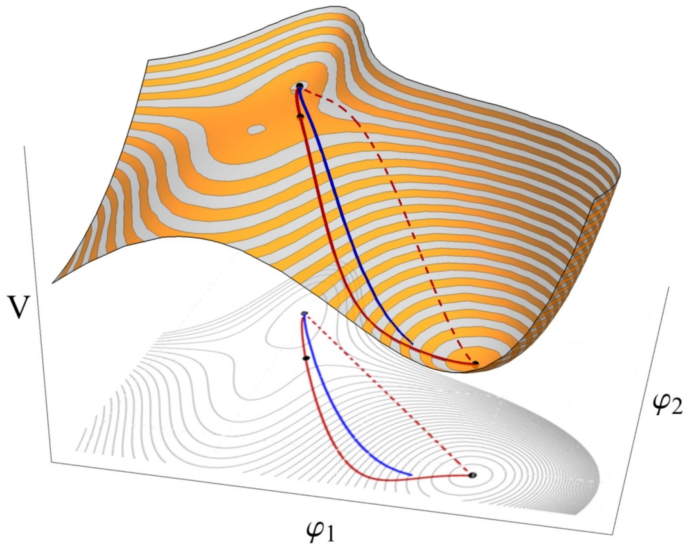

Figure 3.7: An example of a multifield potential with two fields, trajectory of the bounce in blue and its projection on the bottom. Red dashed line is the path in the absence of the potential or interactions among fields, while the solid red one is the path that minimizes the potential.

Computing the false vacuum decay rate with multiple scalar fields faces a number of technical difficulties. These are related to the fact that the Euclidean action is not a minimum but a saddle point. Existing approaches to this problem include an improved action method that converts the saddle point into a minimum [79, 90, 91], numerical functional minimization [80], path deformation and shooting [81, 82], frictionless dimensional continuation [83, 84], semi-analytical techniques [85], multiple shooting [86], tunneling potential [87] and numerically solving coupled PDEs with variable coefficients [88], as well as machine learning techniques [89]. Existing publicly available tools in the literature are: CosmoTransitions [82], AnyBubble [86], BubbleProfiler [88] and SimpleBounce [91]. They are all mostly based on numerical methods.

In general, solutions where the shooting and path deformation are decoupled exhibit oscillatory (and therefore slower) path convergence, multifield shooting faces non-linear scaling with the number fields, and most approaches have difficulties with thin wall regimes. They become either imprecise or impractical for a large number of fields, and provide purely numerical output of the bounce field configuration, as

well as the Euclidean action.

The PB solution overcomes a number of these shortcomings and provides a framework with the following features.

1. The multifield PB field solution remains as simple as in the single field case in (3.2). It is therefore fast to evaluate numerically and is retained upon iteration. The final result has a closed analytical form, which allows for further manipulation.

2. The solution is built iteratively, where a single iteration takes into account the curvature in field space by explicitly solving the ρ dependence and simultaneously deforms the path. This eliminates the oscillatory behavior and the solution converges quickly, within $\mathcal{O}(1)$ iterations, see fig. 3.9.

3. The method works very well in the thin wall limit, which is usually problematic due to severe fine-tuning. This feature is directly inherited from the single field case and is due to the fact that we are solving for the Euclidean time ρ variable and not in φ space. Of course, the method works equally well (see again fig. 3.9) in the thick wall regime; moreover it is applicable to cuspy and unstable potentials, as well as paths with multiple minima.

4. Finding the path in field space boils down to a coupled system of ordinary linear equations that scales linearly with the number of fields and number of segments. The procedure converges very close to the final path even with a few - $\mathcal{O}(1)$ segments. One can switch to more segments in the final step only to ensure sufficient precision in the longitudinal direction, depending on the desired precision of the action.

5. It works for any space-time dimensions $D > 2$ (with $D = 2$ in the Appendix (A.1)), in particular it is simple to consider $D = 3, 4$, which are most relevant for physical applications.

3.5.1 Constructing multi-field polygonal bounces

Let us describe the generalization of the PB approach to an arbitrary number of scalar fields.

The ansatz. The starting point is an initial estimate of the solution,

$$\bar{\varphi}_{is} = \bar{v}_{is} + \frac{2}{D-2}\frac{\bar{b}_{is}}{\rho^{D-2}} + \frac{4}{D}\bar{a}_{is}\rho^2, \tag{3.36}$$

where i is the field index $i = 1, \ldots, n_f$ and $s = 1, \ldots, N$ is the segment point. It is obtained after choosing a path in multi-field space as set of points $\tilde{\varphi}_{is}$, for instance by segmenting a straight line connecting the two minima, as in the left panel of fig. 3.8. Its corresponding longitudinal PB can be computed using sections §3.2 and §3.3 once a_s are given

$$8a_s = \frac{\tilde{V}_{s+1} - \tilde{V}_s}{|\tilde{\varphi}_{is+1} - \tilde{\varphi}_{is}|}, \tag{3.37}$$

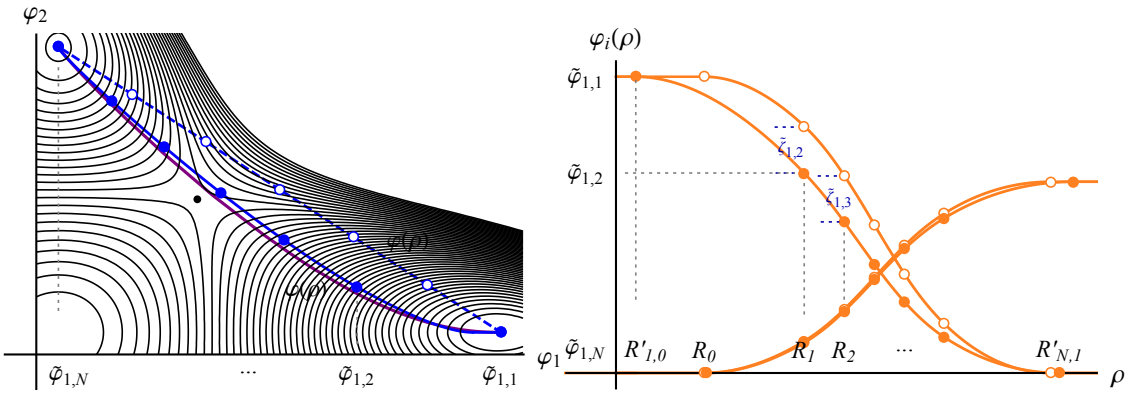

Figure 3.8: The PB solution for two fields in $D = 4$ with $N = 7$ segment points. Left: Path in field space with the initial straight line ansatz $\bar{\varphi}$ with empty circles and the first iteration of the PB solution in solid blue and full circles; the result from shooting is shown in purple. Right: Iterations of the evolution in Euclidean time for $\varphi_1(\rho)$.

Then it is projected back to the multifield space by $e_{is} = (\tilde{\varphi}_{is+1} - \tilde{\varphi}_{is})/|\tilde{\varphi}_{is+1} - \tilde{\varphi}_{is}|$ such that,

$$\bar{v}_{is} = \tilde{\varphi}_{is+1} + e_{is}\left(v_s - \sum_{\sigma=1}^{s}|\tilde{\varphi}_{i\sigma+1} - \tilde{\varphi}_{i\sigma}|\right), \quad 8\,\bar{a}_{is} = e_{is}a_s, \quad \bar{b}_{is} = e_{is}b_s. \tag{3.38}$$

Perturbation of the solution. Next we consider an expansion around the initial estimate, such that $\varphi_{is}(\rho) = \bar{\varphi}_{is} + \zeta_{is}$. This produces a set of coupled bounce equations for each field direction

$$\underbrace{\ddot{\bar{\varphi}}_{is} + \frac{D-1}{\rho}\dot{\bar{\varphi}}_{is}}_{8\bar{a}_{is}} + \underbrace{\ddot{\zeta}_{is} + \frac{D-1}{\rho}\dot{\zeta}_{is}}_{8a_{is}} = \frac{dV}{d\varphi_i}(\bar{\varphi} + \zeta)\,. \tag{3.39}$$

The idea here is to look for a solution of the field expansion ζ, which is of the polygonal type

$$\zeta_{is} = v_{is} + \frac{2}{D-2}\frac{b_{is}}{\rho^{D-2}} + \frac{4}{D}a_{is}\rho^2, \tag{3.40}$$

where a_{is} corresponds to the leading constant expansion of the gradient of the potential around some deformed path, defined by $\tilde{\varphi}_{is} + \tilde{\zeta}_{is}$. This is the main difference in contrast to the single field case: the position in field space is not fixed a priori and one has to allow for the segmentation to move in field space.

The gradient parameters a_{is} can be linearized in terms of the displacement $\tilde{\zeta}_{js}$ with a symmetric average

$$8a_{is} \simeq \frac{dV}{d\varphi_i}\left(\tilde{\varphi}_{is} + \tilde{\zeta}_{is}\right) - 8\bar{a}_{is}, \tag{3.41}$$

$$\frac{dV}{d\varphi_i} \simeq \frac{d_i\tilde{V}_s + d_i\tilde{V}_{s+1} + d_{ij}^2\tilde{V}_s\tilde{\zeta}_{js} + d_{ij}^2\tilde{V}_{s+1}\tilde{\zeta}_{js+1}}{2}. \tag{3.42}$$

It is crucial that the gradient in (3.42) is expanded beyond the constant leading order up to $\mathcal{O}(\tilde{\zeta})$ that includes the second derivative of the potential. This is needed to properly describe curved paths in field space.

Solving the boundary conditions.

Matching. To fix the remaining parameters of the ζ solution in (3.40), the field has to match onto the deformed path. We choose to match to $\tilde{\zeta}$ at the fixed radii R_s, computed from the initial longitudinal polygonal ansatz. This can be done for all the R_s, except for the initial R_{i0} and final ones R_{iN-1}, which are free parameters for each field direction i.

The field values of the ansatz $\bar{\varphi}_{is}$ are continuous from one section to another, while the derivatives may not be. The matching of derivatives at R_s then gives the recursion relation for b_{is}

$$b_{is} = b_{i1} + \sum_{\sigma=1}^{s-1} \frac{4}{D} \left(a_{i\sigma+1} - a_{i\sigma}\right) R_\sigma^D + \frac{1}{2} \left(\dot{\bar{\varphi}}_{i\sigma+1} - \dot{\bar{\varphi}}_{i\sigma}\right) R_\sigma^{D-1}, \tag{3.43}$$

and field continuity, together with (3.43) provides the recursion relation for v_{is}

$$v_{is} = v_{i1} - \sum_{\sigma=1}^{s-1} \frac{4}{D-2} \left(a_{i\sigma+1} - a_{i\sigma}\right) R_\sigma^2 - \frac{1}{D-2} \left(\dot{\bar{\varphi}}_{i\sigma+1} - \dot{\bar{\varphi}}_{i\sigma}\right) R_\sigma. \tag{3.44}$$

Initital/final conditions. In case a) the initial endpoint is free to move, however the solution starts at $\rho = R_{i0} = 0$ with a vanishing derivative, therefore

$$v_{i1} = \tilde{\zeta}_{i1}, \qquad\qquad b_{i1} = 0. \tag{3.45}$$

In case b) the initial endpoint does not move and we have $\varphi_{i1}\left(R_{i0}\right) \simeq \bar{\varphi}_{i1} + \dot{\bar{\varphi}}_{i1} R_0 r_{i0} + \zeta_{i1} = \tilde{\varphi}_{i1}$ that implies $\zeta_{i1}(R_0) = \tilde{\zeta}_{i1} = 0$ because $\dot{\bar{\varphi}}_{i1}(R_0) = 0$. Here we expanded the initial and final radii $R_{i0} = R_0\left(1 + r_{i0}\right)$ and $R_{iN-1} = R_{N-1}\left(1 + r_{iN-1}\right)$ to leading order in $r_{i0,N-1}$, in order to maintain a linear system. As for the derivatives,

$$\dot{\varphi}_{i1}\left(R_{i0}\right) \simeq \dot{\bar{\varphi}}_{i1} + \ddot{\bar{\varphi}}_{i1} R_0 r_{i0} + \dot{\zeta}_{i1} = 8\bar{a}_{i1} R_0 r_{i0} + \dot{\zeta}_{i1} = 0, \tag{3.46}$$

where $\dot{\bar{\varphi}}_{i1} = 0$ and $\ddot{\bar{\varphi}}_{i1} = 8\bar{a}_{i1}$ follows from (7.13). In summary we have the following initial and final conditions:

$$\zeta_{i1}(R_0) = \zeta_{iN-1}(R_{N-1}) = 0, \tag{3.47}$$

$$\dot{\zeta}_{i1}(R_0) = -8\bar{a}_{i1} R_0 r_{i0}, \tag{3.48}$$

$$\dot{\zeta}_{iN-1}(R_{N-1}) = -8\bar{a}_{iN-1} R_{N-1} r_{iN-1}. \tag{3.49}$$

Then the final task is to solve this linear system. The initial conditions are solved in terms of v_{i1} and b_{i1} as

$$v_{i1} = -\frac{4}{D-2}\left(a_{i1} + 2\bar{a}_{i1} r_{i0}\right) R_0^2, \qquad b_{i1} = \frac{4}{D}\left(a_{i1} + D\bar{a}_{i1} r_{i0}\right) R_0^D, \tag{3.50}$$

which determines ζ_{i1} that has to be fixed to $\tilde{\zeta}_{i2}$ at R_1. The recursion relations (3.43) and (3.44) then provide the polygonal ansatz for ζ_{is}, to be fixed onto $\tilde{\zeta}_{is+1}$

$$\zeta_{is}(R_s) = \tilde{\zeta}_{is+1}. \tag{3.51}$$

This continues until the final segment where the endpoint does not move $\tilde{\zeta}_{iN} = 0$, in agreement with (3.47). The final equation to be solved is then the $\dot{\zeta}_{iN-1}$ condition in (3.49), which provides the value of r_{iN-1}. This set of expressions can be written as a system of linear equations to get the new path, which can be solved efficiently and fast.

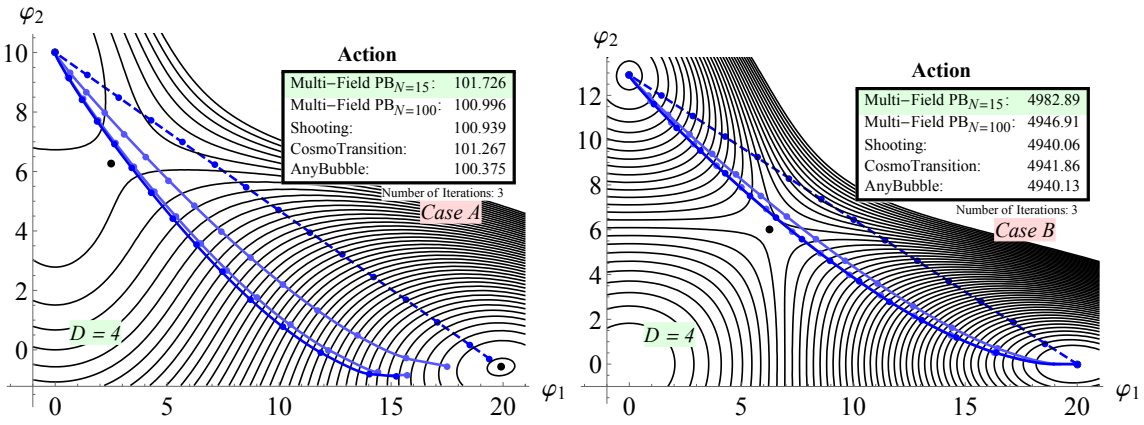

Figure 3.9: Multi-field polygonal solution in $D = 4$ with $N = 15$ segmentation points. The starting ansatz is the straight dashed line connecting the two minima, shown as black dots, together with the saddle point. The solid lines are subsequent iterations that converge to the final path that solves the bounce equations. Insets show the action compared to other approaches. Left: The case a) set-up with the initial endpoint, which is free to move. Right: The case b) potential of the thin wall type with fixed endpoints in the minima.

Iteration. We can perform these steps iteratively until the path in field space does not change anymore, i.e. $\tilde{\zeta}_{is} \simeq 0$. This is simple to achieve by construction since we kept (3.40) with the same polygonal form in ρ.

3.5.2 Examples and path convergence

Let us consider a simple two field potential

$$V(\varphi_i) = \sum_{i=1}^{2} \left(-\mu_i^2 \varphi_i^2 + \lambda_i^2 \varphi_i^4\right) + \lambda_{12} \varphi_1^2 \varphi_2^2 + \tilde{\mu}^3 \varphi_2, \tag{3.52}$$

that has multiple solutions for spontaneous symmetry breaking vevs $\langle \varphi_i \rangle = v_i$. The metastable minima are in general of different depths with $V(v_1) \neq V(v_2)$, which allows for the local false vacuum to decay into the global minimum by traversing the field space along the bounce solution.

To illustrate the multi-field PB method, we choose two exemplary points in the parameter space to cover both non-trivial cases: a) and b). Specifically, we take $\mu_1^2 = 80$, $\mu_2^2 = 100$, $\lambda_1 = 0.1$, $\lambda_2 = 0.3$, $\lambda_{12} = 2$ and $\tilde{\mu}^3 = 800$ for case a), while $\tilde{\mu} = 0$ for case b). The solution in field space is shown on fig. 3.9, with the initial ansatz taken to be a straight line with $N = 15$ that connects the two minima. Remarkably, the PB solution converges to the correct value very quickly, with $\mathcal{O}(1)$ iterations, as seen from fig. 3.9.

It is clear from the insets of fig. 3.9 that the PB action is quite precise even with $N = 15$ and reaches roughly permille precision with $N = 100$. The main requirement for improving the precision of the action is to increase the number of segments to get an accurate description of the longitudinal ρ dependence. The shape of the path in field space is less important and does not change much when N increases. All of the results above are similar for $D = 3$.

Again, the convergence of the action can be improved by taking into account also the ρ dependence of the PB ansatz, similar to the single field extension defined above. It is also possible to solve the multifield bounce equation by solving for ζ dynamically and gluing the corresponding Bessel functions. This is a somewhat tedious task that requires local field rotations and is beyond the scope of the current work, but a similar semi-numerical approach was done in $D = 3$ by [85].

Finally, the path converges to the final one without oscillations, in contrast to [82], where the ρ dependence of transverse field directions was dropped, effectively neglecting the kinetic term. Since we use an explicit solution in (3.40), the dynamical term of the curved path is taken into account. This happens also in [85], where the field construction is slightly more involved, requiring local rotations and evaluation of Bessel functions.

3.6 Conclusions and outlook

An efficient and fast approach for calculating the false vacuum tunneling rate is developed for arbitrary potentials with any number of fields up to the desired precision. The method is based on the simple, well-known exact solution [122] that is extended to any number of segments, space-time dimensions and number of scalar fields.

Usually, the simple single field problem of finding the bounce is solved by shooting - numerically integrating the bounce equation and looking for the correct initial condition. Here instead, the differential equations are solved exactly and are glued into a single continuously differentiable field. The boundary conditions can be solved exactly and the field solution is computed recursively. The remaining initial/final conditions are highly non-linear but can be solved by iterative use of Derrick's theorem or numerical root finding.

In contrast to numerical integration, the PB solution is given by segmented polynomials. This allowed for simple analytical manipulation, such as including corrections of higher orders in the potential expansion, quantum or thermal fluctuations, expanding to more fields and it ultimately reduces the computational cost. Because the one field solution depends on a single dimensional parameter, which is the initial radius defined on some initial segment, the fine-tuning of initial conditions is avoided. This is advantageous especially in the thin wall regime, where the usual shooting procedure struggles.

The method was applied to the displaced quartic potential, where the resulting bounce action converges quickly with $N \gtrsim \mathcal{O}(10)$ and reaches a permille level precision as seen in fig. 3.4. The polygonal potential can serve as an ansatz to be perturbatively deformed in order to describe the remaining non-linearities. These are generically important close to the extrema and their inclusion improves the convergence of the bounce action, as seen from fig. 3.6, where the comparison with existing tools is made.

The ability of perturbative expansion allows for the generalization to the multifield case. The main challenge with respect to the single field case is finding the path in field space. The PB approach solves it by starting from an initial polygonal ansatz that is iteratively deformed by solving the bounce equations at the leading order. Path deformation is solved by a linear system and converges very quickly without oscillations such that the action is recovered to arbitrary precision within a

few iterations.

In summary, we find that the PB method is a robust, precise and reliable way of computing the semi-classical tunneling rate for any given potential. This approach describes the false vacuum decay in flat space time, however the solution can also be used in curved space-time within a small gravitational field approximation [133, 134]. The PB solution and its extension can thus provide a tool with an analytical insight in characterizing stable vacua of theories with multiples scalar fields [135, 136, 137, 138, 139, 140], describing bubble nucleation and the quality of potential first order phase transitions as well as the related spectrum of gravitational waves.

Chapter 4

`FindBounce`: A package for multifield bounce action

4.1 Introduction

In this section we present a `Mathematica` package, called `FindBounce` that implements the polygonal bounce method discussed in chapter §3 [141]. It is a publicly available and documented software that serves to compute the bounce action $\mathcal{S}_0$ for models with an arbitrary number of scalar fields in flat spacetime dimensions $D = 3$ and $D = 4$. This is done by the main function `FindBounce`, which computes the bounce action and returns the associated field solution. It is simple to use with a native `Mathematica` look and feel, it is easy to install, and comes with detailed documentation and physical examples, such as the calculation of the nucleation temperature.

The package preserves the semi-analytic structure of the method and stores the parameters of the field solution that can be used for further manipulation by a dedicated data structure called `BounceFunction`. This allows for a fast and robust evaluation of arbitrary potentials with specified precision, where the time cost grows linearly with the number of fields and/or the number of segments. Typical running time is roughly less than 1 (2) seconds for 10 (20) fields with 0.5% accuracy of the action. The package was tested on Mac OS X and Windows but it should work on any device where `Mathematica` 10 or above is installed.

The upcoming section starts with a quick tryout of the `FindBounce` package, where the minimal short guide to installation is presented with the most basic examples. A more detailed description of the inner workings of the package, with a description of the `FindBounce` function and available options is outlined in §4.3. Examples with benchmarks, performance, timing, and comparisons can be found in §4.4. We also provide timing benchmarks with comparisons to other existing tools, where applicable. We leave the concluding remarks and an outlook for future developments to §5.6.

4.2 Installation and running guide

4.2.1 Download and installation

The FindBounce package is released in the .paclet file format, which contains all the code, documentation and other necessary resources. The latest version of .paclet file can be downloaded from the repository "releases" page (https://github.com/vguada/FindBounce/releases) and can be installed by evaluating the following code in Mathematica.

```
In[1]:= PacletInstall["full/path/to/FindBounce-X.Y.Z.paclet"]
```

This will permanently install the FindBounce package to the $UserBasePacletsDirectory. To update the documentation, it may be necessary to restart Mathematica. Mathematica will always use the latest installed version. All the previously installed versions of FindBounce can be enumerated by evaluating PacletFind["FindBounce"]. More detailed information about the FindBounce package can be found with PacletInformation["FindBounce"]. All the versions can be uninstalled with PacletUninstall["FindBounce"].

4.2.2 Running

Once the package is installed, load it with Needs.

```
In[1]:= Needs["FindBounce`"]
```

To access the documentation, open the notebook interface help viewer and search for FindBounce. Let us show how FindBounce can be used on a simple example

```
In[2]:= V[x_]:= 0.5 x^2 + 0.5 x^3 + 0.12 x^4;

In[3]:= extrema = x/.Sort@Solve[D[V[x],x]==0];
```

The bounce is obtained with the FindBounce function

```
In[4]:= bf = FindBounce[V[x],x,{extrema[[1]],extrema[[3]]}]
```

where the order of the minima is arbitrary.

```
Out[4]= BounceFunction[  ]
```


Here, all the options have their default values and the results can be extracted as follows.

```
In[5]:= bf["Action"]

Out[5]= 73496.

In[6]:= bf["Dimension"]

Out[6]= 4
```

Notice that the summary box outputs rounded values, e.g. for the action, while directly accessing values from the BounceFunction object is done with default precision.

This concludes the simplest demonstration for single field use. More details regarding the other available options and their use are available in §4.3.1. Before moving on, let us briefly comment on FindBounce argument overloading. It is possible to study arbitrary purely polylinear potentials by providing a set of points and their potential values $\{\tilde{\varphi}, V(\tilde{\varphi})\}$:

```
FindBounce[{{x1,V1},{x2,V2},...}]
```

An example of such use is given in §4.4.3. Finally, the FindBounce function is overloaded for use with multi-field potentials, in which case the evaluation is done by the following syntax:

```
FindBounce[V[x,y,...],{x,y,...},{m1,m2}]
```

where $m_{1,2}$ are the two multi-field minima; see §4.4.5 for definite examples.

4.2.3 Contributing

Please use the issues (https://github.com/vguada/FindBounce/issues) page on the GitHub repository to submit bugs or feature ideas. Pull requests are welcome, however in case of major changes, please open an issue first to discuss what you would like to change. For developers, the instructions on how to run the tests, build the package .paclet file from the source code, and create the documentation, can be found in the CONTRIBUTING.md file.

4.3 Using the FindBounce and its output

4.3.1 FindBounce options

In this section we list and describe the available options of the FindBounce function. They are directly accessible within Mathematica using the FindBounce function documentation, which includes detailed descriptions and examples. The options and default values can be listed with the syntax

```
Options[FindBounce]
```

returning the options described below.

- "ActionTolerance" controls the relative variation of the bounce action $|\Delta\mathcal{S}|/\mathcal{S}$ between iterations of the initial radius R_{in} while solving the boundary conditions in (3.7). FindBounce also supervises the change of the action after each deformation of the path. The default tolerance value is 10^{-6}. See for example the right panel of fig. 4.2.

- "BottomlessPotential" is a Boolean variable used to specify whether the combination of polygonal and quartic should be used. This option can be used to deal with single field potentials unbounded from below, as discussed in §4.4.4. The default value is False.

- `"Dimension"` defines the number of space-time dimensions, given by the integer D. The default value is $D = 4$ for zero temperature tunneling via quantum fluctuations. In thermal field theory, the $D = 3$ action is needed, which is obtained by the following evaluation.

```
In[7]:= bf3 = FindBounce[V[x],x,{extrema[[1]],extrema[[3]]},
            "Dimension"-> 3];
```

- `"FieldPoints"` controls the segmentation in field space. It is specified either by the integer number of field values or by an explicit list of field values $\{\tilde{\varphi}_1, \ldots, \tilde{\varphi}_N\}$ given by the user.
  - `"FieldPoints"-> 31` by default. When specified by a single integer N, the segmentation is homogeneously split into N equidistant field points. For multiple scalar fields, the initial trajectory is taken to be a straight line connecting the two minima, e.g. the black dot-dashed line in fig. 4.6.
  - `"FieldPoints"-> {`$\tilde{\varphi}$`}`. Arbitrary segmentations can be given with an explicit set of field coordinates as an input. The order of the minima is not important, `FindBounce` recognizes the higher one as the false vacuum state. For single field potentials field points remain fixed, while for multifields they move when the path is being updated.

- `"Gradient"` controls the evaluation of the bounce beyond the poly-linear approximation of $V(\varphi)$, as in (3.24). There are four available option values.
  - `"Gradient"-> Automatic` by default. `FindBounce` computes the bounce by taking into account the 2^{nd} order approximation to $V(\varphi)$ in (3.24). The gradient function(s) of the potential needed in (3.41) are obtained analytically by running `Grad[V[x,y,...],{x,y,...}]`.
  - `"Gradient"-> "FiniteDifference"`. The set of gradient functions required in (3.41) are approximated by finite differences, where the small variations of the fields $\Delta\varphi$, are proportional to the total length of the path as $\Delta\varphi \equiv 10^{-4} L_{path}$. This option is suitable for non-analytic potentials, or when the default derivative, given by `Mathematica`, may be complicated and leads to delays in evaluation.
  - `"Gradient"-> {`$dV/d\varphi_i$`}`. The set of gradient functions can also be precomputed, stored and given as an input with this option. This can be used in multiple evaluations and scanning to save the computation time. See for example §4.4.5.
  - `"Gradient"-> None`. With this setting, the 2^{nd} order extension is turned off and the polygonal method is implemented in the poly-linear approximation. This may be necessary when the the derivative of the potential is discontinuous, as in §4.4.2.

- `"Hessian"` option for multi-field bounce calculations regulates the evaluation of the second derivatives $d^2V/d\varphi_i d\varphi_j$ in (3.41).
  - `"Hessian"-> Automatic` is the default behavior, where `Mathematica` computes the Hessian matrix analytically by running `Grad[Grad[V[x,y,...],{x,y,...}],{x,y,...}]`.

  - `"Hessian"-> "FiniteDifference"` approximates the Hessian matrix required in (3.41) with numerical finite differences. Similarly to the `"Gradient"` option, the variations of the fields are computed from the path length and given by $\Delta\varphi \equiv 10^{-4} L_{path}$.
  - `"Hessian"->` $\{d^2V/d\varphi_i d\varphi_j\}$. Similarly to the `"Gradient"` option above, the Hessian matrix of functions can be provided externally by the user to speed up the calculation.

- `"MaxPathIterations"` can be used to control the maximum number of times the path can be iterated after starting from the initial ansatz; the default value is 3. See for example §4.4.5.

- `"MaxRadiusIterations"` sets the maximum number of iterations to compute the initial radius R_{in} that satisfies Eq. (2.27); the default value is 100. Generically, `FindBounce` takes about $O(1)$ iterations to compute the action up to the default tolerance value. However, this option may be overridden by the `ActionTolerance` requirement, which prioritizes the precision of the action and thus allows for a larger number of iterations.

- `"MidFieldPoint"` allows the user to control the segmentation by setting a single arbitrary intermediate field point between the two minima, such as saddle points.

  - `"MidFieldPoint"-> None` by default: the segmentation is a homogeneously discretized straight line in field space connecting the two minima.
  - `"MidFieldPoint"-> Automatic`. The straight line connecting the two minima is divided by $\tilde{\varphi}_{max}$ into two homogeneous segmentations. The intermediate field point $\tilde{\varphi}_{max}$ is the local maximum of the V on the straight line, and is computed with `FindMaximum`. This option is suitable for nearly flat or very asymmetric potentials, where automatic segmentation may not detect the maximum unless a large value for `"FieldPoints"` is used.
  - `"MidFieldPoint"->` $\tilde{\varphi}_{int}$ The segmentation is divided by $\tilde{\varphi}_{int}$ into two homogeneous segmentations. It consists of two straight lines that connect the two minima with the intermediate field point $\tilde{\varphi}_{int}$.

  See §4.4.2 for single field and section §4.4.5 for a multi-field example.

- `"PathTolerance"`, controls the search with multiple scalar fields, where the path in field space changes with each iteration. Its value specifies the maximal allowed deviation of the path from one iteration to another. It is defined as the maximum length of deformation of any field point after each iteration, normalized to the total length of the path: $\max_s \left|\tilde{\zeta}_s\right| / L_{\text{path}}$ with default value 10^{-2}.

The `FindBounce` stops if either `"MaxPathIterations"`, `"PathTolerance"` or `"ActionTolerance"` is satisfied.

4.3.2 Bounce function output and manipulation

The results of the calculation are bundled in the `BounceFunction` container, which stores various parameters and other properties of the solution. The `BounceFunction` is rendered in `Mathematica` notebooks with a summary box that contains some minimal amount of information: the shape of the field solution, Euclidean action and the number of space-time dimensions. The list of all the available properties can be accessed with the following syntax:

```
In[8]:= bf["Properties"]

Out[8]= {Action, BottomlessPotential, Bounce, Coefficients,
         CoefficientsExtension, Dimension, Path, PathIterations,
         Radii}
```

- `"Action"` gives the value of the Euclidean bounce action.
- `"BottomlessPotential"` returns the constant factor of the quartic potential V_0 of Eq. (4.3). See §4.4.4 for an example.
- `"Bounce"` returns the piece-wise smooth function that characterizes the bounce solution $\varphi(\rho)$. It can be evaluated as a continuous function, see section §4.4.5 for an example.
- `"Coefficients"` provides the constant factors $\{v_{is}, a_{is}, b_{is}\}$ in Eqs. (3.36) and (3.40) that define the multi-field (polygonal) bounce solution in each segment. See §4.4.4 for an example.
- `"CoefficientsExtension"` provides the constant factors $\{\nu_{is}, \alpha_{is}, \beta_{is}, \partial^2\tilde{V}_s\}$ in eqs. (7.9) and (3.25) that define the extension of the multi-field (polygonal) bounce solution ξ and $\mathcal{I}$ in each segment.
- `"Dimension"` returns the number of space-time dimensions in which the bounce was computed, where finite (zero) temperature corresponds to $D = 3$ ($D = 4$).
- `"PathIterations"` reports the number of times the path in field space was deformed from the initial ansatz. An upper limit on this parameters is set by the `"MaxPathIterations"` option.
- `"Path"` gives a list of points $\tilde{\varphi}_s = \varphi(R_s)$ that defines the trajectory of the bounce in field space. This output can be used as an initial path ansatz to save time when finding the bounce solution for similar potentials, see section §4.4.5 for an example.
- `"Radii"` returns the list of radii R_s where the segments are joined from R_{in} to R_{N-1}.

In addition to the `BounceFunction` described above, a plotting function wrapper `BouncePlot` is available, such that the field configuration(s) can be plotted with ease. The `BouncePlot` behaves similarly to the native `Plot`, where the default options can be changed as shown in the example below. Multi-field bounce solutions, given as a list of functions, can also be plotted simultaneously.

```
In[9]:= BouncePlot[{bf3,bf},
          PlotLegends-> Placed[{"D=3","D=4"}, {Right,Center}]]
```

Out[9]=

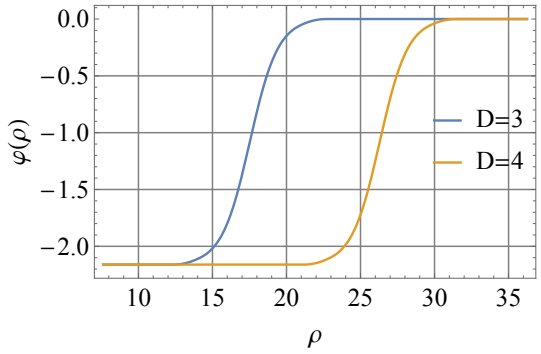

4.4 Examples

This section contains a number of examples, test cases and demonstrations of the `FindBounce` method. Each subsection contains a simple self contained code that can be easily reproduced in `Mathematica`. All of the examples given here (and more) are available also in the `Mathematica` documentation of `FindBounce` after installation.

We start with the single field benchmark in §4.4.1 that showcases the use of some available options and return values of `FindBounce` listed above in §4.3. One of the main aspects is the performance in terms of the precision of the action and timing in thick and thin wall regimes. In particular, timing scales linearly with the number of field points.

We consider the exactly solvable bi-quartic case in §4.4.2 that shows how `FindBounce` deals with such non-trivial cuspy potentials. In §4.4.3 we use the purely polygonal example with $N = 5$ points to reproduce the curious case of the disappearing instanton in the presence of additional local minima. We show how `FindBounce` can estimate the escape point φ_0 of unstable potentials in §4.4.4 by combining the exact linear solution to an exact (unstable) quartic one.

For multi-field applications, we first perform the simplest study with two fields in §4.4.5, where we demonstrate how to control the precision and speed of the evaluation as well as the use of an arbitrary path ansatz. We also demonstrate the use of `FindBounce` on effective and thermal potentials and give a demonstration on computing the nucleation temperature. In the final sub-section §4.4.7, we address the bounce calculation with an arbitrary number of fields and test the `FindBounce` method with up to twenty fields. We compare the results with other existing methods and demonstrate that the time demand of the `FindBounce` function scales *linearly* with the number of fields.

4.4.1 Single field benchmark

Let us consider a generic renormalizable scalar potential with terms up to the quartic power. Such potentials in general feature an unstable ground state, as seen on the left panel of fig. 4.1. Using the re-scaling properties of both the field φ and the ρ from (3.35), one can rewrite V as a function of a single parameter α, as [99]

$$V = \frac{1}{2}\varphi^2 + \frac{1}{2}\varphi^3 + \frac{\alpha}{8}\varphi^4. \tag{4.1}$$

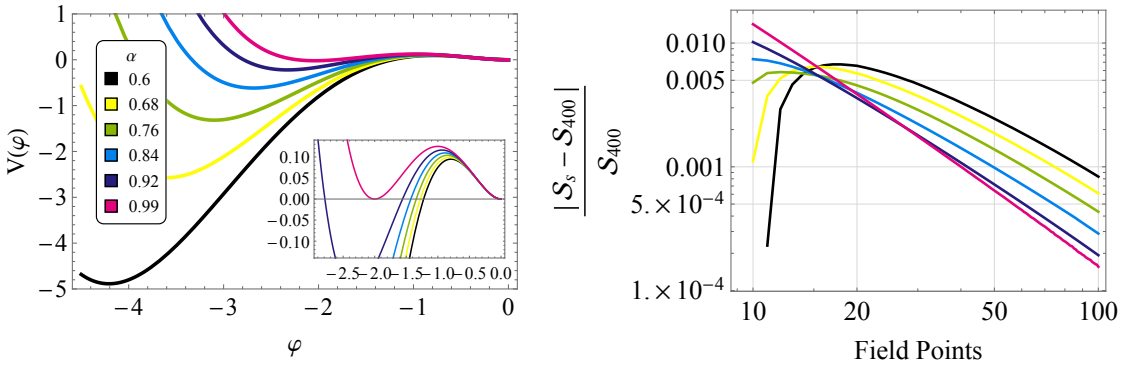

Figure 4.1: Left: The benchmark potential from Eq. (4.1) for different values of α going from thick $\alpha = 0.6$ to thin wall $\alpha = 0.99$. Right: The bounce action $\mathcal{S}_s$ for each potential configuration and a given number of field points s, normalized to $s = 400$ and computed in $D = 4$.

Here $0 \leq \alpha \leq 1$ covers all the possible scenarios going from thick to thin wall respectively. The bounce configuration for a particular α and the number of field points N in 3 space-time dimension can be obtained by `FindBounce` with:

```
In[1]:= V[x_,a_]:= 0.5 x^2 + 0.5 x^3 + 0.125 a x^4;

In[2]:= extrema[a_]:= x /. Sort@NSolve[(D[V[x,a], x]) == 0, x];

In[3]:= bf[a_,n_Integer]:= FindBounce[V[x,a], x, extrema[a][[{1,3}]],
          "FieldPoints"-> n, "Dimension"-> 3];

In[4]:= bf[0.6,100]

Out[4]= BounceFunction[  ]

In[5]:= bf[0.6,100][{"Action","Dimension"}]

Out[5]= {44.5098, 3}
```

The resulting action for different values of α is plotted on the right panel of fig. 4.1 and is normalized to $N = 400$ field points, which is already very precise. The accuracy of the action improves with the number of field points and goes below the percent level with $N = 30$ segmentation points in both, thin and thick wall. As expected, the convergence is faster for thin walls since the minimal $N = 3$ case already coincides with the thin wall solution. Note also that in this case, the 2^{nd} order correction of the potential is taken into account by default and the convergence is faster than the pure polygonal calculation.

The construction of the bounce solution, in particular the v_s, b_s parameters, already indicates that adding more segments does not require significant additional computing cost: evaluation time of the sums in (3.7) grows linearly. Thus it is to be expected that the total time should grow linearly with the number of field points, which is indeed the case, as displayed in fig. 4.2. Note that the `FindBounce`

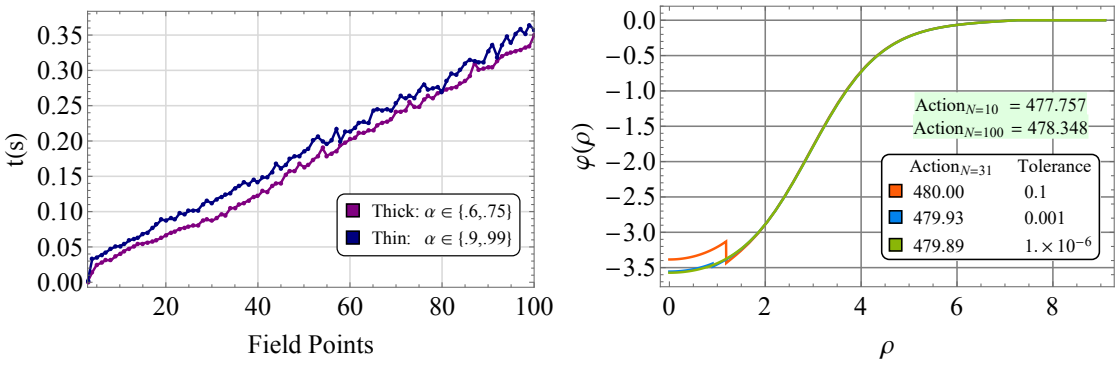

Figure 4.2: Left: Evaluation time with respect to the number of field points, averaged over two intervals of α corresponding to thin and thick wall regimes. Right: The bounce field configuration and action with $N = 31$ (default) field points for different tolerance value of the action controlled by `"ActionTolerance"`. Reference values of the action for `"FieldPoints"->` 10 and 100 field points with `"ActionTolerance"->` 10^{-6} (default) are shown on the green background.

performance is similar for both thick and thin walls, with a $\sim 10\%$ faster evaluation in the thin wall regime.

This behavior should be contrasted with numerical approaches based on under-over-shooting. There, the very thin wall limit requires an exponential amount of precision in finding φ_0[1]. This may cause numerical approaches to fail or significantly reduce the speed of computation. `FindBounce` instead relies on the R_{in}, which is found by extremizing the action, similar to the original thin wall approach [68]. Such change of variables thus provides a more stable universal behavior near the thin wall limit.

Speed and accuracy can be controlled as explained in §4.3.1. The bounce field configuration and the action can be computed with different requirements for `"ActionTolerance"`, as shown on the right panel of fig. 4.2. Even though the boundary conditions are not exactly satisfied at the first segment around $\rho \simeq 3$, the rest are joined analytically and the solution is smooth. Despite the discontinuity, the bounce action is fairly precise and within the limits of required action tolerance. For comparison, we also show the Euclidean action with different number of `"FieldPoints"-> 10, 100`, computed with the default `"ActionTolerance"->` 10^{-6}, which shows how the action converges with the number of field points.

As a final comment, one can use the `"FieldPoints"` option to specify a fixed custom segmentation from which the bounce is obtained. This feature may be useful when dealing with non-homogeneous potentials that contain flat pieces, followed by local features. In such cases, rather than increasing the number of field points, constructing a custom segmentation may be more beneficial. In the following subsection we give one such example, where a bi-homogeneous segmentation, set by the `"MidFieldPoint"` option gives a more stable output.

[1] As in [68], when φ_0 is very close to the true vacuum $\tilde{\varphi}_1$, the solution is given by $\varphi(\rho) - \tilde{\varphi}_1 = 2\,(\varphi_0 - \tilde{\varphi}_1)\, I_{D/2-2}(m\rho)/(m\rho)$, where $m^2 \equiv V''(\tilde{\varphi}_1)$. Thus in the thin wall limit $R_{in} \gg m^{-1}$ the initial condition $\varphi(R_{in}) \equiv \varphi_0$ is exponentially tuned.

4.4.2 Bi-quartic potential

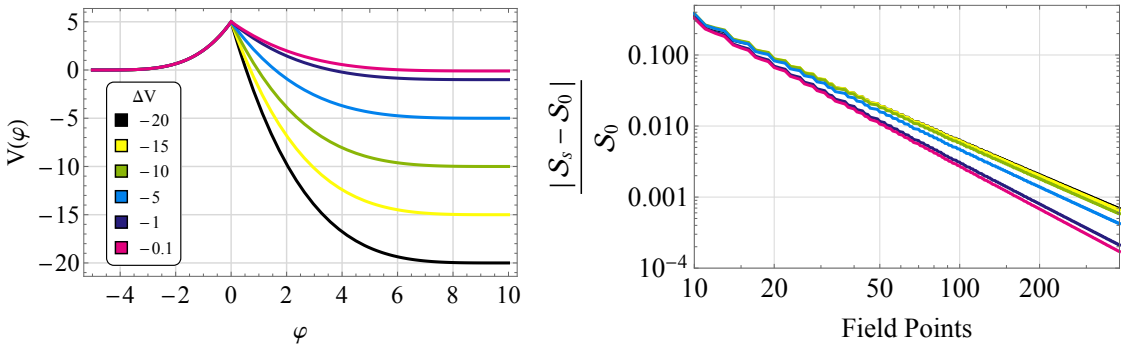

Figure 4.3: Left: The piecewise quartic potential for different values of the potential difference between the vacua, going from the thin wall $\Delta V = -0.1$ to thick wall $\Delta V = -20$ regime. Right: The bounce action $\mathcal{S}_s$ for different number of field points, normalized to the exact result $\mathcal{S}_0$ of the bi-quartic potential.

Perhaps the cleanest way of testing the `FindBounce` package is to compare it to one of the few non-trivial analytical closed-form solutions that are available [117, 122, 123, 133]. Here, we consider the bi-quartic potentials studied in section §2.5.2.

For the sake of illustration we choose a potential with fixed local extrema and leave a single parameter ΔV, which controls the potential difference between the false and true vacua. As shown on the left of fig. 4.3, we vary ΔV from -20 (thick wall) to $\Delta V = -0.1$ (thin wall). The corresponding action values are computed with different number of field points and are shown on the right panel. They are evaluated at $D = 4$ and normalized to the known exact value.

The `FindBounce` syntax used for this calculation is again simple.

```
In[1]:= DV = -20;
        V[x_]:= Piecewise[ {{0.008 (x + 5)^4, x < 0},
          {DV + (5 - DV)(x/10 - 1)^4, x >= 0}} ];

In[2]:= FindBounce[V[x], x, {-5, 10},
            "Gradient"-> None, "MidFieldPoint"-> 0]
```

Notice that the first derivative of the potential, required in Eq. (3.25), is not well defined at the origin $\varphi = 0$, therefore the default evaluation of the gradient, as well as the automatic extension of the polygonal approach, was turned off with `"Gradient"-> None`. If this were not the case, `FindBounce` would issue a warning message and automatically return the solution computed without the gradient extension. Due to the absence of the second order correction, the convergence is a bit slower compared to the previous example in §4.4.1. Nevertheless, `FindBounce` finds the solution within 1% accuracy for 50 (100) field points in thin (thick) wall regime.

The other option used above is the `"MidFieldPoint"`, which was used to set the intermediate field point of the segmentation to $\varphi = 0$, see the left panel of fig. 4.3. This feature is optional but stabilizes and improves the accuracy of the bounce action, especially with a small number of field points.

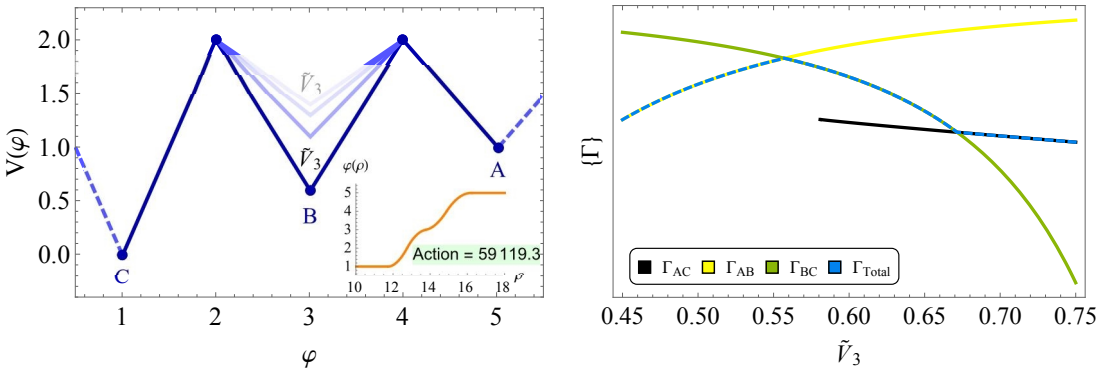

Figure 4.4: Left: The minimal example of a potential with an intermediate minimum. The inset shows the bounce solution with the typical double bubble wall shape in orange. Right: Decay rates for the direct (ABC) and the two subsequent (AB, BC) transitions, together with the total decay rate (4.2).

4.4.3 Intermediate minima and disappearing instantons

A number of physically motivated models may feature a non-trivial potential with many local minima. Such situations appear in multiple axion and relaxion-type potentials [142, 143, 144, 145, 146, 147, 148, 149, 150]. Here we demonstrate the use of the polygonal approach to analyze the minimal polygonal potential with an intermediate minimum, i.e. the two-triangle construction with $N = 5$ field points, shown on the left of fig. 4.4.

The value of the potential at the mid-point $\tilde{V}_3$ controls the depth of the intermediate minima and the resulting bounce solution. As this is lowered below the highest extremum $\tilde{V}_3 < \tilde{V}_5$, two types of transitions are possible. The direct tunneling from $\tilde{V}_5$ to $\tilde{V}_1$ (the ABC) instanton, or a two-step transition first from $\tilde{V}_5$ to $\tilde{V}_3$ (AB) and then from $\tilde{V}_3$ to $\tilde{V}_1$, the BC instanton. The right panel of fig. 4.4 shows the associated rates and the total decay rate, defined by

$$\Gamma_{total} \approx \frac{\Gamma_{AB}\Gamma_{BC}}{\Gamma_{AB} + \Gamma_{BC}} + \Gamma_{AC}. \tag{4.2}$$

The point of emphasis is that the direct ABC transition exists only up to a certain value of $\tilde{V}_3$ and then suddenly disappears. This behavior of a disappearing instanton was pointed out in [151] and explained in the thin wall approximation. In order to construct the bounce of the direct solution, the field should traverse from $\tilde{\varphi}_1$ to $\tilde{\varphi}_3$ with a radius associated to the BC transition and finally from $\tilde{\varphi}_3$ to $\tilde{\varphi}_5$ at the AB radius. Clearly, to have a meaningful solution $R_{BC} < R_{AB}$. However, when we lower the intermediate minimum, $\tilde{V}_3$ comes increasingly close to $\tilde{V}_1$, thus R_{AB} grows larger, and thereby Γ_{AB} decreases until direct tunneling via the ABC instanton becomes impossible. This is seen on the right panel of fig. 4.4, where the Γ_{ABC} in black suddenly disappears. Of course, the two-step decay still exists, i.e. Γ_{AB} and Γ_{BC} are in fact non-zero.[2]

To study such particularly simple settings, `FindBounce` allows the user to manually set individual values of the potential as a list of points in field space

[2]Strictly speaking, one should perform the two-step analysis more carefully, and allow the field to develop in real time after tunneling from $\tilde{V}_5$ in the vicinity of $\tilde{V}_3$. This would lead to oscillations with subsequent decay, see e.g. [126, 127, 128, 129, 130] and potential enhancement of the rate.

$\left\{\left\{\tilde{\varphi}_1, \tilde{V}_1\right\}, \ldots, \left\{\varphi_N, \tilde{V}_N\right\}\right\}$. For example, the direct ABC instanton of fig. 4.4 is obtained with the following syntax.

```
In[1]:= FindBounce[{{1,0},{2,2},{3,0.6},{4,2},{5,1}}]

Out[1]= BounceFunction[ 

]
```

Note also that the order of points in the list is arbitrary and can be given from left to right or vice versa.

4.4.4 Potentials unbounded from below

In this section, we demonstrate how FindBounce can be used to deal with unstable potentials. Many BSM theories contain portions of parameter space with unstable field directions, such that local ground states may tunnel into the unstable region. This seems to be the case for the Standard Model as well, with the estimated lifetime significantly longer than the age of the universe, see e.g. [7, 9, 10, 152, 153].

Note that the quartic-quadratic potentials do not admit the bounce solution at tree level due to scale invariance [154], however the bounce may exists after the inclusion of quantum corrections. In any case, one might expect the unstable direction to be dominated by the negative quartic term at large field values.

The escape point can be found either by the usual numerical shooting method or with the polygonal approach. However, due to the steepness of the unstable direction, polygonal segments might need to be extended to large values, which may require a large number of segments. In order to provide a good estimate for large φ_0, we demonstrate how the poly-linear potential with many segments can be joined with an exact unstable quartic solution. This functionality is implemented in FindBounce single field potentials in $D = 4$. It can be turned on with the "BottomlessPotential"-> True, option, together with the field values $\tilde{\varphi}_N$ and $\tilde{\varphi}_2$. The latter is the point where the PB is connected to the unstable quartic.

To understand how the estimate works, consider the quartic potential V_q and the associated solution

$$V_q(\varphi) = V_0 - a_q\left(\varphi - v_q\right)^4, \qquad \varphi_q(\rho) = v_q + \frac{b_q}{1 + \frac{1}{2}a_q b_q^2 \rho^2}, \tag{4.3}$$

where v_q and b_q are constants of integration and $a_q > 0$ is a dimensionless parameter of the potential. Assuming the unstable φ^4 term dominates for large field values, a_q is fixed by equating it to the φ^4 coefficient of the input potential $V(\varphi)$.

Similar to the pure polygonal construction explained in section §3.2, the quartic piece of the potential can be matched to the polygonal ones. In particular, the coefficients b_q, v_q are then determined by the boundary conditions $\varphi_q(R_2) = \varphi_{PB}(R_2) = \tilde{\varphi}_2$ and $\dot{\varphi}_q(R_2) = \dot{\varphi}_{PB}(R_2)$. What remains to be determined is the matching radius R_2, which can be found with FindRoot, similar to the polygonal case above. Finally, we fix V_0 by requiring the potential to be continuous.

We demonstrate the use of FindBounce in such unbounded transitions with the following example, where we specify the minimum at $\varphi = 0$ and the connecting point to the quartic at $\varphi = 5$.

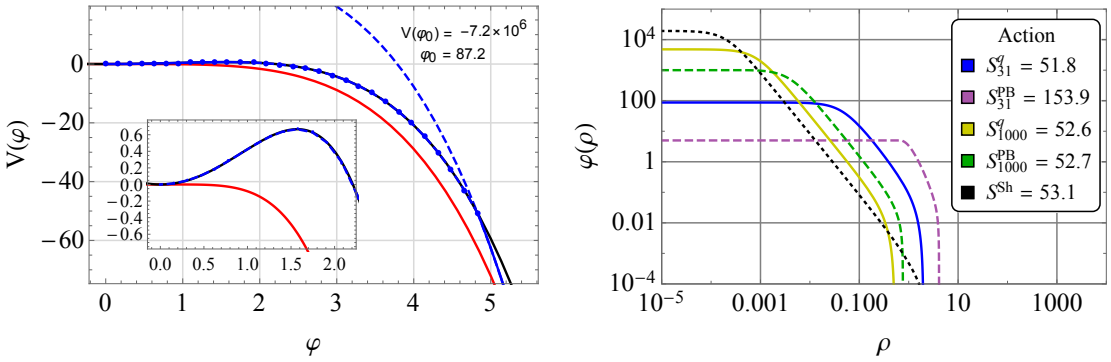

Figure 4.5: Left: Potential unbounded from below. The pure quartic, polygonal-quartic and input potentials are shown in red, solid blue and black, respectively. The dashed blue line is the pure quartic potential that is joined to the piece-wise polygonal potential. Right: The bounce field configuration with its bounce action. The solid lines show the field configuration with PB+quartic estimate, the dashed are the pure polygonal solutions and the dotted black line is the numerical result obtained with over-under-shooting.

```
In[1]:= V[x_]:= 0.5 x^2 + 0.05 x^3 - 0.125 x^4;

In[2]:= bf = FindBounce[V[x], x,{0, 5},"BottomlessPotential"->True];

In[3]:= {vq, aq, bq} = bf["Coefficients"];
        V0 = bf["BottomlessPotential"];

In[4]:= Plot[V0 - aq[[1]](x - vq[[1]])^4,
           {x, bf["Path"][[1,1]],bf["Path"][[2,1]]}]
```

The potentials of interest are shown on the right side of fig. 4.5 where the red, solid blue and black lines represent the pure quartic V_q, polygonal-quartic and the input potential, respectively. The dashed blue line is the pure quartic potential (4.3) that was joined to the polygonal potential. Its parameters are given by `"Coefficients"` and `BottomlessPotential` as shown in the syntax below. The bounce solution given by `FindBounce` is then shown on the right of fig. 4.5. Notice that the materialization of the bounce happens at $\varphi_0 \sim 90$, much above the connecting point at $\varphi = 5$.

4.4.5 Two field benchmark

Many extensions of the SM feature additional scalar fields, see [155] for a review. Extra scalars can couple to the SM Higgs and may alter the vacuum structure, potentially triggering a first order phase transition. The number of additional fields in generic SM extensions may be large. However, in many cases it may be sufficient to consider the dynamics of two fields only.

As a simple multi-field example in `FindBounce`, let us consider such two field potential with parameters chosen such that the field dynamics produces a large curvature in field space. We start with the simplest tree-level potential at zero temperature, compute the bounce action and show some additional features of `FindBounce`. In the upcoming §4.4.6 we show how to deal with finite temperature and thermal corrections.

Let us then consider the following example, where we call FindBounce on the two minima and ask it to connect them with an intermediate point, set by "MidFieldPoint". We also show how the pre-computed gradient function can be specified.

```
In[1]:= V[h_,s_]:=-100 h^2 + 0.1 h^4 - 60 s^2 + 0.3 s^4 + 3 h^2 s^2;
        minima = {{0.,10.},{22.4,0.}};

In[2]:= bf = FindBounce[V[h,s],{h,s}, minima,"MidFieldPoint"->{6,6},
          "Gradient"-> {-200h+0.4h^3+6h*s^2,-120s+1.2s^3+6s*h^2}];

In[3]:= {Ri,Rf} = bf["Radii"][[{1,-1}]];
        Show[
          ContourPlot[V[h,s], {h,-1,25}, {s,-1,11},Contours->50],
          ParametricPlot[ Through@bf["Bounce"][r], {r, Ri, Rf}]]

In[4]:= BouncePlot[bf,
          PlotLabel->Row[{"Action = ",Round@bf["Action"]}],
          PlotStyle->{Purple, Orange}]
```

The code above returns the bounce field configuration corresponding to the solid blue line in field space, shown on the left of fig. 4.6. The Euclidean time profiles $(h(\rho), s(\rho))$ can also be plotted easily and are shown on the right of fig. 4.6.

The dashed lines in fig. 4.6 represent the different choices of the initial path. By default, FindBounce chooses a straight line from one minimum to the other, seen by the black dashed line. In case there is a specific point that the segmentation should follow, such as the saddle point, or an arbitrary point in the above example, it is specified with the "MidFieldPoint" option. Finally, one can start with a completely arbitrary initial path, set by the "FieldPoints" option. In the example above, the dashed red line on the left of fig. 4.6 was obtained with a parabola connecting the two minima. The latter option is particularly useful when we already have some idea about the path in field space, e.g. when performing potential parameter scans.

Whatever the choice of the initial path is, FindBounce iterates the path deformation procedure until it reaches at least one of the following three conditions.

1. The maximum number of iterations, controlled by "MaxPathIterations". Here, zero means no perturbation of the initial path; i.e. all the dashed lines in fig. 4.6 were obtained by setting "MaxPathIterations"-> 0.

2. Path deformation measure, controlled set up by "PathTolerance", as explained in §4.3.1.

3. "ActionTolerance" that directly measures the change of the Euclidean action between iterations.

The resulting field configurations are shown in solid blue line on the left of fig. 4.6.

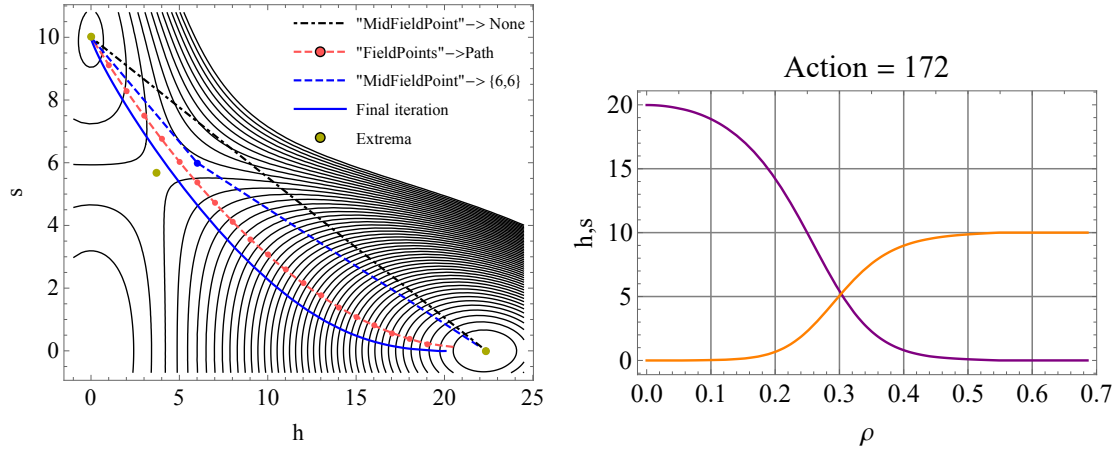

Figure 4.6: Left: Potential contours in solid gray lines, the final trajectory of the bounce field in solid blue line and three different initial paths in dashed. Black dot-dashed line is the default straight line ansatz, the straight dashed blue line includes the intermediate point at {6,6}, while the red dashed line is a parabola, set by hand. Right: The field configuration $(h(\rho), s(\rho))$ of the final iteration and the associated bounce action in the caption.

4.4.6 Thermal corrections and nucleation temperature

As a phenomenological application of `FindBounce`, let us compute the nucleation temperature of a SM extension with a real scalar singlet, i.e. the temperature where the phase transition takes place. This model can support a first order phase transition that could successfully explain phenomena such as: baryogenesis [137, 156, 157, 158, 159], dark matter [160, 161, 162, 163] and act as a possible source of gravitational waves [164, 165, 166, 167, 168].

We would like to consider the SM Higgs h together with the singlet scalar singlet field s. For simplicity, we assume an additional $\mathbb{Z}_2$ symmetry and define the tree-level renormalizable potential

$$V_{\text{tree}}(h,s) = -\frac{1}{2}\mu_h^2 h^2 + \frac{1}{2}\mu_s^2 s^2 + \frac{1}{4}\lambda_h h^4 + \frac{1}{4}\lambda_s s^4 + \frac{1}{4}\lambda\, s^2 h^2. \tag{4.4}$$

One-loop thermal corrections to the potential above can be computed using the equations presented in the appendix §B.1. For excellent references, see [169, 170], a review [171] or textbook [172]. The exact thermal one-loop functions $J_{B/F}$ in (B.3) were implemented efficiently in `C++` [173] and can be employed in `Mathematica` with the provided interface. However, we remain in the high-T limit and use the closed form given in Eqs. (B.4) and (B.5). These are valid up to $\mathcal{O}(T^4)$, while neglecting the contributions of the quartic coupling of the potential for simplicity.

As shown in [174], the thermal one-loop corrections to the potential in (4.4) at high-T are given by

$$V(h,s,T) = \frac{1}{2}\left(c_h h^2 + c_s s^2\right) T^2, \tag{4.5}$$

$$c_h = \frac{2M_W^2 + M_Z^2 + m_h^2 + 2m_t^2}{4v^2} + \frac{\lambda}{4!}, \qquad c_s = \frac{2\lambda + 3\lambda_s}{12}. \tag{4.6}$$

Here we considered the W, Z gauge bosons and the top quark contributions to the effective potential and neglected the other light fermions.

Following [88, 174], the tree level potential (4.4) can be redefined as a function of the critical temperature and couplings of the singlet fields $\{T_C, \lambda_s, \lambda\}$ respectively. Taking into account the constrains that lead to a first order phase transition and requiring that the deeper minimum becomes our Higgs vacuum as T is lowered, the effective quadratic couplings turn into:

$$\mu_h^2(T) = \lambda_h v_h^2(T), \qquad \mu_s^2(T) = -\lambda_s v_s^2(T), \qquad \lambda_h = \frac{m_h^2}{2v^2}. \tag{4.7}$$

The corresponding vacuum expectation values (vevs) are then

$$v_h^2(T) = v^2\left(1 - \frac{2c_h}{m_h^2}T^2\right), \quad v_s^2(T) = \frac{1}{\lambda_s}\left(\left(\frac{m_h}{2v}v_h^2(T)\sqrt{2\lambda_s} + c_s T_C^2\right) - c_s T^2\right), \tag{4.8}$$

where v is the SM vev at zero temperature and the minima of the potential are $\{v_h(T), 0\}$ and $\{0, v_s(T)\}$.

With the thermal and quantum corrections in place, we can show how the nucleation temperature T_N can be computed with `FindBounce`. The T_N is defined as the temperature when the probability for a single bubble to be nucleated within one horizon volume is ~ 1 [175]. Assuming radiation domination and the SM degrees of freedom in the thermal plasma, the above requirement roughly translates to $B = S_3/T_N \approx 140$.

Let us consider the benchmark in [88, 89] and use `FindBounce` to determine the variation of B with temperature.

```
In[1]:= V[h_, s_, T_] := -uh2[T]/2*h^2+us2[T]/2*s^2+lh/4 h^4+
          ls/4*s^4+l/4*s^2 h^2;
        ch = (2 mW^2 + mZ^2 + mh^2 + 2 mt^2)/(4v^2) + l/24;
        cs = (2 l + 3 ls)/12;
        uh2[T_] := mh^2/(2v^2) vh2[T];
        us2[T_] := -ls*vs2[T];
        vh2[T_] := v^2(1 - 2 ch/mh^2 T^2);
        vs2[T_] := ((mh/(2 v)*vh2[TC]*Sqrt[2 ls]+cs*TC^2)-cs*T^2)/ls;

In[2]:= {mW, mZ, mh, v, mt}={80.4, 91.2, 125.1, 246.2, 173.2};(*GeV*)
        {TC, l, ls, lh}={110(*GeV*), 1.5, 0.65, mh^2/(2 v^2)};

In[3]:= (*S3/T at finite temperature*)
        BT[T_?NumericQ,fp_] := 1/T*FindBounce[
          V[h, s, T], {h, s},{{Sqrt@vh2[T], 0},{0,Sqrt@vs2[T]}},
          "Dimension" -> 3, "FieldPoints"-> fp ]["Action"];

In[4]:= LogPlot[{BT[T,10],BT[T,31], 140}, {T, 70, 100},
           AxesLabel ->{"T(GeV)", "S3/T"},PerformanceGoal ->"Speed"]
```

Out[4]=

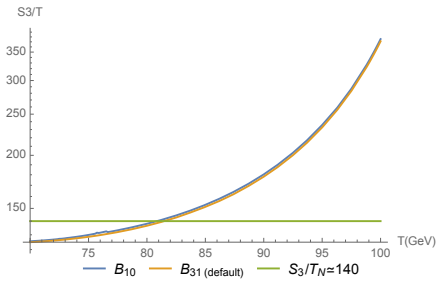

In[5]:=
```
Round[T /.FindRoot[BT[T,10] == 140,{T,100}]]
```

Out[5]=
```
81
```

The nucleation temperature we get is approximately 81 GeV, where $B_{10}(B_{31})$ is the normalized action, obtained with with 10(31) field points.

Clearly, one can improve the precision by increasing the number of field points `"FieldPoints"` and action tolerance with `"ActionTolerance"`. However, it should be kept in mind that one should also consistently consider quantum corrections, daisy resummation terms, the pre-factor A and contributions from lighter fermions, among others. Taking the above leading contributions only, `FindBounce` with only a few field points (10) already gives a reasonably accurate estimate, while being computationally inexpensive.

4.4.7 Beyond two fields

We devote this section to the estimates of the computational time of `FindBounce` with an arbitrary number of fields. We start with a simple example and show the `Mathematica` code to obtain the minima and compute the bounce configurations. Our main result is that the time requirement increases linearly with respect to the number of fields and that the calculation with 10 fields takes ~ 1 second. We compare the results to other available packages in the literature and test `FindBounce` with up to 20 fields.

From [88], we consider the multi-field potential as a function of the number of fields,

$$V(\varphi) = \left(\sum_{i=1}^{n_\varphi} c_i \left(\varphi_i - 1\right)^2 - c_{n_\varphi+1}\right) \sum_{i=1}^{n_\varphi} \varphi_i^2, \tag{4.9}$$

where c_i take values between 0 to 1. The position of the minima is a point in field space with components close to 0 and 1. Given the number of fields $n_\varphi = 6$ and a constant set of random parameters c_i, the code to compute the bounce is:

In[1]:=
```
nf = 6;
SeedRandom[1];
c = RandomReal[1, nf + 1];
phi = Table[Symbol["phi" <> ToString[i]], {i, nf}];
```

In[2]:=
```
V[phi_] := (Sum[c[[i]](phi[[i]]-1)^2,{i,nf}]-c[[-1]])
   Sum[phi[[i]]^2,{i,nf}];
```

```
In[3]:= extrema = Table[FindRoot[D[V[phi] == 0, {phi}],
          Transpose@{phi, ConstantArray[phi0, nf]}], {phi0,0,1}];

In[4]:= {minima, d2V}={phi/.extrema,D[V[phi],{phi},{phi}]/.extrema};
        ei=Table[DeleteDuplicates@Sign[Eigenvalues@d2V[[i]]],{i,2}];
        typeV=Table[If[Length@ei[[i]] > 1,
           "Saddle",If[ei[[i, 1]] > 0,"Minimum","Maximum"]],{i,2}]

Out[4]= {Minimum,Minimum}

In[5]:= bf = FindBounce[V[phi], phi, minima]

Out[5]= BounceFunction[ Action: 202.
                        Dimension: 4 ]

In[6]:= BouncePlot[ bf,
          PlotLegends->LineLegend[Automatic,LegendLabel->"Fields"]]
```

Out[6]=

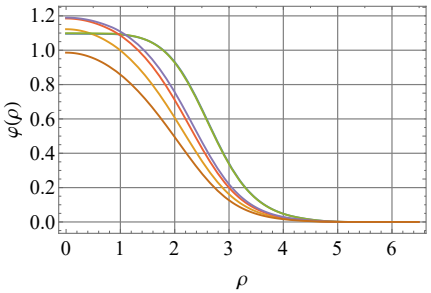

Since c_i were chosen at random, `FindRoot` might not find the minimum of the potential but a saddle point instead. In such case `FindBounce` returns `$Failed`. For more general potentials, the extrema can be computed with `Vevacious` [176], which is a tool that finds all the tree-level extrema of a generic one-loop effective potential.

With the multi-field potential defined in (4.9), we are ready to compute the action, estimate the computation time and compare to the existing tools. We vary the number of fields from the single field case going up to twenty fields. The results are collected in table 4.1 and on the left of fig. 4.7, together with results obtained by other methods. The parameters for $n_\varphi \leq 8$ were taken from [88], while for $n_\varphi > 8$ they were chosen randomly, as listed in the appendix §B.2. The comparison includes the `FindBounce` with 10, 30 and 100 field points, `CosmoTransition`(CT) [82], `AnyBubble`(AB) [86], `BubbleProfile`(BP) [88] and `SimpleBounce`(SB) [177].

We find that the action computed with $N \lesssim 20$ field points is accurate up to roughly 1%, as shown on the left panel of fig. 4.7. Similarly, bounces with `"FieldPoints"->` $10, 30$ in table 4.1 are accurate to 1% level or below. table 4.1 also shows how the accuracy of the action improves with the number of field points. In particular, the $N = 100$ case reproduces the values of the action obtained by other methods. Therefore, it is clear that one can use `FindBounce` with any type of potential to get the arbitrarily precise bounce action by adjusting the `"FieldPoints"` and `"ActionTolerance"` settings.

Note that the parameters c_i that regulate the multi-field potential for $n_\varphi \leq 8$ were chosen in a way that the bounce solution belongs to the thick wall regime. This is well suited for numerical shooting methods and typically gives the action of

Action							
n_φ	FB_{10}	FB_{30}	FB_{100}	CT	AB	BP	SB
1	52.1	52.6	52.4	52.6	52.4	54.1	52.4
2	20.8	20.8	20.8	21.1	20.8	20.8	20.8
3	20.8	20.7	20.7	22.0	22.0	22.0	22.0
4	57.9	56.2	55.8	55.9	56.4	55.9	55.8
5	16.3	16.3	16.3	16.3	16.3	16.3	16.4
6	24.6	24.5	24.5	24.5	24.5	24.4	24.5
7	36.9	36.7	36.7	36.7	36.6	36.7	36.7
8	46.4	46.1	46.0	46.1	46.0	46.0	46.0

Table 4.1: Comparison of the bounce action obtained by different methods in the literature for various number of fields n_φ. It includes `FindBounce` with 10, 30 and 100 field points and `CosmoTransition`, `AnyBubble`, `BubbleProfile` and `SimpleBounce`.

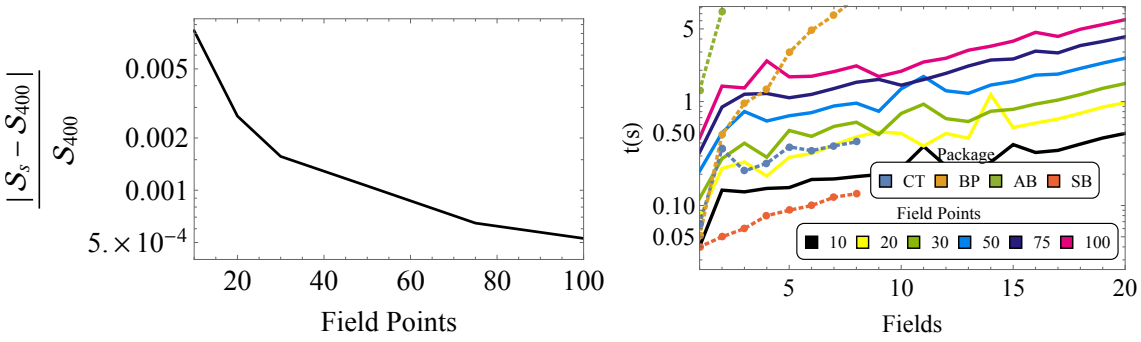

Figure 4.7: Left: The multi-field bounce action $\mathcal{S}_s$ average, normalized to the one with $N = 400$ field points. Right: Multi-field time measure with respect to number of fields for several field points. The solid lines were obtained by `FindBounce` with `"ActionTolerance"` $\to 10^{-4}$. The dashed lines with dots are the time measurements from other existing tools, see text for details.

$\mathcal{O}(10)$, as seen in table 4.1. For larger number of fields $n_\varphi > 8$, the parameters were chosen at random, see table B.1 and the resulting action in table B.2 contains both small and large values, in particular $n_\varphi = 15, 19$ that belong to the thin wall regime. Clearly, `FindBounce` can deal with both cases quite efficiently.

Let us turn to the timing performance of `FindBounce`. As explained in the PB method chapter §3, we expect this increase to be linear. Indeed, as shown on the right panel of fig. 4.7 in solid lines, the time consumption of `FindBounce` scales linearly with the number of fields n_φ. This behavior is independent of the number of field points, i.e. for different colors of the solid lines in fig. 4.7 and covers both thin and thick wall cases. Moreover, the time demand of `FindBounce` with respect to the number of field points also scales linearly in the multi-field scenarios.

The running time clearly depends on the CPU capabilities and the optimization efficiency of the implementation in a given computer language. In our setup, the

computation time of FindBounce for 10(20) fields turns out to be less than 1(2) seconds for the default value with 31 field points. This was computed on a desktop system using the Mathematica native functions AboluteTiming and RepeatedTiming running on a desktop iMac 10.12.6, equipped with an Intel Core i7, processor speed 3.4 GHz and 16 GB of DDR3 RAM clocked at 1.6 GHz.

For the other implementations, the timing reports were adopted from [88] and [177]. We find FindBounce to be comparable to these tools in terms of speed performance, as shown on the right side of fig. 4.7. In particular, the time demand with $N = 10$ field points is comparable to the values quoted by SimpleBounce and CosmoTransition. It should be noted though that the above tools are implemented in C++ and Python, while FindBounce was coded straightforwardly in Mathematica, with no significant numerical optimization.

4.5 Conclusions and outlook

The FindBounce package presented in this work performs the task of calculating the semi-classical contribution to the false vacuum decay rate, the so-called bounce field configuration and the associated Euclidean action. We demonstrated the basic use of the FindBounce function implemented in Mathematica, as well as the extended options and manipulation of the output. The current version of the package can deal efficiently with single and multi-field calculations, ranging up to 20 fields in a matter of seconds.

There are a number of physically relevant directions one can pursue, that may be implemented in the future versions of the FindBounce framework. An obvious question relates to the growth of the bubble after nucleation, which is governed by the bounce equations in Minkowski space-time [68]. An initial step in this direction was done in [121] and may be generalized straightforwardly to more segments and fields. Moreover, matching such solutions to subsequent tunneling may be needed when potentials with multiple minima are considered.

The semi-analytical approach to computing the bounce field configuration and the action at finite temperature is relevant for characterizing the strength of the potential phase transitions. In particular, we saw how one can determine the nucleation temperature T_N, that happens below the critical temperature, using the output from the FindBounce result. Similarly, one can get an analytical insight in the gravitational wave spectra by computing the α and β parameters [63], which are related to the strength and the position of the maximum in the frequency range. We intend to return to these issues in future instalments of the FindBounce approach.

Chapter 5

The decay rate at one loop: An exact solution

5.1 Introduction

Up to now, we have focused our attention on the leading semi-classical approximation that dominates the decay rate of a false vacuum. To get the complete physical picture and proper dimensions of the decay rate one must also get the pre-factor A of the exponent in (2.1), as discussed in chapter §1. Its computation and the renormalization of its ultraviolet divergences are well understood [69, 92, 93], but are in general difficult to obtain as it is related to functional determinants. They are related to the operator that describes quantum fluctuations around a non-trivial background, the bounce.

Since A does not have a dramatic exponential dependence unlike the bounce action $e^{-\mathcal{S}_0}$, it is often estimated on dimensional grounds. However, we should be concerned about how this may affect our results and be able to obtain it rigorously. In general, precise and consistent calculations of the pre-factor are needed in several contexts of physics, from the SM [9, 10] to the nucleation temperature in the early universe [94], i.e. when loop corrections are required. The prefactor was computed numerically at zero [98, 99, 178] and finite temperatures [97, 103], where recent progress was made in numerical calculations for gauge theories [179]. An analytic estimate in the TW limit was found in [102] (see also [97, 103, 104, 180, 181]), while the issues with gauge and scale invariance of the unstable quartic in the SM were worked out recently [6, 9, 182, 183] and the Fubini-Lipatov was studied in [105].

In this chapter we briefly describe the general well-known formalism that deals with those quantum fluctuations around the bounce and provide a method that computes A for any continuous and smooth potential that admits a bounce solution. Then we present our contribution [184], which consists of extending and re-deriving the above procedure to include potentials that might have a discontinuous first derivative. As a result, we provide a new exact false vacuum decay rate at one loop for a real and complex scalar field in $D = 4$, which is scarce in the literature. To my knowledge, we will present the first complete exact solution of the sub-leading quantum fluctuations for a potential with two separate tree-level minima. In particular, we find a simple formula for the prefactor of the bi-quartic potential described in §2.5.2, which depends only on the ratios of vevs and quartic couplings between the false and true vacuum.

This setup can be considered as a benchmark for understanding the impact of finite one loop corrections and serve for models that feature a large separation of scales. In particular, one can easily derive the behavior in the thin and thick wall limit and thus provide generic expectations for the class of potentials which are approximately scale-invariant around the two minima.

The order of the upcoming sections is the following. We start with the well-known formalism of the prefactor in chapter §5.2 and show how it can be evaluated for any given smooth potential [100, 101]. Then we focus on the bi-quartic potential, where we derive the exact expressions for the product of eigenvalues, removal of zeroes, and the finite sum in section §5.3. In section §5.4.1, we re-derive and extend the method presented in §5.2 to take into account potentials whose second derivative is discontinuous. There, we explain the use of the zeta function formalism via the contour integral to get both, the finite and the renormalized prefactor. The final exact result is summarized in §5.5, from where we derive simple expansions in the thin and thick wall limits and determine their validity. The outlook for further developments is discussed in §5.6 and technical details are left to the appendices §C.3 and §C.4. Appendix §C.1 contains a simple example to illustrate the powerful Gel'fand Yanglom formalism, which computes the function determinants without having to calculate the eigenvalues. Then, in appendix §C.2 I describe how the previous PB method can be used to obtain the pre-factor semi-analytically for any renormalizable potential.

5.2 Loop corrections

Before solving the bi-quartic potential, let us briefly present the complete expression of the prefactor and show how to compute it.

5.2.1 The prefactor

The pre-factor corresponds to the sub-leading contributions of the decay rate, related to one-loop field theory calculations. It was first derived in [69] (see also [185]) and explained in more detail in Coleman's lectures [30, 186] and classic textbooks [92, 93]. They start with the assumption that amplitude of transition of the FV state is proportional to the Feynman's path integral in Euclidean space-time,

$$\langle \varphi_{FV} \big| e^{-TH/\hbar} \big| \varphi_{FV} \rangle \sim \int \mathcal{D}\varphi \, e^{-\mathcal{S}[\varphi]/\hbar} \tag{5.1}$$

where H is the full Hamiltonian and T is the amount of Euclidean time taken by the transition. In chapter §2 we considered heuristic arguments from quantum mechanics to justify this assumption. However, a more rigorous derivation via path integration in Minkowski space has been provided recently in [72, 75], where they carefully extract the imaginary contribution that leads to the same decay rate. Here we accept this fact and continue with the evaluation of the path integral as it turns out proportional to the decay rate.

The integral above can be approximated by the saddle point method in the limit when $\hbar$ is small. For this purpose, the Euclidean action $\mathcal{S}[\varphi]$ is functionally expanded

around the bounce $\varphi = \overline{\varphi} + \psi$ up to second order,

$$\mathcal{S}[\varphi] \simeq \mathcal{S}[\overline{\varphi}] + \frac{\delta \mathcal{S}}{\delta \varphi}[\overline{\varphi}]\psi + \frac{1}{2}\psi \frac{\delta^2 \mathcal{S}}{\delta \varphi^2}[\overline{\varphi}]\psi + \dots, \qquad \mathcal{O} \equiv \frac{\delta^2 \mathcal{S}}{\delta \varphi^2}[\overline{\varphi}]\,, \tag{5.2}$$

where the first term corresponds to the bounce action $\mathcal{S}_0 = \mathcal{S}[\overline{\varphi}]$. The first derivative is zero because the bounce field configuration extremizes the action, i.e. $\delta\mathcal{S}/\delta\varphi[\overline{\varphi}] = 0$. The second derivative of the action, evaluated on the bounce, is defined as the fluctuation operator $\mathcal{O}$.

Expanding ψ in a set of eigenfunctions $\psi_{\mathbf{n}}$ of the fluctuation operator $\mathcal{O}\psi_{\mathbf{n}} = \gamma_{\mathbf{n}}\psi_{\mathbf{n}}$, we can perform the Gaussian integral in (5.7) and end up with the ratio of functional determinants [69]. That is, with a convenient normalization of the fluctuations, such that

$$\langle \psi_{\mathbf{n}} | \psi_{\mathbf{m}} \rangle = \int \mathrm{d}^4x\, \psi_{\mathbf{n}}\psi_{\mathbf{m}} = 2\pi\delta_{\mathbf{nm}}\,, \tag{5.3}$$

we find

$$\int \mathcal{D}\psi\, e^{-\mathcal{S}_0 - \frac{1}{2}\psi\mathcal{O}\psi} = e^{-\mathcal{S}_0}\prod_{\mathbf{n}}\int_{-\infty}^{\infty}\mathrm{d}c_{\mathbf{n}}\, e^{-\frac{1}{2}\gamma_{\mathbf{n}}\, c_{\mathbf{n}}^2 2\pi} = e^{-\mathcal{S}_0}\prod_{\mathbf{n}}\sqrt{\frac{1}{\gamma_{\mathbf{n}}}}\,, \tag{5.4}$$

where we have defined the path integral measure as $\mathcal{D}\psi = \prod_{\mathbf{n}}\mathrm{d}c_{\mathbf{n}}$. Thus the prefactor is proportional to an infinite product of eigenvalues $A \sim \prod_{\mathbf{n}}\gamma_{\mathbf{n}}^{-1/2}$ of the fluctuation operator $\delta^2\mathcal{S}[\bar{\varphi}]/\delta\varphi^2$.

In section §2.4, we proved that $\delta^2\mathcal{S}[\bar{\varphi}]/\delta\varphi^2 < 0$ in (2.30), which implies that the resulting spectrum contains at least an odd number of negatives modes. In fact, there is at most a single negative eigenvalue as demonstrated in [187], describes the unstable direction of the expanding bubble. Any symmetry of the bounce, such as translational, scale or internal global invariance, will be reflected in the number of zero eigenvalues [188, 189]. For instance, the translation modes are proportional to $\partial_\mu\bar{\varphi}$, which implies

$$\mathcal{O}\bar{\psi} \sim \mathcal{S}''[\bar{\varphi}]\partial_\mu\bar{\varphi} = \partial_\mu\left(\mathcal{S}'[\bar{\varphi}]\right) = 0, \tag{5.5}$$

confirming that $\partial_\mu\bar{\varphi}$ are the four zero modes. This means that $\mathcal{S}_0$ has no explicit position dependence, which justifies the space-time volume factor $\mathscr{V}$ on the left hand side of (5.7), as also commented in section 2.2. The normalization of these modes are obtained by comparing eq. (5.3) with:

$$\langle \partial_\mu\bar{\varphi} | \partial_\nu\bar{\varphi}\rangle = \frac{1}{2}\delta_{\mu\nu}\int \mathrm{d}^4x\,\frac{1}{2}\left(\partial_\sigma\bar{\varphi}\right)\left(\partial_\sigma\bar{\varphi}\right) = \delta_{\mu\nu}\mathcal{S}_0\,, \tag{5.6}$$

where we have used the identity (2.29) in the last step to get the action. The rescaled zero modes are then $\sqrt{2\pi/\mathcal{S}_0}\,\partial_\mu\bar{\varphi}$.

To obtain the final expression, we must remove the translational modes by integrating over the collective coordinates [9, 190, 191, 192, 193], which provide a factor of $\sqrt{\mathcal{S}_0/2\pi}$ for each space-time dimension. We end up with the decay rate at one loop written in the form

$$\frac{\Gamma}{\mathscr{V}} = \frac{\mathrm{Im}\int\mathcal{D}\varphi\, e^{-\mathcal{S}[\overline{\varphi}]}}{\int\mathcal{D}\varphi\, e^{-\mathcal{S}[\varphi_{\mathrm{FV}}]}} = \left(\frac{\mathcal{S}_0}{2\pi}\right)^2 \mathrm{Im}\sqrt{\frac{\det\mathcal{O}_{\mathrm{FV}}}{\det'\mathcal{O}}}\, e^{-\mathcal{S}_0}\left(1 + \mathcal{O}\left(\hbar\right)\right). \tag{5.7}$$

The prime in det' indicates that zero eigenmodes were removed, where each gives a dimension of mass squared that together gives the correct dimension of the decay rate. The numerator is the FV normalization, while the denominator is the integral around the bounce field configuration, with an imaginary component from the square root of the negative mode.

5.2.2 Evaluation of the prefactor

To compute the prefactor, we would like to find the product of eigenvalues $\gamma_{\mathbf{n}}$, associated with the operator $\mathcal{O}$ as

$$\mathcal{O} = -\Box + V''(\overline{\varphi}), \qquad \mathcal{O}\psi_{\mathbf{n}} = \gamma_{\mathbf{n}}\psi_{\mathbf{n}}, \tag{5.8}$$

where $\Box$ is the Laplace operator in flat 4D Euclidean space-time, and $V''(\rho)$ is the second derivative of the potential evaluated at the bounce. Here, $\mathbf{n}$ is a collective index for the relevant quantum numbers that come about when the boundary conditions $\psi_{\mathbf{n}}(0) = \psi_{\mathbf{n}}(\infty) = 0$ are imposed.

As the $V''(\overline{\varphi}(\rho))$ is 4D symmetric, we can separate the radial and orbital part of $\psi_{\mathbf{n}}$, where the latter is described by hyper-spherical harmonics. These are eigenfunctions of the total orbital momentum operator with orbital quantum numbers $l = 0, \ldots, \infty$, which are $(l+1)^2$-fold degenerate [110].

It turns out that it is simpler to rely on the Gel'fand-Yaglom [194] theorem, which relates the ratio of determinants to the value of the ratio of eigenfunctions evaluated at $\rho \to \infty$. That is, we have to find the zero eigenmodes of the fluctuation operator

$$\mathcal{O}_l\psi_l = -\ddot{\psi}_l - \frac{3}{\rho}\dot{\psi}_l + \frac{l(l+2)}{\rho^2}\psi_l + V''(\overline{\varphi})\,\psi_l = 0, \tag{5.9}$$

which provide the log of the ratio of determinants

$$\ln\left(\frac{\det\mathcal{O}}{\det\mathcal{O}^{\mathrm{FV}}}\right) = \sum_{l=0}^{\infty}(l+1)^2 \ln\mathcal{R}_l(\infty), \qquad \mathcal{R}_l \equiv \frac{\psi_l}{\psi_l^{\mathrm{FV}}}. \tag{5.10}$$

The boundary conditions (above for ψ) can be recast as $\mathcal{R}_l(0) = 1$ and $\mathcal{R}_l'(0) = 0$. To understand this concept more clearly, I have devoted appendix §C.1 to provide a simple example of the use of this theorem via a potential well in $D = 1$ space-time dimension.

The differential equation (5.9) is simple and can be easily integrated numerically for any angular mode l. However, we clearly cannot compute all of them numerically as they extend to infinity and we need them all to perform the renormalization of the ultraviolet divergences. A feasible approach to solve this issue has been provided by [99, 100], providing a simple semi-analytic method to compute the prefactor of any differentiable potential.

Before extending their approach into more general potentials, let us first summarize their results. The idea is that the calculation of the pre-factor splits into two parts: the low l region up to an arbitrary $l \leq L \simeq \mathcal{O}(10)$ and the high l region, going to infinity.

In the low l part the ratio of determinants $\mathcal{R}_l$ is computed by solving the differential equation for $\mathcal{R}_l$, eq. (5.9). The contribution to the decay rate is finite and proportional to the sum of the log of all the ratios of determinants:

$$\ln \Sigma_{\rm lo} = -\frac{1}{2}\sum_{l=0}^{L} (l+1)^2 \ln |\mathcal{R}_l(\infty)| \,. \tag{5.11}$$

On the other hand, when $l > L \gg 1$, one can solve for the $\mathcal{R}_l$ in a closed-form via the WKB approximation [99, 100, 178], which is regularized with the proper counter-terms. This high-l part of the rate is

$$\begin{aligned} \ln \Sigma_{\rm hi} =& \frac{(L+1)(L+2)}{8}\int_0^\infty \mathrm{d}\rho\, \rho \bar{V}'' - \frac{\ln L}{16}\int_0^\infty \mathrm{d}\rho\, \rho^3 \left(\bar{V}''^2 - V_{FV}''^2\right) \\ &+ \frac{1}{16}\int_0^\infty \mathrm{d}\rho\, \rho^3 \left(\bar{V}''^2 - V_{FV}''^2\right)\left(1 + \ln\frac{\rho}{2}\right), \end{aligned} \tag{5.12}$$

where $\bar{V}'' = V'' - V_{FV}''$. These integrals are straightforward to compute semi-analytically and the total prefactor contribution is the sum of the low and high l pieces.

In general, $\mathcal{R}_l$ cannot be computed in a closed-form, but only for particular $\bar{V}''$. In appendix §C.2, we provide an explicit example, where we exploit the semi-analytic properties of our PB method to compute the prefactor in a fast and efficient way for any single field potential that admits bounce solution.

In the next chapters, we present a simple model that provides a closed-form of $\mathcal{R}_l$, the bi-quartic potential, described in §2.5.2. In order to complete the prefactor calculation of this model, we must extend eq. (5.12) to include sharp potentials as the bi-quartic potential, where $V'' \supset \delta(\varphi)$. This is realized in chapter §5.4.2 in a self-contained way, whose results will converge to the equation (5.12) in the limit when the potential is smooth.

5.3 Functional determinants

In this section, we compute the functional determinant of the bi-quartic potential, which surprisingly admits a complete closed-form solution.

5.3.1 Radial mode separation and exact product of eigenvalues

The fluctuation potential follows from (2.40)

$$V''(\varphi) = 3\left(\lambda_1 (\varphi + v_1)^2 H(-\varphi) + \lambda_2 (\varphi - v_2)^2 H(\varphi)\right) - \left(\lambda_1 v_1^3 + \lambda_2 v_2^3\right)\delta(\varphi)\,, \tag{5.13}$$

and contains a delta function due to the discontinuity of V' at the origin. Let us see how the fluctuations behave. In the FV, we have $V_{\rm FV}'' = 0$ and the solution of (5.9) is $\psi_l^{\rm FV} = \rho^l$. We dropped the part that diverges at $\rho = 0$ and assigned the arbitrary multiplication constant to 1. The general solution of (5.9), when the fluctuation

potential is evaluated around the bounce, is instead given by

$$\begin{aligned}\psi_{ls} = A_{ls}\,\frac{\rho^l\,R_s^4}{\left(R_s^2-\rho^2\right)^2}\left(1-2\left(\frac{l-1}{l+2}\right)\frac{\rho^2}{R_s^2}+\frac{l(l-1)}{(l+2)(l+3)}\frac{\rho^4}{R_s^4}\right)\\ + B_{ls}\,\frac{R_s^{l+4}}{(R_s^2-\rho^2)^2}\frac{R_s^{l+2}}{\rho^{l+2}}\left(1-2\left(\frac{l+3}{l}\right)\frac{\rho^2}{R_s^2}+\frac{(l+2)(l+3)}{l(l-1)}\frac{\rho^4}{R_s^4}\right).\end{aligned} \tag{5.14}$$

where $s=1,2$ denotes the two segments of the bi-quartic potential.

On the first segment with $s=1$, regularity of ψ_{ls} at $\rho=0$ requires $B_{l1}=0$, and we choose the normalization $A_{l1}=1$, such that we normalize to the FV at $\rho=0$. This part reduces to the unstable single potential in the SM [6, 9], where we can easily read off the ratio $\mathcal{R}_l(\infty)=\lim_{\rho\to\infty}\psi_{l1}/\rho^l$ from the only term remaining in (5.14) at high ρ

$$\lambda\varphi^4: \quad \mathcal{R}_l(\infty)=\frac{\psi_{l1}\left(\infty\right)}{\psi_l^{\rm FV}\left(\infty\right)}=\frac{l(l-1)}{(l+2)(l+3)}\,. \tag{5.15}$$

On general grounds [187], we expect the $l=0$ mode to be negative, corresponding to the expanding bubble. On the other hand, the four $l=1$ eigenvalues should vanish because of the translational invariance of the center of the bubble (or the bounce solution, which depends only on ρ). The $\mathcal{R}_l(\infty)$ in (5.15) indeed contains a zero mode at $l=1$, but also has an additional zero at $l=0$, due to the classical scale invariance [6, 9].

Let us move on to the second segment and glue the two solutions. Since the fluctuation potential contains a delta, the first derivative of ψ_l changes discontinuously[1]. Therefore, the appropriate boundary conditions to join $\psi_{l1,l2}$ at $\rho=R_T$ are given by

$$\psi_{l1}=\psi_{l2}\,,\qquad \dot\psi_{l1}=\dot\psi_{l2}+\mu_V\psi_{l1}\,,\qquad \mu_V=\frac{\lambda_1 v_1^3+\lambda_2 v_2^3}{\dot{\overline{\varphi}}(R_T)}\,. \tag{5.16}$$

These fix the remaining parameters A_{2l},B_{2l} that ultimately determine the behavior of $\mathcal{R}_l$ as $\rho\to\infty$. We arrived to our main result for the fluctuation determinant

$$\mathcal{R}_l(\infty)=A_{l2}\frac{l(l-1)}{(l+2)(l+3)}=\frac{(l-1)(l^3+c_2l^2+c_1l+c_0)}{(l+1)(l+2)^2(l+3)}\,, \tag{5.17}$$

with the three coefficients c_i that depend only on dimensionless ratios x and y:

$$c_0=\frac{12(1+x)^2x^4y(1+x^3y)^2}{(x^4y-1)^3}\,, \tag{5.18}$$

$$c_1=\frac{2x\left(1+(1+2x)\,x^2y\right)\left(2+3x+(3+4x)x^3y\right)}{(x^4y-1)^2}\,, \tag{5.19}$$

$$c_2=\frac{1+4x+(4+7x)x^3y}{x^4y-1}\,. \tag{5.20}$$

All c_i are real and positive because $x^4y>1$, which follows from the construction of the potential. Similarly to the radii $R_{1,2,T}$, the c_i diverge in the TW limit.

[1]Integrating (5.9) around R_T, we have $\int_{R_T-\epsilon}^{R_T+\epsilon}\mathrm{d}\rho\mathcal{O}_l\psi_l=0\xrightarrow{\epsilon\to0}\dot\psi_l(R_T+\epsilon)-\dot\psi_l(R_T-\epsilon)=-\left(\lambda_1v_1^3+\lambda_2v_2^3\right)\int_{R_T-\epsilon}^{R_T+\epsilon}\mathrm{d}\rho\delta\left(\bar\varphi\left(\rho\right)\right)\psi_l$.

The zero eigenvalue of the scale invariant single quartic in (5.15) at $l = 0$ is now gone, it got absorbed by the $A_{l2} \propto l$ in (5.17). This happens because the bi-quartic contains mass scales $v_{1,2}$ that break scale invariance and the $l = 0$ mode in (5.17) becomes negative

$$\mathcal{R}_0(\infty) = -\frac{c_0}{12} < 0\,, \tag{5.21}$$

as required from the instability of the bounce solution.

It follows from (5.17) that $\mathcal{R}_l(\infty) \xrightarrow{l\gg 1} 1$ and the sum over l in (5.10) diverges quadratically in the UV – after all, we are computing a one loop quantity with a tree level counterterm. In §5.4.2 we will regularize the sum by subtracting the terms divergent in l and calculate the finite part. Before that, let us deal with the removal of the translational zero eigenvalues of the $l = 1$ modes.

5.3.2 Removing the zero modes

As discussed in §5.2, the pre-factor involves the reduced determinant, where the four translational zero eigenvalues are subtracted. The reduced contribution from the $l = 1$ modes is defined as

$$\mathcal{O}_l\psi_l = \gamma_n\psi_l \implies \mathcal{R}_1'(\infty) = \frac{\prod_{n=2}^{\infty}\gamma_n}{\prod_{n=1}^{\infty}\gamma_n^{\rm FV}}\,. \tag{5.22}$$

This is a straightforward procedure when γ_n are known for the principal quantum numbers n. However, with the Gel'fand-Yaglom approach, the eigenvalues are re-grouped in terms of orbital l modes. Thus the zero from translations has to be removed carefully, because it multiplies all the other eigenvalues with $l = 1$.

This can be done perturbatively [9, 182, 183, 193] by off-setting the fluctuation potential with a small dimensionful parameter μ_ε^2 and finding the corresponding eigenfunctions of

$$\left(\mathcal{O}_1 + \mu_\varepsilon^2\right)\psi_1^\varepsilon = 0\,. \tag{5.23}$$

Instead of approaching zero, the ratio of determinants is then given by

$$\mathcal{R}_1^\varepsilon(\infty) = \frac{\psi_1^\varepsilon(\infty)}{\psi_{\rm FV1}(\infty)} \simeq \frac{(\mu_\varepsilon^2+\gamma_1)\prod_{n=2}^{\infty}\gamma_n}{\prod_{n=1}^{\infty}\gamma_n^{\rm FV}} = \mu_\varepsilon^2\mathcal{R}_1'(\infty)\,, \tag{5.24}$$

because the μ_ε^2 shift does not affect $\gamma_{n>1}$ and $\gamma_n^{\rm FV}$. In other words, we need to compute

$$\mathcal{R}_1'(\infty) = \lim_{\mu_\varepsilon^2\to 0}\frac{1}{\mu_\varepsilon^2}\mathcal{R}_1^\varepsilon(\infty)\,. \tag{5.25}$$

The eigenfunctions ψ_1^ε are infinitesimally close to ψ_1 and we can perform a perturbative expansion $\psi_1^\varepsilon \simeq \psi_1 + \mu_\varepsilon^2\,\delta\psi_1$, which enters in (5.23) such that

$$\left(\mathcal{O}_1 + \mu_\varepsilon^2\right)\left(\psi_1 + \mu_\varepsilon^2\delta\psi_1\right) \simeq \mathcal{O}_1\psi_1 + \mu_\varepsilon^2\left(\psi_1 + \mathcal{O}_1\delta\psi_1\right) = 0\,. \tag{5.26}$$

The general solution ψ_{ls} in (5.14) is singular for $l = 1$, so we re-derive it

$$\psi_{1s} = \frac{R_s^4\rho}{\left(R_s^2-\rho^2\right)^2}\left(A_{1s} + B_{1s}\left(\frac{\rho^4}{R_s^4} - 8\frac{\rho^2}{R_s^2} + 24\log\rho + 8\frac{R_s^2}{\rho^2} - \frac{R_s^4}{\rho^4}\right)\right)\,. \tag{5.27}$$

On the first segment with $s = 1$, the ψ_{11} needs to be regular at $\rho = 0$ and normalized to the FV, therefore $A_{11} = 1$ and $B_{11} = 0$. Matching to the second segment at R_T gives $A_{12} = x^6 y^2$ and $B_{12} = 0$. The value at infinity is then given by $\psi_{12}(\infty) \propto B_{12} = 0$, as it should be since we are looking at the zero eigenvalue and $\mathcal{R}_1(\infty) \propto \psi_{12}(\infty) = 0$.

Now that we have the $l = 1$ fluctuation, let us move on to perturbations $\delta\psi_{1s}$, given by the non-homogeneous equation $\mathcal{O}\delta\psi_1 = -\psi_1$ that comes from (5.26) and get

$$\delta\psi_{1s} = \frac{3R_s^6\rho}{4\left(R_s^2-\rho^2\right)^2}\left(\delta A_{1s} + \frac{\delta B_{1s}}{18}\left(\frac{\rho^4}{R_s^4} - 8\frac{\rho^2}{R_s^2} + 24\log\rho + 8\frac{R_s^2}{\rho^2} - \frac{R_s^4}{\rho^4}\right) - \frac{A_{1s}}{18}\left(6\frac{\rho^2}{R_s^2} - 18 - 24\log\rho - \frac{R_s^2}{\rho^2} + \frac{R_s^4}{\rho^4}\right)\right). \tag{5.28}$$

The boundary conditions $\delta\psi_{11}(0) = \dot{\delta\psi}_{11}(0) = 0$ fix $\delta A_{11} = \delta B_{11} = -1$ on the first segment[2] and the same matching conditions required for ψ_l in (5.16), apply to $\delta\psi_l$. These determine the remaining δA_{12} and $\delta B_{12} = 3\lambda/(8\pi^2)\mathcal{S}_0 x^6 y^2$.

In fact, it is δB_{12} that gives the reduced determinant after plugging the expansion in (5.25)

$$\mathcal{R}_1'(\infty) = \lim_{\mu_\varepsilon^2\to 0}\frac{1}{\mu_\varepsilon^2}\frac{\psi_1 + \mu_\varepsilon^2\delta\psi_1}{\psi_{\rm FV1}}\Big|_{\rho=\infty} = \frac{\delta\psi_1}{\psi_{\rm FV1}}\Big|_{\rho=\infty} = \frac{R_2^2}{24}\delta B_{12} = \frac{R_2^2}{24}\left(\frac{3\lambda}{8\pi^2}\right)\mathcal{S}_0 x^6 y^2\,, \tag{5.29}$$

where we used the fact that $\psi_1(\infty) = 0$ and R_2 was calculated in (2.41). Note that the $\mathcal{R}_1'$ is proportional to $\mathcal{S}_0$, which cancels with the prefactor in (5.7). The reduced determinant has the correct dimension of mass^{-2}, set by the dimensional R_2, which is proportional to $1/v$, the energy scale of the model. The dimensionless δB_{12} serves as the numerical pre-factor that diverges in the TW limit and gives an additional suppression to the rate. With the $l = 1$ zero removed, we can proceed to the finite part.

5.3.3 Finite sum

With $\mathcal{R}_l$ in (5.10) at hand, the finite part can be computed in some generality. Let us consider a generic form of $\mathcal{R}_l$, given by a ratio of polynomials of order n

$$\mathcal{R}_l(\infty) = \prod_{i=1}^{n}\frac{l+1-a_i}{l+1-b_i}\,, \tag{5.30}$$

which covers the results in (5.15) and (5.17). The number of roots and poles must be the same, a consequence of the normalization to the FV in (5.10). To get the finite part of (5.10), we first find the asymptotic behavior of $\mathcal{R}_l$ by expanding the log of the determinant for large l. The degeneracy factor goes as l^2, therefore the $\ln\mathcal{R}_l$ has to be expanded up to $1/l^3$ to account for the quadratic, linear and log divergencies.

[2]The single quartic case $\lim_{\rho\to\infty}\delta\psi_{11}/\rho = -R^2/24$ becomes consistent with the SM [6, 9] after flipping the sign of V'', because we assumed $\lambda > 0$.

It turns out that the asymptotics of the zeta function, used for renormalization, will be given in powers of $\nu = l + 1$, therefore it is convenient to define $\mathcal{R}_l^a$ by expanding (5.10) in $1/\nu$ up to $\mathcal{O}(\nu^{-3})$. This is subtracted from (5.10) and we get

$$\Sigma_f = \sum_{\nu=1}^{\infty} \nu^2 \left(\ln \mathcal{R}_l(\infty) - \ln \mathcal{R}_l^a(\infty) \right), \tag{5.31}$$

which is convergent and can be computed[3] in a closed form

$$\begin{aligned} \Sigma_f = \sum_{i=1}^{n} \Bigg(& \frac{a_i^3}{3}\gamma_E - \frac{a_i}{12}\left(1 + 3a_i - 6a_i^2\right) - \zeta_R'\left(-2, 3 - a_i\right) - 2a_i\zeta_R'\left(-1, 3 - a_i\right) \\ & - a_i^2\zeta_R'\left(0, 3 - a_i\right) - (a \to b) \Bigg) + \ln \mathcal{R}_0(\infty) + 4 \ln \mathcal{R}_1'(\infty) \,. \end{aligned} \tag{5.32}$$

Here, $\zeta_R'(s, a)$ is the derivative over s of the generalized Riemann zeta function and γ_E is the Euler's constant. Finally, the three roots a_i of the polynomial in (5.17) are

$$a_i = 1 - \left(c_2 + \chi_i \left(c_2^2 - 3c_1 \right) / \theta + \chi_i^* \theta \right) / 3 \,, \tag{5.33}$$

with $\theta^3 = 9/2 \left(c_1 c_2 - 3c_0 - 2/9 c_2^3 + \sqrt{(27c_0^2 + 4c_1^3 - 18c_0c_1c_2 - c_1^2c_2^2 + 4c_0c_2^3)/3} \right)$ and $\chi = \{-1, (1 \pm i\sqrt{3})/2\}$, while c_i are given in (5.18)-(5.20). This completes the finite part of the decay rate. Next, we are going to recover the asymptotic terms $\mathcal{R}_l^a$ that were subtracted in (5.31) using the zeta function regularization.

5.4 Zeta function regularization

The decay rate in (5.7) is a physical quantity that depends on the parameters of the potential $V(\varphi)$ in $\mathcal{S}[\varphi]$. These need to be renormalized to make connections between measurements, such as decay rates and scattering cross-sections, observed at the minimum of the potential. Most commonly, the renormalization is done perturbatively via Feynman diagrams and dimensional regularization. It introduces an arbitrary renormalization scale μ to keep the mass dimensions for any D and ascribes $1/(4 - D)$ poles to divergent parts of the momentum integrals. Within a chosen subtraction scheme, such as $\overline{\text{MS}}$, on-shell or other, the renormalized parameters (or counter-terms) will remove infinities in physical quantities.

The above holds for the FV decay rate in (5.7) as well [186]. One can compute the UV part of the determinant with Feynman diagrams [9, 98, 99, 182, 183, 195] for scalars, fermions and gauge bosons. The counter-terms used for other processes, will also make the effective action and therefore the rate, finite. For the effective action that describes the UV part of the FV decay rate to be consistent with the finite sum over the eigenvalues, the asymptotic parts are computed by expanding in terms of insertions of $V''(\rho)$. In the SM this is equivalent to insertions of the quartic and gauge couplings, which defines the power counting.

[3] Technically, we do the sum over $\mathcal{R}_l(\infty)$ from $\nu = 3$ up to a large finite regulator to skip the $l = 0, 1$ modes, which are then added by hand. The sum over $\mathcal{R}_l^a(\infty)$ starts from $\nu = 1$ as in the renormalization procedure. After the summation, the regulator disappears and can be taken to infinity.

Alternatively, the UV part of the determinant can be defined by use of the zeta function [196, 197], see [198] for a review[4]. The zeta function formalism was applied to FV decay in the early works [102] and more recently in [100]. We will review its introduction via the contour integral [199, 200, 202, 203] in the following section. Similarly to dimensional regularization, the renormalization scale is introduced for dimensional reasons to define the zeta function for any value of its argument. As with Feynman diagrams, the UV part is computed perturbatively in powers of V''. However, contrary to the diagrammatic approach, the UV part is an expansion in powers of l and therefore serves as a convenient UV regulator. Finally, the renormalization is performed by an analytic continuation of the zeta function and follows from the analyticity of the Riemann zeta function. We will see that the final result for the single quartic rate via Feynman diagrams agrees with the zeta function approach.

5.4.1 Zeta function via contour integral

Let us begin by redefining the sum over the eigenvalues of $\mathcal{O}$ in terms of the zeta function

$$\ln\det\mathcal{O}=\sum_{\mathbf{n}}\ln\gamma_{\mathbf{n}}=-\frac{\mathrm{d}}{\mathrm{d}s}\sum_{\mathbf{n}}\left(\frac{\mu^2}{\gamma_{\mathbf{n}}}\right)^s\Bigg|_{s=0}=-\frac{\mathrm{d}}{\mathrm{d}s}\left(\mu^{2s}\,\zeta_{\mathcal{O}}(s)\right)\Big|_{s=0}, \tag{5.34}$$

where $\mathbf{n}$ stands for all the quantum numbers and μ is the renormalization scale, which keeps the sum over eigenvalues dimensionless for all values of s. As found in [100], it will correspond to the same scale arising from dimensional regularization in the $\overline{\mathrm{MS}}$ scheme [98]. The zeta function, associated to the ratio of determinants, is then given by the difference

$$\zeta=\mu^{2s}\left(\zeta_{\mathcal{O}}-\zeta_{\mathcal{O}_{\mathrm{FV}}}\right)\qquad\text{and}\qquad\ln\left(\frac{\det\mathcal{O}}{\det\mathcal{O}_{\mathrm{FV}}}\right)=-\frac{\mathrm{d}}{\mathrm{d}s}\zeta(s)|_{s=0}\,. \tag{5.35}$$

The sum over eigenvalues in (5.34) converges if $\mathrm{Re}(s)>D/2$ [204]. However, to analytically continue ζ to the region of interest $s=0$, we have to regularize the integral.

To obtain the analytical structure of ζ in the range $\mathrm{Re}(s)\leq 2$, we conveniently recast the sum in (5.34) as a contour integral. For this purpose, let us consider $\mathcal{O}\psi(\rho,\gamma)=\gamma\psi(\rho,\gamma)$, where γ is a continuous complex parameter. The $\psi(\gamma)$ is a generalization of $\psi_{\mathbf{n}}$ in the sense that when the boundary conditions in (5.8) are imposed, γ becomes quantized and $\psi_{\mathbf{n}}$ is recovered with $\gamma\to\gamma_{\mathbf{n}}$. Now, the zeta function can be defined as a contour integral

$$\zeta_{\mathcal{O}}=\sum_{\mathbf{n}}\frac{1}{\gamma_{\mathbf{n}}^s}=\frac{1}{2\pi i}\oint\frac{\mathrm{d}\gamma}{\gamma^s}\frac{\mathrm{d}}{\mathrm{d}\gamma}\ln\psi(\infty,\gamma)\,. \tag{5.36}$$

The sum over eigenvalues $\gamma_{\mathbf{n}}^{-s}$ is recovered because the simple poles are set by $\mathrm{d}\ln\psi/\mathrm{d}\gamma=\psi'/\psi$ and the boundary condition $\psi(\infty,\gamma)\xrightarrow{\gamma\to\gamma_{\mathbf{n}}}0$. Thus, by the residue theorem, the integral in (5.36) sums up all the eigenvalues, as long as the integration contour runs counterclockwise and encloses the entire real axis, as the solid red line in fig. 5.1.

[4] For a pedagogical introduction with examples regarding the use of spectral functions/functional determinants in physical settings, see [110, 199, 200, 201].

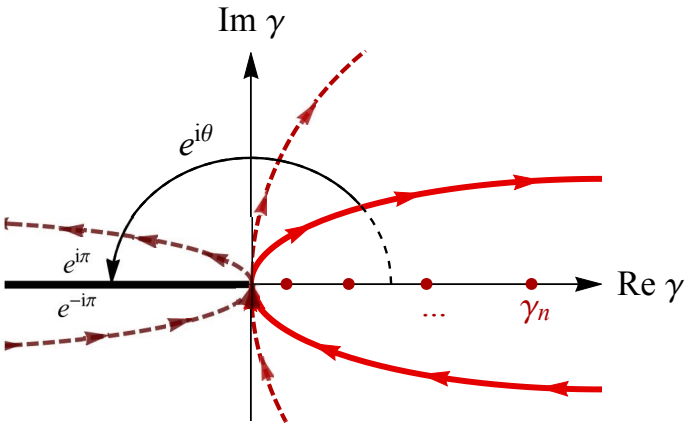

Figure 5.1: Deformation of the integration contour of eq. (5.36) from the positive real axis to the negative one. The red dots represent the location of the poles such that $\psi(\infty,\gamma)=0$.

Here, we have to deform the contour from the positive real axis, which encloses all the eigenvalues, to the negative one. For this purpose, we split the contour in two paths, parametrized in the complex plane by $\exp(\pm i\theta)\gamma$. As shown in fig. 5.1, we start with a path that runs along the positive real axis,

$$\zeta_{\mathcal{O}}=\frac{1}{2\pi i}\left(\int_0^\infty \mathrm{d}\gamma\frac{e^{i\theta s}}{\gamma^s}\frac{\mathrm{d}}{\mathrm{d}\gamma}\ln\psi(\infty,e^{-i\theta}\gamma)+\int_\infty^0 \mathrm{d}\gamma\frac{e^{-i\theta s}}{\gamma^s}\frac{\mathrm{d}}{\mathrm{d}\gamma}\ln\psi(\infty,e^{i\theta}\gamma)\right). \quad (5.37)$$

Then we deform the path to the negative real axis by taking the limit $\theta\to\pi$ and get

$$\zeta_{\mathcal{O}}=\frac{\sin\pi s}{\pi}\int_0^\infty\frac{\mathrm{d}\gamma}{\gamma^s}\frac{\mathrm{d}}{\mathrm{d}\gamma}\ln\psi(\infty,-\gamma)\,, \quad (5.38)$$

where we assume that ψ is continuous around the negative real axis, such that $\psi(\rho,e^{\pm i\pi}\gamma)=\psi(\rho,-\gamma)$. Finally, since we are considering a hyper-spherically symmetric potential, we can separate the variables

$$\mathcal{O}_l\psi_l(\rho,\gamma)=\gamma\,\psi_l(\rho,\gamma)\,, \quad (5.39)$$

and take into account the degeneracy of the orbital modes. Using (5.35) and (5.38) the zeta function for the ratio of determinants is

$$\zeta=\frac{\sin\pi s}{\pi}\mu^{2s}\sum_\nu\nu^2\int_0^\infty\frac{\mathrm{d}\gamma}{\gamma^s}\frac{\mathrm{d}}{\mathrm{d}\gamma}\ln\left(\frac{\psi_l(\infty,-\gamma)}{\psi_l^{\mathrm{FV}}(\infty,-\gamma)}\right). \quad (5.40)$$

Alas, a closed form solution of $\psi_l(\rho,\gamma)$ cannot be obtained in general, even for the single quartic potential. Since we are only interested in the asymptotic behavior $\psi_l(\infty,\gamma)$ near the FV, it is enough to consider the expansion around the FV, where the solution of (5.39) is

$$\psi_l^{\mathrm{FV}}(\rho,-\gamma)=I_\nu\left(\sqrt{\gamma}\rho\right)/\rho\,. \quad (5.41)$$

The K_ν part is discarded due to regularity at $\rho=0$ and the normalization factor is chosen to be one. When $\rho\to\infty$, the fluctuation potential approaches the FV[5] and

[5] In general, one should subtract V''_{FV} from the fluctuation potential $V''\to V''-V''_{\mathrm{FV}}$ and shift the eigenvalues $\gamma\to\gamma-V''_{\mathrm{FV}}$ in (5.38) and (5.39), modifying the lower limit of integration. For quartic potentials $V''_{\mathrm{FV}}=0$.

we can set up an approximate solution

$$\psi_l(\rho,-\gamma) \simeq f_l\,(\gamma)\;\psi_l^{\rm FV}(\rho,-\gamma)\,, \tag{5.42}$$

where $f_l\,(\gamma)$ is a constant to be determined in the section below. The K_ν term was neglected, because it vanishes in the asymptotic limit. With this ansatz, (5.40) becomes

$$\zeta = \frac{\sin\pi s}{\pi}\mu^{2s}\sum_\nu \nu^2 \int_0^\infty \frac{\mathrm{d}\gamma}{\gamma^s}\frac{\mathrm{d}}{\mathrm{d}\gamma}\ln f_l\,(\gamma)\;, \tag{5.43}$$

which is valid for $\mathrm{Re}(s) > 2$. In order to make it well defined around $s = 0$, we have to find the asymptotic form of f_l and renormalize it.

5.4.2 Renormalization of the functional determinant

To perform the analytical continuation of ζ to $s = 0$, we define its asymptotic limit by expanding (5.43) in the large l limit

$$\zeta_a = \frac{\sin\pi s}{\pi}\mu^{2s}\sum_\nu \nu^2 \int_0^\infty \frac{\mathrm{d}\gamma}{\gamma^s}\frac{\mathrm{d}}{\mathrm{d}\gamma}\ln f_l^a(\gamma)\,, \tag{5.44}$$

and compute f_l^a perturbatively by expanding around the FV. Once we have ζ_a, we subtract it from ζ, which removes the leading l divergence and produces the finite result

$$\zeta_f = \zeta - \zeta_a\,, \tag{5.45}$$

similarly to what was done for the finite sum in §5.3.3. Finally, the divergent terms in ζ_a will be renormalized using the analytic properties of the Riemann zeta function.

Asymptotic expansion of the zeta. As discussed above, we would like to compute (5.44) by considering a double expansion. First, $\rho \to \infty$ in (5.40), which allows us to construct an implicit iterative solution around the FV for a fixed angular mode l. Then the high-l expansion can be performed and we end up with a closed form expression for ζ_a.

False vacuum expansion. When approaching the FV, (5.39) can be solved by starting from $\psi_l^{\rm FV}(\rho,-\gamma)$, given by (5.41), and writing down the general ansatz

$$\psi_l(\rho,-\gamma) = \psi_l^{\rm FV}(\rho,-\gamma) + \int_0^\rho \mathrm{d}\rho_1 G(\rho,\rho_1)V''(\rho_1)\psi_l(\rho_1,-\gamma)\,, \tag{5.46}$$

$$G(\rho,\rho_1) = \frac{\rho_1^2}{\rho}\left(I_\nu(\sqrt{\gamma}\rho)K_\nu(\sqrt{\gamma}\rho_1) - I_\nu(\sqrt{\gamma}\rho_1)K_\nu(\sqrt{\gamma}\rho)\right)\,, \tag{5.47}$$

where G is the Green function associated with $\mathcal{O}_l$. This is a self-referential integral equation, which can be solved iteratively by starting in the FV and expanding in powers of V''. The iteration stops when the zeta function becomes well defined in the asymptotic UV limit and describes all the high l modes.

Actually, we already know from the normalization in (5.10) and the discussion regarding the finite sum in §5.3.3 that the asymptotic terms need to go up to ν^{-3}. In the doubly asymptotic limit when $\rho, \nu \to \infty$, the Green function is proportional

to $1/\nu$, which follows from the properties of Bessel functions in the appendix §C.3. Thus, each insertion of V'' in (5.46) comes with a factor of $1/\nu$ and it is enough to expand the zeta up to $\mathcal{O}(V''^3)$. Using (5.42) and (5.46) we have

$$\frac{\psi_l(\infty,-\gamma)}{\psi_l^{\rm FV}(\infty,-\gamma)} = f_l(\gamma) = 1 + \int_0^\infty \mathrm{d}\rho\rho^2 K_\nu(\sqrt{\gamma}\rho)V''(\rho)\psi_l(\rho,-\gamma)\,, \tag{5.48}$$

$$= 1 + f_l^{(1)} + f_l^{(2)} + f_l^{(3)} + \mathcal{O}(V''^4)\,, \tag{5.49}$$

while expanding the log to the same order gives

$$\ln f_l(\gamma) \simeq f_l^{(1)} - \frac{1}{2}\left(f_l^{(1)2} - 2f_l^{(2)}\right) + \frac{1}{3}\left(f_l^{(1)3} - 3f_l^{(1)}f_l^{(2)} + 3f_l^{(3)}\right)\,. \tag{5.50}$$

The integrals $f_l^{(n)}$ are obtained by iterating (5.46)

$$f_l^{(1)} = \int_0^\infty \mathrm{d}\rho_1\rho_1 V''(\rho_1)K_\nu(\sqrt{\gamma}\rho_1)I_\nu(\sqrt{\gamma}\rho_1)\,, \tag{5.51}$$

$$f_l^{(2)} = \int_0^\infty \mathrm{d}\rho_1\rho_1^2 V''(\rho_1)K_\nu(\sqrt{\gamma}\rho_1)\int_0^{\rho_1}\mathrm{d}\rho_2 G_{12}V''(\rho_2)\frac{I_\nu(\sqrt{\gamma}\rho_2)}{\rho_2}\,, \tag{5.52}$$

$$f_l^{(3)} = \int_0^\infty \mathrm{d}\rho_1\rho_1^2 V''(\rho_1)K_\nu(\sqrt{\gamma}\rho_1)\int_0^{\rho_1}\mathrm{d}\rho_2 G_{12}V''(\rho_2)\int_0^{\rho_2}\mathrm{d}\rho_3 G_{23}V''(\rho_3)\frac{I_\nu(\sqrt{\gamma}\rho_3)}{\rho_3}\,, \tag{5.53}$$

where $G_{ij} = G(\rho_i,\rho_j)$. This concludes the FV expansion in V'' and we can focus on isolating the high-l behavior.

High-l expansion. We would like to expand $f_l^{(i)}$ for high l up to $\mathcal{O}(\nu^{-3})$ while keeping $\rho\to\infty$. To this end, we evaluate the Bessel functions in (5.51)-(5.53) in the limit when $\nu,\rho\to\infty$ with $\sqrt{\gamma}\rho/\nu$ fixed, and use the saddle point approximation, see (C.7)-(C.9) in the appendix §C.3 for technical details.

For continuous V'', the integrals in (5.51)-(5.52) were calculated by [99, 100] and (5.53) was not needed. Here, we extend the analysis to take into account the delta function

$$V''(\rho) = \sum_s V_s''(\rho)H\left((-1)^s(\rho-R_T)\right) - \mu_V\delta(\rho-R_T)\,. \tag{5.54}$$

Performing the integrals (5.51)-(5.53) requires some effort and we leave the details to the appendix §C.4. The final result up to $\mathcal{O}\left(\sqrt{\gamma}/\nu\right)^4$ is fairly compact

$$\begin{aligned}\ln f_l^a = \sum_s \int_0^\infty \mathrm{d}\rho\rho V_s''\left(\frac{t}{2\nu} + \frac{t^3}{16\nu^3}\left(1-6t^2+5t^4-2\rho^2V_s''\right)\right)H\left((-1)^s(\rho-R_T)\right)\\ -(\mu_V R_T)\left(\left(\frac{t}{2\nu}+\frac{t^3}{16\nu^3}\left(1-6t^2+5t^4\right)\right) + (\mu_V R_T)\frac{t^2}{8\nu^2}\right.\\ \left.+(\mu_V R_T)^2\frac{t^3}{24\nu^3}\left(1-\frac{3}{\mu_V^2}\left(V_1''+V_2''\right)\right)\right)\Big|_{\rho=R_T}\,,\end{aligned} \tag{5.55}$$

where $t = 1/\sqrt{1+\gamma\left(\rho/\nu\right)^2}$. The first line corresponds to the continuous part of V'' and reproduces the known results of [100] when $V''_{\rm FV}=0$. The terms proportional to μ_V are new because of the presence of the delta at R_T. This completes the asymptotic description of zeta and (5.55) can be used to evaluate the finite sum and carry out the renormalization.

Regularization of the finite zeta. The asymptotic form of the zeta function allows us to regulate the large l infinities and compute the finite sum, similarly to what we did in §5.3.3. From (5.44) and (5.45) we have

$$\zeta_f = \frac{\sin \pi s}{\pi} \sum_\nu \nu^2 \mu^{2s} \int_0^\infty \frac{\mathrm{d}\gamma}{\gamma^s} \frac{\mathrm{d}}{\mathrm{d}\gamma} \left(\ln f_l(\gamma) - \ln f_l^a(\gamma) \right) , \tag{5.56}$$

which is finite and analytic in the neighbourhood of $s = 0$. This means we can take the derivative with respect to s and evaluate $\zeta_f'(0)$. In doing that, the terms proportional to $\sin \pi s$ vanish, γ^{-s} goes to one and the integral can be computed trivially by evaluating the terms on the boundaries.

On the upper limit $\gamma \to \infty$ and $V''(\rho)$ in (5.39) vanishes, thus $\psi_l(\rho, \gamma)$ goes to the FV solution and $f_l(\gamma \to \infty) \to 1$ for both log terms in (5.56), which go to zero. This leaves us with the two terms on the lower boundary, when $\gamma \to 0$ (and $\rho \to \infty$, as usual). First, from the definition of $f_l(\gamma)$ in (5.42) and from (5.39), it becomes clear that we end up with the same equation (5.9) that defined $\mathcal{R}_l(\infty)$. In other words, $f_l(0) = \mathcal{R}_l(\infty)$. Second, we need to evaluate the asymptotic part $f_l^a(0)$ by setting $\gamma = 0$ in (5.55) which sets $t = 1$ and we can integrate over ρ for a specific fluctuation potential. Now the finite sum can be performed and we reproduce Σ_f in (5.31), such that

$$-\zeta_f'(0) = \sum_\nu \nu^2 \left(\ln \mathcal{R}_l(\infty) - \ln f_l^a(0) \right) = \Sigma_f \, , \tag{5.57}$$

for the single and the bi-quartic potential. As a very non-trivial cross-check of the asymptotics, we find that f_l^a computed from (5.55), which is defined directly in terms of V'', is precisely equal to the one from $\mathcal{R}_l(\infty)$ in (5.30), i.e. $f_l^a(0) = \mathcal{R}_l^a(\infty)$.

The procedure that gave (5.57) does not always reproduce the finite sum Σ_f. In particular, when $V''_{\mathrm{FV}} \neq 0$, the lower limit of integration over γ is shifted from 0 to $\sqrt{V''_{\mathrm{FV}}}$, and we have to evaluate $f_l^a(\sqrt{V''_{\mathrm{FV}}})$. In this case, additional terms appear in (5.55) when we expand $t \neq 1$. However, this is an over-subtraction [100] – such terms are suppressed by $1/\nu^4$ or more and get cancelled by the renormalized parts below.

Renormalization of the asymptotic zeta. The asymptotic part of the zeta function can now be renormalized. The integrals in (5.55) are evaluated using the following identity, valid for $\mathrm{Re}(s) < 1$

$$\frac{\sin \pi s}{\pi} \mu^{2s} \int_0^\infty \frac{\mathrm{d}\gamma}{\gamma^s} \frac{\mathrm{d}}{\mathrm{d}\gamma} t^n = -\frac{\Gamma\left(s + \frac{n}{2}\right) (\mu\rho)^{2s}}{\Gamma(s)\,\Gamma\left(\frac{n}{2}\right)} \nu^{-2s} \, . \tag{5.58}$$

The resulting expressions are plugged into (5.44) and we perform the sum over ν. Each term that goes as $(t/\nu)^n$ gives a Riemann zeta $\zeta_R(2s + n - 2)$. The analytic continuation properties of ζ_R are well known and provide a mathematical description of divergencies. Finally, we take the derivative over s and send s to zero, ending up with

$$\begin{aligned} \zeta_a'(0) = &\sum_s \frac{1}{8} \int_0^\infty \mathrm{d}\rho \, \rho^3 V_s''^2 \left(\ln\left(\frac{\mu\rho}{2}\right) + \gamma_E + 1 \right) H\left((-1)^s (\rho - R_T) \right) \\ &- \frac{(\mu_V R_T)^2}{16} + \frac{(\mu_V R_T)^3}{24} \left(1 - \frac{3}{\mu_V^2} \left(V_1'' + V_2'' \right) \big|_{R_T} \right) \left(\ln\left(\frac{\mu R_T}{2}\right) + \gamma_E + 1 \right) . \end{aligned} \tag{5.59}$$

It agrees with (5.12) for a continuous V'' with $\mu_V = 0$ and $V''_{\rm FV} = 0$ and also reproduces the SM [9], when applied to the single quartic. This demonstrates that the Feynman diagrammatic approach coincides with the zeta function formalism. Another non-trivial check regards the cancellation of divergences, i.e. we verify that terms proportional to γ_E in Σ_f given by (5.32) cancel the ones in $\zeta'_a(0)$ above.

Let us comment on the renormalization scale dependence. The FV decay is a physical process and the rate should not depend μ. Specifically, the μ dependence from the prefactor cancels the $\ln\mu$ from running of parameters in the bounce action $\mathcal{S}_0$. For the single quartic case this is easy to see. The first segment gives $1/2\zeta'_a(0) \supset 3\ln\mu$, while the running of the quartic $\beta_\lambda = d\lambda/d\ln\mu = 9\lambda^2/(8\pi^2)$ is solved for $\lambda(\mu)$ and plugged into the bounce action $-8\pi^2/(3\lambda(\mu))$ to cancel the pre-factor μ dependence. While running the bi-quartic potential couplings is beyond the scope of this work, we confirm that the leading order running of $\lambda_{1,2}$ with the above beta functions cancels the μ dependence of the continuous part of (5.59) in the weakly coupled limit when x and y are small.

5.5 Summary of decay rates

The final result for the renormalized log of the functional determinant is

$$\ln\left(\frac{\det\mathcal{O}}{\det\mathcal{O}_{\rm FV}}\right) = -\zeta'(0) = -\zeta'_f(0) - \zeta'_a(0)\,, \tag{5.60}$$

where $-\zeta'_f(0) = \Sigma_f$ can be found in (5.32) and $\zeta'_a(0)$ in (5.59). Therefore, the total decay rate per 4D unit volume is

$$\frac{\Gamma}{\mathscr{V}} = \left(\frac{\mathcal{S}_0}{2\pi}\right)^2 e^{-\mathcal{S}_0+\frac{1}{2}\zeta'(0)} = v^4 e^{-\mathcal{S}_0-\mathcal{S}_1}\,, \tag{5.61}$$

where the $\mathcal{S}_0$ comes from (2.42) and $\zeta'(0)$ is the sum of (5.32) and (5.59). As we will see, having a closed form result is particularly useful to study the behavior of the rate in the TW limit as well as for the large scale separation $x \gg 1$, corresponding to a rather flat potential.

5.5.1 Real quartic

To complete the calculation for the real scalar part, we evaluate the integral in (5.59) in a closed form with $R_{1,2,T}$ and μ_V given by (2.41) and (5.16), respectively. This is a straightforward calculation, but we omit the entire expression for brevity and instead show the negative log of the normalized rate $-\ln\Gamma/\mathscr{V}/v^4$ in fig. 5.2. The total rate is shown by the black solid line on fig. 5.2 for a fixed $\lambda_1 = \lambda_2 = 1$ as $x = v_1/v_2$ interpolates from the TW $x \sim 1$ to the thick wall and a flat potential when $x \gg 1$. We assume that all the couplings are defined at v and set the renormalization scale to $\mu = v$. In this case, the rate is insensitive to v, apart from the overall normalization factor v^4, which is factorized in the plot.

The contribution from the semiclassical action $\mathcal{S}_0$ in the first term of (5.62) coming from the bounce action is shown in dashed red and tends to dominate for small x, as long as λ is small. The prefactor correction $\mathcal{S}_1$ is plotted in dashed yellow. It is sub-dominant for small values of x and starts to dominate for $x \sim 4$, the rate

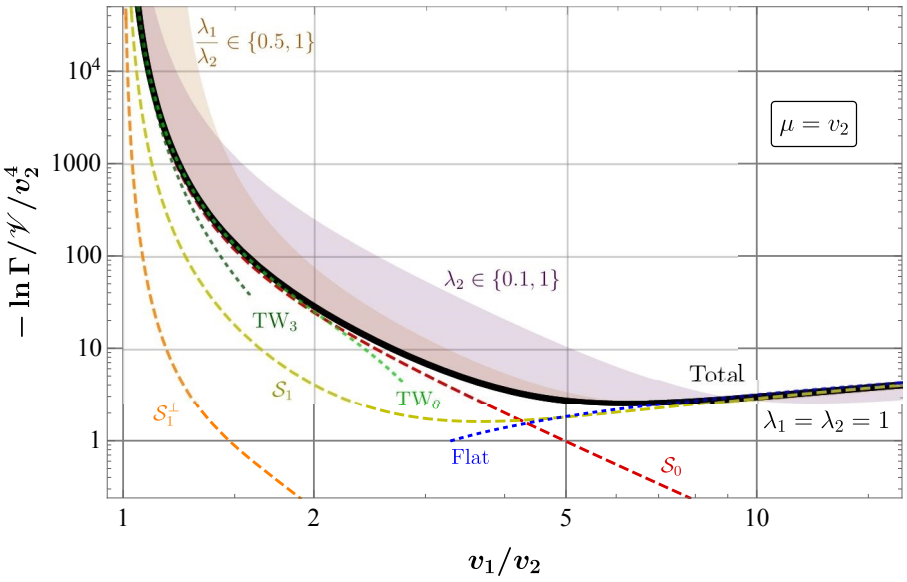

Figure 5.2: The FV decay rate for the bi-quartic potential in (2.39). The black solid line shows the total rate, while the dashed ones show the semiclassical part $\mathcal{S}_0$ in red and the finite renormalized prefactor $\mathcal{S}_1$ in dark yellow. The dotted lines correspond to the TW leading expansion, where we set $y = \lambda_1/\lambda_2 = 1$ and expand up to $(x-1)^{-3}$ in dark green, additional corrections up to $(x-1)^0$ in light green and the flat potential limit $x = v_1/v_2 \gg 1$ in blue. The shaded regions show the variation of $\lambda_2 \in \{0.1, 1\}$ in purple and $\lambda_1/\lambda_2 \in \{0.5, 1\}$ in light brown.

drops and then rises logarithmically. At this point, we should be worried about the validity of our semiclassical approximation. After all, the small-$\hbar$ approximation breaks down when the size of the coupling is large[6] [30]. In this limit, the one loop perturbative running is not self-consistent and the μ term becomes large. We will come back to this point in more details below, at the end of this section. In any case, lowering λ_2 results in a higher $\mathcal{S}_0$ which dominates the $\mathcal{S}_1$ for larger values of x, as shown by the purple shaded region. The variation of y, on the other hand, results in a shift of the entire curve to larger x, as shown by the brown shaded region, because the thin wall pole in the rate happens when $x^4 y \simeq 1$.

The behavior of the rate simplifies considerably in these two limits. Near the thin wall $x^4 y \sim 1$ (TW: $x \sim 1+\varepsilon, y = 1$), the a_i become large and negative, thus the asymptotic expansion of $\zeta'(s, 3-a_i)$ in (C.10)-(C.12) can be used. Conversely, the a_i become nearly constant when $x \gg 1$ (flat) and we have

$$-\ln \frac{\Gamma}{\mathscr{V}} \frac{1}{v^4} \simeq \begin{cases} \frac{2\pi^2}{3\lambda\varepsilon^3}\left(1 + \frac{\lambda}{8\pi^2}\left(\frac{8}{3} + 2\sqrt{3}\pi - \ln 2 - \ln\frac{\lambda v^2}{\mu^2}\right)\right), & \text{TW}, \\ \frac{32\pi^2}{3y\lambda x^3}\left(1 + \frac{y\lambda x^3}{16\pi^2}\left(\frac{7}{8} - 3\zeta_R'(-1) + \frac{1}{2}\ln\frac{2}{\pi} + \ln\frac{y\lambda x^3 v^2}{\mu^2}\right)\right), & \text{Flat}. \end{cases} \tag{5.62}$$

The leading TW functional dependence goes as ε^{-3}, which is the same as in the TW approximation of the displaced quadratic potential [102], with different numerical coefficients and an additional log term. The TW series can easily be extended to

[6] To see this point, note that in the Feynman's path-integral (5.1), we can define $\varphi' = \sqrt{\lambda}\hbar$ such that $S_E[\varphi]/\hbar = S_E[\varphi']/\lambda\hbar$. Thus the relevant expansion parameter is actually $\lambda\hbar$, which implies that small-$\hbar$ approximations are equivalent to weak-coupling approximations, small λ approximations.

arbitrary order in ε; we plot the leading ε^{-3} and the expansion up to ε^0 with the dotted green lines in fig. 5.2. These two are fairly good proxies and cover a significant portion of parameter space, as seen from fig. 5.2.

Finally, let us inspect when the small-$\hbar$ approximation breaks down. For this purpose we should impose the condition that the quantum corrections remain always smaller than the bounce action. Assuming that log terms are order one, from eq (5.62) we get

$$\lambda < \frac{24\pi^2}{5 + 6\sqrt{3}\pi - 3\ln 2} \approx 2\pi, \tag{5.63}$$

$$\lambda y x^3 < \frac{128\pi^2}{15 - 24\zeta'(-1) + \ln 16 - 4\ln \pi} \approx 24\pi. \tag{5.64}$$

For fixed $\lambda = y = 1$ the constraint on x, associated to fig. 5.2 is $x < 4.2$. These conditions are model dependent and define the validity of our saddle point approximation.

5.5.2 Complexified quartic

Let us extend the analysis to the complexified version of the model and examine the effect of transverse fluctuations, coming from the imaginary field component. This is similar to the SM, where the would-be-Goldstones contribute as longitudinal components of gauge bosons. Consider a complex scalar field $\Phi = (\varphi + i\,\varphi_\perp)/\sqrt{2}$ and the complexified version of the potential

$$V = \left(\lambda_2 v_2^4 - \lambda_1 v_1^4 + \lambda_1 \left|\Phi + v_1\right|^4\right) H\left(\tilde{\Phi} - \Phi\right) + \lambda_2 \left|\Phi - v_2\right|^4 H\left(\Phi - \tilde{\Phi}\right), \tag{5.65}$$

where $\tilde{\Phi}(\Phi)$ describes the boundary between the two regions. It is chosen such that V is continuous in the $\varphi - \varphi_\perp$ plane and $\tilde{\Phi}$ goes to zero on the $\varphi_\perp = 0$ axis, reproducing (2.39). Parameters of the potential are still real and the bounce for the real component φ stays the same, as does the determinant.

The perpendicular component $\varphi_\perp$ carries no vev, because $v_{1,2} \in \mathbb{R}$, and its bounce is zero. The fluctuations $\psi_l^\perp$ are non-zero and obey

$$\mathcal{O}_\perp \psi_l^\perp = -\ddot{\psi}_l^\perp - \frac{3}{\rho}\dot{\psi}_l^\perp + \frac{l(l+2)}{\rho^2}\psi_l^\perp + V_\perp''\left(\overline{\varphi}\right)\psi_l^\perp = 0\,, \qquad V_\perp'' = \frac{1}{3}V''\,. \tag{5.66}$$

The FV normalization stays the same $\psi_{ls}^{\mathrm{FV}\perp} = \rho^l$, while the transverse fluctuations are simpler than the real scalar ones

$$\psi_{ls}^\perp = \frac{\rho^l\, R_s^2}{R_s^2 - \rho^2}\left(A_{ls}^\perp\left(1 - \left(\frac{l}{l+2}\right)\frac{\rho^2}{R_s^2}\right) + B_{ls}^\perp \frac{R_s^{2l+2}}{\rho^{2l+2}}\left(1 - \left(\frac{l+2}{l}\right)\frac{\rho^2}{R_s^2}\right)\right). \tag{5.67}$$

The boundary conditions fix $A_{l1}^\perp = 1, B_{l1}^\perp = 0$, such that dividing by ρ^l and taking the limit $\rho \to \infty$, we recover the single quartic global Goldstone [9]

$$\lambda\left|\Phi\right|^4 : \mathcal{R}_l^\perp(\infty) = \frac{l}{l+2}\,, \tag{5.68}$$

where the zero eigenvalue at $l = 0$ appears due to the $U(1)$ symmetry. Proceeding to the second segment and taking into account the matching conditions, we end up with

$$\mathcal{R}_l^{\perp}(\infty) = A_{l2}^{\perp}\,\frac{l}{l+2} = \frac{l^3 + c_2^{\perp} l^2 + c_1^{\perp} l + c_0^{\perp}}{(l+1)(l+2)^2}\,. \tag{5.69}$$

After adding the second segment, the $U(1)$ symmetry gets broken and the zero eigenvalue in (5.68) disappears. The coefficients are then given by $c_0^{\perp} = c_0/9$ and

$$c_1^{\perp} = \frac{2x\left((2x+1)x^2y+1\right)\left((4x+1)x^3y+x-2\right)}{3\left(x^4y-1\right)^2}\,,\quad c_2^{\perp} = \frac{(13x+4)x^3y+4x-5}{3(x^4y-1)}\,. \tag{5.70}$$

The $\mathcal{R}_l^{\perp}(\infty)$ goes to 1 as $l \gg 1$ and the ratio of determinants diverges. To get the total decay rate, we proceed as for the real quartic above. The solutions to the cubic polynomial in (5.69) are given by the same expression in (5.33) with replacing $c_i \to c_i^{\perp}$ and the fluctuation potential $V_{\perp}'' \to V''/3$. Again, the asymptotic behavior is simple

$$\mathcal{S}_1^{\perp} \simeq \begin{cases} \frac{1}{972\varepsilon^3}\left(152 - 8\ln 27 - 12\sqrt{11}\arctan\sqrt{11} - 57\ln\frac{2\lambda v^2}{\mu^2}\right), & \text{TW}\,, \\ \frac{322}{81}\ln 2 - \frac{1}{324} - \frac{\zeta_R(3)}{8\pi^2} - \frac{5}{2}\ln 3 + \frac{2}{81}\ln\frac{\lambda y x^3 v^2}{\mu^2} - \\ \qquad \frac{\zeta_R'\left(-2,\frac{7}{3}\right)}{2} - \frac{2\zeta_R'\left(-1,\frac{7}{3}\right)}{3} - \frac{2\zeta_R'\left(0,\frac{7}{3}\right)}{9}, & \text{Flat}\,, \end{cases} \tag{5.71}$$

and the total rate is obtained by adding $\mathcal{S}_1^{\perp}$ to $\mathcal{S}_1$ in (5.61). It turns out that the correction from the transverse fluctuations are rather small and subdominant with respect to the real scalar ones, as seen from the orange dashed line on fig. 5.2.

5.6 Conclusions and outlook

We presented a closed-form solution for the total decay rate at one loop for a potential with two tree level minima of a bi-quartic potential. Our approach is based on the Gel'fand-Yaglom theorem that evades the need to obtain individual eigenvalues of the fluctuation operator. However, the treatment of the renormalization procedure had to be generalized to include the delta functions in the fluctuation potential. To this end, an appropriate expansion of the fluctuation functions to the maximal $1/l^3$ term had to be performed to extract the UV behavior and regularize the determinant.

This work makes a significant step forward in computing the dimensionful prefactor and the impact of fluctuations for potentials/models with a large-ish separation of scales. We noticed that the estimation of the quantum corrections from the tree-level bounce action can be misleading, in particular when a large separation of scales is involved. In this cases, the couplings need to run and we have to include all the corrections of the same order consistently, both in $\mathcal{S}_0$ and in the prefactor. We also provide the conditions where the saddle point approximation to compute the vacuum decay of our model breaks down.

It might be of interest to obtain the result with the Feynman diagrammatic approach and also obtain the RGE running of parameters for this particular case.

The final expression for the FV decay rate in (5.61) consists of the semi-classical action $\mathcal{S}_0$ and the finite and renormalized corrections $\mathcal{S}_1$. Both are calculated for a complete range of parameters of the potential. The main results are summarized in fig. 5.2, where the behavior of the rate for thin and thick walls becomes apparent, as well as the range of validity of the simple approximations that were derived from the exact result. We also included the effects of the imaginary component of the complex field, which are found to be subdominant in general. Similarly to the SM which corresponds to the single quartic, the effect of fermions and gauge bosons could be taken into account. To this end, the known results [9, 182, 183], for spin $1/2$ and 1 fluctuations should be extended to include the second quartic segment while taking into account the presence of Dirac delta, in complete analogy to the imaginary complex scalar.

The present calculation relies on an exact bounce solution that can be found in $D = 4$. It may be of interest to extend its validity via dimensional continuation to other dimension, $D = 3$ in particular. This may be possible to do perturbatively, similarly to the bounce [83], near the thin wall, where the $1/\rho$ terms do not play a significant role. Likewise, one may consider other examples of exactly solvable bounce solutions such as the the log potential [118, 119], quadratic-quadratic [121], binomial [120] and (extended) polygonal [131]. The latter is particularly interesting because the fluctuation potential is smooth and avoids the delta function. At the same time, it can serve as a universal estimator of the total rate and might be extended to multi-fields [205], where only recently [179] progress was made.

Chapter 6

Concluding remarks

The decay of a false vacuum has been motivated by different contexts of physics. For instance, it can not only dynamically generate the observed dominance of matter over anti-matter and trigger phase transitions in the early universe, but it is also crucial for the calculation of the Higgs mass bound and the lifetime of our universe. In general, it allows us to obtain information about the unavoidable physics beyond the SM that takes place at energy scales well beyond the reach of any collider experiment. Nowadays, the motivation has been enhanced after the recent discovery of gravitational waves production and promising experiments such as LISA [63], DECIGO [64] and BBO [65, 66] that are scheduled to launch in over a decade.

In this work, we expanded the understanding of the false vacuum decay in three different aspects, both conceptual and practical. It includes a novel method to compute bounces in multifield potential, an user-friendly `Matematica` package and evaluations of sub-leading contributions in the prefactor with a closed-form result.

The method, called Polygonal bounce, provides an analytic insight into the multi-field phase transitions of the vacuum. It is a robust approach that avoids the usual purely numerical shooting method by the use of a collection of analytic solutions that approximate any potential up to desired precision. This makes the computation of the bounce stable, in particular in very thin-wall limit where purely numerical methods fail. We observed that it converge linearly with the number of fields and segments, which makes it fast and efficient to implement.

Then we released a `Mathematica` package called `FindBounce` that computes the bounce action with speed and precision around 2 seconds for 20 fields potential and within 1% accuracy. It is competitive with respect to other currently available programs with the Mathematica feel and look and contains a collection of basic examples, benchmarks, and timing. Its latest version can be downloaded from the repository, "release" on the web page `https://github.com/vguada/FindBounce/releases`. Its semi-analytic output can be exploited to obtain a semi-analytic prefactor and the subsequent evolution of the bubble. The package contains several applications, including the calculation of the nucleation temperature of a SM extension with a real scalar singlet.

In the end, we focused on the first quantum corrections of the vacuum decay rate. We learned that we must include these contributions to get a consistent and precise calculation of the bubble nucleation. We presented the first analytic complete result at one loop of the decay rate of a potential with two separate tree-level minima by the use of the bi-quartic potential. There, we showed that the calculation of the prefactor becomes non-perturbative for some range of parameters, in particular

when a large separation of scales is involved.

The above results have been fundamental in my current progress toward a general semi-analytic method to compute the pre-factor for any type of potential. The crucial point is that we showed how PB can provide analytic insight in the evaluation of the loop correction of the vacuum decay, as shown in appendix §C.2. Thus, it seems interesting to understand how this quantum fluctuation affects the gravitational waves spectrum in detail, in particular when there is a large separation of scales and loop correction are needed. Moreover, `FindBounce`, the Mathematica package, can be extended to compute gravitational waves for a large range of models beyond the SM as it is fast and practical to use. In particular, it could be interesting to focus on models BSM that has a rich vacuum structure such as Type II See Saw and compute the nucleation temperature and the gravitational waves signal. In short, I have been working on finding novel approaches to understand the decay of a false vacuum up to one-loop order, in heading towards gravitational waves and BSM physics.

Bibliography

[1] G. Aad *et al.* (ATLAS), *Observation of a new particle in the search for the Standard Model Higgs boson with the ATLAS detector at the LHC*, Phys. Lett. B **716**, 1 (2012).

[2] S. Chatrchyan *et al.* (CMS), *Observation of a New Boson at a Mass of 125 GeV with the CMS Experiment at the LHC*, Phys. Lett. B **716**, 30 (2012).

[3] S. Weinberg, *Mass of the Higgs Boson*, Phys. Rev. Lett. **36**, 294 (1976).

[4] A. D. Linde, *Dynamical Symmetry Restoration and Constraints on Masses and Coupling Constants in Gauge Theories*, JETP Lett. **23**, 64 (1976).

[5] P. Frampton, *Consequences of Vacuum Instability in Quantum Field Theory*, Phys. Rev. D **15**, 2922 (1977).

[6] G. Isidori, G. Ridolfi and A. Strumia, *On the metastability of the standard model vacuum*, Nucl. Phys. B **609**, 387 (2001).

[7] D. Buttazzo, G. Degrassi, P. P. Giardino, G. F. Giudice, F. Sala, A. Salvio and A. Strumia, *Investigating the near-criticality of the Higgs boson*, JHEP **12**, 089.

[8] A. Salvio, A. Strumia, N. Tetradis and A. Urbano, *On gravitational and thermal corrections to vacuum decay*, JHEP **09**, 054.

[9] A. Andreassen, W. Frost and M. D. Schwartz, *Scale Invariant Instantons and the Complete Lifetime of the Standard Model*, Phys. Rev. D **97**, 056006 (2018).

[10] S. Chigusa, T. Moroi and Y. Shoji, *Decay Rate of Electroweak Vacuum in the Standard Model and Beyond*, Phys. Rev. D **97**, 116012 (2018).

[11] P. Zyla *et al.* (Particle Data Group), *Review of Particle Physics*, PTEP **2020**, 083C01 (2020).

[12] V. Kuzmin, V. Rubakov and M. Shaposhnikov, *On the Anomalous Electroweak Baryon Number Nonconservation in the Early Universe*, Phys. Lett. B **155**, 36 (1985).

[13] M. Shaposhnikov, *Baryon Asymmetry of the Universe in Standard Electroweak Theory*, Nucl. Phys. B **287**, 757 (1987).

[14] A. Sakharov, *Violation of CP Invariance, C asymmetry, and baryon asymmetry of the universe*, Sov. Phys. Usp. **34**, 392 (1991).

[15] B. Garbrecht, *Why is there more matter than antimatter? Calculational methods for leptogenesis and electroweak baryogenesis*, Prog. Part. Nucl. Phys. **110**, 103727 (2020).

[16] J. E. Gunn and I. Gott, J. Richard, *On the Infall of Matter into Clusters of Galaxies and Some Effects on Their Evolution*, Astrophys. J. **176**, 1 (1972).

[17] J. Fillmore and P. Goldreich, *Self-similiar gravitational collapse in an expanding universe*, Astrophys. J. **281**, 1 (1984).

[18] E. Bertschinger, *Self - similar secondary infall and accretion in an Einstein-de Sitter universe*, Astrophys. J. Suppl. **58**, 39 (1985).

[19] J. F. Navarro, C. S. Frenk and S. D. White, *A Universal density profile from hierarchical clustering*, Astrophys. J. **490**, 493 (1997).

[20] A. Cooray and R. K. Sheth, *Halo Models of Large Scale Structure*, Phys. Rept. **372**, 1 (2002).

[21] S. Weinberg, *The Cosmological constant problems*, in *4th International Symposium on Sources and Detection of Dark Matter in the Universe (DM 2000)* (2000) pp. 18–26, arXiv:astro-ph/0005265 .

[22] D. H. Weinberg, M. J. Mortonson, D. J. Eisenstein, C. Hirata, A. G. Riess and E. Rozo, *Observational Probes of Cosmic Acceleration*, Phys. Rept. **530**, 87 (2013).

[23] S. Carroll and T. Company, *Dark Matter, Dark Energy: The Dark Side of the Universe*, Great courses (Teaching Company, LLC, 2007).

[24] Y. Fukuda *et al.* (Super-Kamiokande), *Evidence for oscillation of atmospheric neutrinos*, Phys. Rev. Lett. **81**, 1562 (1998).

[25] T. Araki *et al.* (KamLAND), *Measurement of neutrino oscillation with KamLAND: Evidence of spectral distortion*, Phys. Rev. Lett. **94**, 081801 (2005).

[26] A. D. Linde, *On the Vacuum Instability and the Higgs Meson Mass*, Phys. Lett. B **70**, 306 (1977).

[27] I. Affleck, *Quantum Statistical Metastability*, Phys. Rev. Lett. **46**, 388 (1981).

[28] A. D. Linde, *Fate of the False Vacuum at Finite Temperature: Theory and Applications*, Phys. Lett. B **100**, 37 (1981).

[29] A. D. Linde, *Decay of the False Vacuum at Finite Temperature*, Nucl. Phys. B **216**, 421 (1983), [Erratum: Nucl.Phys.B 223, 544 (1983)].

[30] S. Coleman, *Aspects of Symmetry: Selected Erice Lectures* (Cambridge University Press, Cambridge, U.K., 1985).

[31] E. Witten, *Cosmic Separation of Phases*, Phys. Rev. D **30**, 272 (1984).

[32] C. Hogan, *Gravitational radiation from cosmological phase transitions*, Mon. Not. Roy. Astron. Soc. **218**, 629 (1986).

[33] A. Kosowsky, M. S. Turner and R. Watkins, *Gravitational waves from first order cosmological phase transitions*, Phys. Rev. Lett. **69**, 2026 (1992).

[34] C. Grojean and G. Servant, *Gravitational Waves from Phase Transitions at the Electroweak Scale and Beyond*, Phys. Rev. D **75**, 043507 (2007).

[35] M. Hindmarsh, S. J. Huber, K. Rummukainen and D. J. Weir, *Gravitational waves from the sound of a first order phase transition*, Phys. Rev. Lett. **112**, 041301 (2014).

[36] D. Cutting, M. Hindmarsh and D. J. Weir, *Gravitational waves from vacuum first-order phase transitions: from the envelope to the lattice*, Phys. Rev. D **97**, 123513 (2018).

[37] C. Caprini and D. G. Figueroa, *Cosmological Backgrounds of Gravitational Waves*, Class. Quant. Grav. **35**, 163001 (2018).

[38] T. Vachaspati, *Magnetic fields from cosmological phase transitions*, Phys. Lett. B **265**, 258 (1991).

[39] G. Sigl, A. V. Olinto and K. Jedamzik, *Primordial magnetic fields from cosmological first order phase transitions*, Phys. Rev. D **55**, 4582 (1997).

[40] A. De Simone, G. Nardini, M. Quiros and A. Riotto, *Magnetic Fields at First Order Phase Transition: A Threat to Electroweak Baryogenesis*, JCAP **10**, 030.

[41] A. G. Tevzadze, L. Kisslinger, A. Brandenburg and T. Kahniashvili, *Magnetic Fields from QCD Phase Transitions*, Astrophys. J. **759**, 54 (2012).

[42] J. Ellis, M. Fairbairn, M. Lewicki, V. Vaskonen and A. Wickens, *Intergalactic Magnetic Fields from First-Order Phase Transitions*, JCAP **09**, 019.

[43] A. Bochkarev, S. Kuzmin and M. Shaposhnikov, *Electroweak baryogenesis and the Higgs boson mass problem*, Phys. Lett. B **244**, 275 (1990).

[44] A. G. Cohen, D. B. Kaplan and A. E. Nelson, *Weak scale baryogenesis*, Phys. Lett. B **245**, 561 (1990).

[45] N. Turok and J. Zadrozny, *Electroweak baryogenesis in the two doublet model*, Nucl. Phys. B **358**, 471 (1991).

[46] N. Turok and J. Zadrozny, *Dynamical generation of baryons at the electroweak transition*, Phys. Rev. Lett. **65**, 2331 (1990).

[47] M. Joyce, T. Prokopec and N. Turok, *Electroweak baryogenesis from a classical force*, Phys. Rev. Lett. **75**, 1695 (1995), [Erratum: Phys.Rev.Lett. 75, 3375 (1995)].

[48] M. Trodden, *Electroweak baryogenesis*, Rev. Mod. Phys. **71**, 1463 (1999).

[49] J. M. Cline, *Baryogenesis*, in *Les Houches Summer School - Session 86: Particle Physics and Cosmology: The Fabric of Spacetime* (2006) arXiv:hep-ph/0609145 .

[50] D. E. Morrissey and M. J. Ramsey-Musolf, *Electroweak baryogenesis*, New J. Phys. **14**, 125003 (2012).

[51] S. Khlebnikov, *Fluctuation - dissipation formula for bubble wall velocity*, Phys. Rev. D **46**, 3223 (1992).

[52] P. B. Arnold, *One loop fluctuation - dissipation formula for bubble wall velocity*, Phys. Rev. D **48**, 1539 (1993).

[53] G. D. Moore and T. Prokopec, *How fast can the wall move? A Study of the electroweak phase transition dynamics*, Phys. Rev. D **52**, 7182 (1995).

[54] P. John and M. Schmidt, *Do stops slow down electroweak bubble walls?*, Nucl. Phys. B **598**, 291 (2001), [Erratum: Nucl.Phys.B 648, 449–452 (2003)].

[55] J. M. No, *Large Gravitational Wave Background Signals in Electroweak Baryogenesis Scenarios*, Phys. Rev. D **84**, 124025 (2011).

[56] T. Konstandin, G. Nardini and I. Rues, *From Boltzmann equations to steady wall velocities*, JCAP **09**, 028.

[57] S. Höche, J. Kozaczuk, A. J. Long, J. Turner and Y. Wang, *Towards an all-orders calculation of the electroweak bubble wall velocity*, (2020).

[58] M. Barroso Mancha, T. Prokopec and B. Swiezewska, *Field theoretic derivation of bubble wall force*, (2020).

[59] F. Giese, T. Konstandin, K. Schmitz and J. van de Vis, *Model-independent energy budget for LISA*, (2020).

[60] B. Abbott *et al.* (LIGO Scientific, Virgo), *Observation of Gravitational Waves from a Binary Black Hole Merger*, Phys. Rev. Lett. **116**, 061102 (2016).

[61] J. Aasi *et al.* (LIGO Scientific), *Advanced LIGO*, Class. Quant. Grav. **32**, 074001 (2015).

[62] F. Acernese *et al.* (VIRGO), *Advanced Virgo: a second-generation interferometric gravitational wave detector*, Class. Quant. Grav. **32**, 024001 (2015).

[63] C. Caprini *et al.*, *Detecting gravitational waves from cosmological phase transitions with LISA: an update*, JCAP **03**, 024.

[64] S. Kawamura *et al.*, *The Japanese space gravitational wave antenna: DECIGO*, Class. Quant. Grav. **28**, 094011 (2011).

[65] J. Crowder and N. J. Cornish, *Beyond LISA: Exploring future gravitational wave missions*, Phys. Rev. D **72**, 083005 (2005).

[66] V. Corbin and N. J. Cornish, *Detecting the cosmic gravitational wave background with the big bang observer*, Class. Quant. Grav. **23**, 2435 (2006).

[67] I. Kobzarev, L. Okun and M. Voloshin, *Bubbles in Metastable Vacuum*, Sov. J. Nucl. Phys. **20**, 644 (1975).

[68] S. R. Coleman, *The Fate of the False Vacuum. 1. Semiclassical Theory*, Phys. Rev. D **15**, 2929 (1977), [Erratum: Phys.Rev.D 16, 1248 (1977)].

[69] J. Callan, Curtis G. and S. R. Coleman, *The Fate of the False Vacuum. 2. First Quantum Corrections*, Phys. Rev. D **16**, 1762 (1977).

[70] T. Guenault, *Basic Superfluids*, Master's Series in Physics and Astronomy (Taylor & Francis, 2002).

[71] G. Savvidy, *Infrared Instability of the Vacuum State of Gauge Theories and Asymptotic Freedom*, Phys. Lett. B **71**, 133 (1977).

[72] A. Andreassen, D. Farhi, W. Frost and M. D. Schwartz, *Precision decay rate calculations in quantum field theory*, Phys. Rev. D **95**, 085011 (2017).

[73] J. Espinosa, *A Fresh Look at the Calculation of Tunneling Actions*, JCAP **07**, 036.

[74] R. Jinno, *Machine learning for bounce calculation*, (2018).

[75] A. Andreassen, D. Farhi, W. Frost and M. D. Schwartz, *Direct Approach to Quantum Tunneling*, Phys. Rev. Lett. **117**, 231601 (2016).

[76] W.-Y. Ai, B. Garbrecht and C. Tamarit, *Functional methods for false vacuum decay in real time*, JHEP **12**, 095.

[77] M. P. Hertzberg and M. Yamada, *Vacuum Decay in Real Time and Imaginary Time Formalisms*, Phys. Rev. D **100**, 016011 (2019).

[78] J. Braden, M. C. Johnson, H. V. Peiris, A. Pontzen and S. Weinfurtner, *New Semiclassical Picture of Vacuum Decay*, Phys. Rev. Lett. **123**, 031601 (2019).

[79] A. Kusenko, *Improved action method for analyzing tunneling in quantum field theory*, Phys. Lett. B **358**, 51 (1995).

[80] P. John, *Bubble wall profiles with more than one scalar field: A Numerical approach*, Phys. Lett. B **452**, 221 (1999).

[81] J. M. Cline, G. D. Moore and G. Servant, *Was the electroweak phase transition preceded by a color broken phase?*, Phys. Rev. D **60**, 105035 (1999).

[82] C. L. Wainwright, *CosmoTransitions: Computing Cosmological Phase Transition Temperatures and Bubble Profiles with Multiple Fields*, Comput. Phys. Commun. **183**, 2006 (2012).

[83] T. Konstandin and S. J. Huber, *Numerical approach to multi dimensional phase transitions*, JCAP **06**, 021.

[84] J.-h. Park, *Constrained potential method for false vacuum decays*, JCAP **02**, 023.

[85] S. Akula, C. Balázs and G. A. White, *Semi-analytic techniques for calculating bubble wall profiles*, Eur. Phys. J. C **76**, 681 (2016).

[86] A. Masoumi, K. D. Olum and B. Shlaer, *Efficient numerical solution to vacuum decay with many fields*, JCAP **01**, 051.

[87] J. Espinosa and T. Konstandin, *A Fresh Look at the Calculation of Tunneling Actions in Multi-Field Potentials*, JCAP **01**, 051.

[88] P. Athron, C. Balázs, M. Bardsley, A. Fowlie, D. Harries and G. White, *BubbleProfiler: finding the field profile and action for cosmological phase transitions*, Comput. Phys. Commun. **244**, 448 (2019).

[89] M. L. Piscopo, M. Spannowsky and P. Waite, *Solving differential equations with neural networks: Applications to the calculation of cosmological phase transitions*, Phys. Rev. D **100**, 016002 (2019).

[90] S. Chigusa, T. Moroi and Y. Shoji, *Bounce Configuration from Gradient Flow*, Phys. Lett. B **800**, 135115 (2020).

[91] R. Sato, *Simple Gradient Flow Equation for the Bounce Solution*, Phys. Rev. D **101**, 016012 (2020).

[92] E. J. Weinberg, *Classical solutions in quantum field theory: Solitons and Instantons in High Energy Physics*, Cambridge Monographs on Mathematical Physics (Cambridge University Press, 2012).

[93] S. Weinberg, *The quantum theory of fields. Vol. 2: Modern applications* (Cambridge University Press, 2013).

[94] D. Croon, O. Gould, P. Schicho, T. V. Tenkanen and G. White, *Theoretical uncertainties for cosmological first-order phase transitions*, (2020).

[95] M. Peskin and D. Schroeder, *An Introduction To Quantum Field Theory*, Frontiers in Physics (Avalon Publishing, 1995).

[96] M. Srednicki, *Quantum Field Theory* (Cambridge University Press, 2007).

[97] A. Strumia and N. Tetradis, *A Consistent calculation of bubble nucleation rates*, Nucl. Phys. B **542**, 719 (1999).

[98] J. Baacke and G. Lavrelashvili, *One loop corrections to the metastable vacuum decay*, Phys. Rev. D **69**, 025009 (2004).

[99] G. V. Dunne and H. Min, *Beyond the thin-wall approximation: Precise numerical computation of prefactors in false vacuum decay*, Phys. Rev. D **72**, 125004 (2005).

[100] G. V. Dunne and K. Kirsten, *Functional determinants for radial operators*, J. Phys. A **39**, 11915 (2006).

[101] K. Kirsten and P. Loya, *Computation of determinants using contour integrals*, Am. J. Phys. **76**, 60 (2008).

[102] R. Konoplich, *Calculation of Quantum Corrections to Nontrivial Classical Solutions by Means of the Zeta Function*, Theor. Math. Phys. **73**, 1286 (1987).

[103] G. Munster and S. Rotsch, *Analytical calculation of the nucleation rate for first order phase transitions beyond the thin wall approximation*, Eur. Phys. J. C **12**, 161 (2000).

[104] A. Wipf, *Tunnel Determinants*, Nucl. Phys. B **269**, 24 (1986).

[105] B. Garbrecht and P. Millington, *Fluctuations about the Fubini-Lipatov instanton for false vacuum decay in classically scale invariant models*, Phys. Rev. D **98**, 016001 (2018).

[106] N. Froman, N. Fröman and P. Fröman, *JWKB Approximation: Contributions to the Theory* (North-Holland Publishing Company; [sole distributors for U.S.A.: Interscience Publishers, New York], 1965).

[107] L. Landau and E. Lifshitz, *Quantum Mechanics: Non-Relativistic Theory*, Course of Theoretical Physics (Elsevier Science, 1981).

[108] D. Griffiths and P. Griffiths, *Introduction to Quantum Mechanics*, Pearson international edition (Pearson Prentice Hall, 2005).

[109] R. Feynman, A. Hibbs and D. Styer, *Quantum Mechanics and Path Integrals*, Dover Books on Physics (Dover Publications, 2010).

[110] H. Kleinert, *Path Integrals in Quantum Mechanics, Statistics, Polymer Physics, and Financial Markets*, EBL-Schweitzer (World Scientific, 2009).

[111] S. R. Coleman, V. Glaser and A. Martin, *Action Minima Among Solutions to a Class of Euclidean Scalar Field Equations*, Commun. Math. Phys. **58**, 211 (1978).

[112] K. Blum, M. Honda, R. Sato, M. Takimoto and K. Tobioka, *O(N) Invariance of the Multi-Field Bounce*, JHEP **05**, 109, [Erratum: JHEP 06, 060 (2017)].

[113] G. Derrick, *Comments on nonlinear wave equations as models for elementary particles*, J. Math. Phys. **5**, 1252 (1964).

[114] S. Fubini, *A New Approach to Conformal Invariant Field Theories*, Nuovo Cim. A **34**, 521 (1976).

[115] L. Lipatov, *Divergence of the Perturbation Theory Series and the Quasiclassical Theory*, Sov. Phys. JETP **45**, 216 (1977).

[116] F. Loran, *Fubini vacua as a classical de Sitter vacua*, Mod. Phys. Lett. A **22**, 2217 (2007).

[117] K.-M. Lee and E. J. Weinberg, *Tunneling without barriers*, Nucl. Phys. B **267**, 181 (1986).

[118] T. Shen, *Bubbles without cores*, Phys. Rev. D **37**, 3537 (1988).

[119] A. Ferraz de Camargo, R. Shellard and G. Marques, *Vacuum Decay in a Soluble Model*, Phys. Rev. D **29**, 1147 (1984).

[120] A. Aravind, B. S. DiNunno, D. Lorshbough and S. Paban, *Analyzing multifield tunneling with exact bounce solutions*, Phys. Rev. D **91**, 025026 (2015).

[121] G. Pastras, *Exact Tunneling Solutions in Minkowski Spacetime and a Candidate for Dark Energy*, JHEP **08**, 075.

[122] M. J. Duncan and L. G. Jensen, *Exact tunneling solutions in scalar field theory*, Phys. Lett. B **291**, 109 (1992).

[123] K. Dutta, C. Hector, P. M. Vaudrevange and A. Westphal, *More Exact Tunneling Solutions in Scalar Field Theory*, Phys. Lett. B **708**, 309 (2012).

[124] K. Dutta, C. Hector, T. Konstandin, P. M. Vaudrevange and A. Westphal, *Validity of the kink approximation to the tunneling action*, Phys. Rev. D **86**, 123517 (2012).

[125] A. Masoumi, K. D. Olum and J. M. Wachter, *Approximating tunneling rates in multi-dimensional field spaces*, JCAP **10**, 022.

[126] L. Darmé, J. Jaeckel and M. Lewicki, *Towards the fate of the oscillating false vacuum*, Phys. Rev. D **96**, 056001 (2017).

[127] S. Sarangi, G. Shiu and B. Shlaer, *Rapid Tunneling and Percolation in the Landscape*, Int. J. Mod. Phys. A **24**, 741 (2009).

[128] P. M. Saffin, A. Padilla and E. J. Copeland, *Decay of an inhomogeneous state via resonant tunnelling*, JHEP **09**, 055.

[129] S.-H. Tye and D. Wohns, *Resonant Tunneling in Scalar Quantum Field Theory*, (2009).

[130] L. Darmé, J. Jaeckel and M. Lewicki, *Generalized escape paths for dynamical tunneling in QFT*, Phys. Rev. D **100**, 096012 (2019).

[131] V. Guada, A. Maiezza and M. Nemevšek, *Multifield Polygonal Bounces*, Phys. Rev. D **99**, 056020 (2019).

[132] U. Sarid, *Tools for tunneling*, Phys. Rev. D **58**, 085017 (1998).

[133] S. R. Coleman and F. De Luccia, *Gravitational Effects on and of Vacuum Decay*, Phys. Rev. D **21**, 3305 (1980).

[134] G. Isidori, V. S. Rychkov, A. Strumia and N. Tetradis, *Gravitational corrections to standard model vacuum decay*, Phys. Rev. D **77**, 025034 (2008).

[135] M. Claudson, L. J. Hall and I. Hinchliffe, *Low-Energy Supergravity: False Vacua and Vacuous Predictions*, Nucl. Phys. B **228**, 501 (1983).

[136] J. Moreno, M. Quiros and M. Seco, *Bubbles in the supersymmetric standard model*, Nucl. Phys. B **526**, 489 (1998).

[137] S. J. Huber, T. Konstandin, T. Prokopec and M. G. Schmidt, *Electroweak Phase Transition and Baryogenesis in the nMSSM*, Nucl. Phys. B **757**, 172 (2006).

[138] M. C. Johnson and M. Larfors, *Field dynamics and tunneling in a flux landscape*, Phys. Rev. D **78**, 083534 (2008).

[139] B. Greene, D. Kagan, A. Masoumi, D. Mehta, E. J. Weinberg and X. Xiao, *Tumbling through a landscape: Evidence of instabilities in high-dimensional moduli spaces*, Phys. Rev. D **88**, 026005 (2013).

[140] M. Dine and S. Paban, *Tunneling in Theories with Many Fields*, JHEP **10**, 088.

[141] V. Guada, M. Nemevšek and M. Pintar, *FindBounce: package for multi-field bounce actions*, Comput. Phys. Commun. **256**, 107480 (2020).

[142] P. W. Graham, D. E. Kaplan and S. Rajendran, *Cosmological Relaxation of the Electroweak Scale*, Phys. Rev. Lett. **115**, 221801 (2015).

[143] J. Espinosa, C. Grojean, G. Panico, A. Pomarol, O. Pujolàs and G. Servant, *Cosmological Higgs-Axion Interplay for a Naturally Small Electroweak Scale*, Phys. Rev. Lett. **115**, 251803 (2015).

[144] E. Hardy, *Electroweak relaxation from finite temperature*, JHEP **11**, 077.

[145] S. P. Patil and P. Schwaller, *Relaxing the Electroweak Scale: the Role of Broken dS Symmetry*, JHEP **02**, 077.

[146] J. Jaeckel, V. M. Mehta and L. T. Witkowski, *Musings on cosmological relaxation and the hierarchy problem*, Phys. Rev. D **93**, 063522 (2016).

[147] R. S. Gupta, Z. Komargodski, G. Perez and L. Ubaldi, *Is the Relaxion an Axion?*, JHEP **02**, 166.

[148] B. Batell, G. F. Giudice and M. McCullough, *Natural Heavy Supersymmetry*, JHEP **12**, 162.

[149] J. Jaeckel, V. M. Mehta and L. T. Witkowski, *Monodromy Dark Matter*, JCAP **01**, 036.

[150] N. Fonseca, E. Morgante, R. Sato and G. Servant, *Relaxion Fluctuations (Self-stopping Relaxion) and Overview of Relaxion Stopping Mechanisms*, JHEP **05**, 080.

[151] A. R. Brown and A. Dahlen, *The Case of the Disappearing Instanton*, Phys. Rev. D **84**, 105004 (2011).

[152] G. Degrassi, S. Di Vita, J. Elias-Miro, J. R. Espinosa, G. F. Giudice, G. Isidori and A. Strumia, *Higgs mass and vacuum stability in the Standard Model at NNLO*, JHEP **08**, 098.

[153] S. Chigusa, T. Moroi and Y. Shoji, *State-of-the-Art Calculation of the Decay Rate of Electroweak Vacuum in the Standard Model*, Phys. Rev. Lett. **119**, 211801 (2017).

[154] J. Espinosa, *Tunneling without Bounce*, Phys. Rev. D **100**, 105002 (2019).

[155] G. Branco, P. Ferreira, L. Lavoura, M. Rebelo, M. Sher and J. P. Silva, *Theory and phenomenology of two-Higgs-doublet models*, Phys. Rept. **516**, 1 (2012).

[156] S. Huber and M. Schmidt, *Electroweak baryogenesis: Concrete in a SUSY model with a gauge singlet*, Nucl. Phys. B **606**, 183 (2001).

[157] H. H. Patel and M. J. Ramsey-Musolf, *Baryon Washout, Electroweak Phase Transition, and Perturbation Theory*, JHEP **07**, 029.

[158] J. M. Cline and K. Kainulainen, *Electroweak baryogenesis and dark matter from a singlet Higgs*, JCAP **01**, 012.

[159] M. Chala, G. Nardini and I. Sobolev, *Unified explanation for dark matter and electroweak baryogenesis with direct detection and gravitational wave signatures*, Phys. Rev. D **94**, 055006 (2016).

[160] C. Burgess, M. Pospelov and T. ter Veldhuis, *The Minimal model of nonbaryonic dark matter: A Singlet scalar*, Nucl. Phys. B **619**, 709 (2001).

[161] J. McDonald, *Thermally generated gauge singlet scalars as selfinteracting dark matter*, Phys. Rev. Lett. **88**, 091304 (2002).

[162] M. Gonderinger, Y. Li, H. Patel and M. J. Ramsey-Musolf, *Vacuum Stability, Perturbativity, and Scalar Singlet Dark Matter*, JHEP **01**, 053.

[163] J. M. Cline, K. Kainulainen, P. Scott and C. Weniger, *Update on scalar singlet dark matter*, Phys. Rev. D **88**, 055025 (2013), [Erratum: Phys.Rev.D 92, 039906 (2015)].

[164] C. Caprini, R. Durrer and G. Servant, *The stochastic gravitational wave background from turbulence and magnetic fields generated by a first-order phase transition*, JCAP **12**, 024.

[165] J. R. Espinosa, T. Konstandin, J. M. No and G. Servant, *Energy Budget of Cosmological First-order Phase Transitions*, JCAP **06**, 028.

[166] P. Binetruy, A. Bohe, C. Caprini and J.-F. Dufaux, *Cosmological Backgrounds of Gravitational Waves and eLISA/NGO: Phase Transitions, Cosmic Strings and Other Sources*, JCAP **06**, 027.

[167] E. Thrane and J. D. Romano, *Sensitivity curves for searches for gravitational-wave backgrounds*, Phys. Rev. D **88**, 124032 (2013).

[168] J. Ellis, M. Lewicki, J. M. No and V. Vaskonen, *Gravitational wave energy budget in strongly supercooled phase transitions*, JCAP **06**, 024.

[169] L. Dolan and R. Jackiw, *Symmetry Behavior at Finite Temperature*, Phys. Rev. D **9**, 3320 (1974).

[170] S. Weinberg, *Gauge and Global Symmetries at High Temperature*, Phys. Rev. D **9**, 3357 (1974).

[171] M. Quiros, *Finite temperature field theory and phase transitions*, in *ICTP Summer School in High-Energy Physics and Cosmology* (1999) pp. 187–259, arXiv:hep-ph/9901312 .

[172] J. Kapusta and C. Gale, *Finite-temperature field theory: Principles and applications*, Cambridge Monographs on Mathematical Physics (Cambridge University Press, 2011).

[173] A. Fowlie, *A fast C++ implementation of thermal functions*, Comput. Phys. Commun. **228**, 264 (2018).

[174] J. R. Espinosa, T. Konstandin and F. Riva, *Strong Electroweak Phase Transitions in the Standard Model with a Singlet*, Nucl. Phys. B **854**, 592 (2012).

[175] G. W. Anderson and L. J. Hall, *The Electroweak phase transition and baryogenesis*, Phys. Rev. D **45**, 2685 (1992).

[176] J. Camargo-Molina, B. O'Leary, W. Porod and F. Staub, **Vevacious***: A Tool For Finding The Global Minima Of One-Loop Effective Potentials With Many Scalars*, Eur. Phys. J. C **73**, 2588 (2013).

[177] R. Sato, *SimpleBounce : a simple package for the false vacuum decay*, (2019).

[178] J. Hur and H. Min, *A Fast Way to Compute Functional Determinants of Radially Symmetric Partial Differential Operators in General Dimensions*, Phys. Rev. D **77**, 125033 (2008).

[179] S. Chigusa, T. Moroi and Y. Shoji, *Precise Calculation of the Decay Rate of False Vacuum with Multi-Field Bounce*, (2020).

[180] B. Garbrecht and P. Millington, *Green's function method for handling radiative effects on false vacuum decay*, Phys. Rev. D **91**, 105021 (2015).

[181] W.-Y. Ai, B. Garbrecht and P. Millington, *Radiative effects on false vacuum decay in Higgs-Yukawa theory*, Phys. Rev. D **98**, 076014 (2018).

[182] M. Endo, T. Moroi, M. M. Nojiri and Y. Shoji, *On the Gauge Invariance of the Decay Rate of False Vacuum*, Phys. Lett. B **771**, 281 (2017).

[183] M. Endo, T. Moroi, M. M. Nojiri and Y. Shoji, *False Vacuum Decay in Gauge Theory*, JHEP **11**, 074.

[184] V. Guada and M. Nemevšek, *Exact one-loop false vacuum decay rate*, Phys. Rev. D **102**, 125017 (2020).

[185] C. Hammer, J. Shrauner and B. DeFacio, *Alternate Derivation of Vacuum Tunneling*, Phys. Rev. D **19**, 667 (1979).

[186] S. R. Coleman, *The Uses of Instantons*, Subnucl. Ser. **15**, 805 (1979).

[187] S. R. Coleman, *Quantum Tunneling and Negative Eigenvalues*, Nucl. Phys. B **298**, 178 (1988).

[188] A. Kusenko, *Tunneling in quantum field theory with spontaneous symmetry breaking*, Phys. Lett. B **358**, 47 (1995).

[189] A. Kusenko, K.-M. Lee and E. J. Weinberg, *Vacuum decay and internal symmetries*, Phys. Rev. D **55**, 4903 (1997).

[190] J.-L. Gervais and B. Sakita, *Extended Particles in Quantum Field Theories*, Phys. Rev. D **11**, 2943 (1975).

[191] J.-L. Gervais, A. Jevicki and B. Sakita, *Perturbation Expansion Around Extended Particle States in Quantum Field Theory. 1.*, Phys. Rev. D **12**, 1038 (1975).

[192] J. Callan, Curtis G. and D. J. Gross, *Quantum Perturbation Theory of Solitons*, Nucl. Phys. B **93**, 29 (1975).

[193] A. Jevicki, *Treatment of Zero Frequency Modes in Perturbation Expansion About Classical Field Configurations*, Nucl. Phys. B **117**, 365 (1976).

[194] I. Gelfand and A. Yaglom, *Integration in functional spaces and it applications in quantum physics*, J. Math. Phys. **1**, 48 (1960).

[195] S. Oda, Y. Shoji and D.-S. Takahashi, *High Scale Validity of the DFSZ Axion Model with Precision*, JHEP **03**, 011.

[196] S. Minakshisundaram and A. Pleijel, *Some properties of the eigenfunctions of the Laplace operator on Riemannian manifolds*, Can. J. Math. **1**, 242 (1949).

[197] S. Hawking, *Zeta Function Regularization of Path Integrals in Curved Space-Time*, Commun. Math. Phys. **55**, 133 (1977).

[198] E. Elizalde, S. Odintsov, A. Romeo, A. Bytsenko and S. Zerbini, *Zeta regularization techniques with applications* (1994).

[199] K. Kirsten, *Spectral functions in mathematics and physics*, AIP Conf. Proc. **484**, 106 (1999).

[200] K. Kirsten, *Spectral functions in mathematics and physics* (2001).

[201] G. V. Dunne, *Functional determinants in quantum field theory*, J. Phys. A **41**, 304006 (2008).

[202] K. Kirsten and A. J. McKane, *Functional determinants by contour integration methods*, Annals Phys. **308**, 502 (2003).

[203] K. Kirsten and A. J. McKane, *Functional determinants in the presence of zero modes*, in *6th Workshop on Quantum Field Theory under the Influence of External Conditions (QFEXT03)* (2005) pp. 146–151, arXiv:hep-th/0507005 .

[204] H. Weyl., *Das asymptotische Verteilungsgesetz der Eigenwerte linearer partieller Differentialgleichungen (mit einer Anwendung auf die Theorie der Hohlraumstrahlung)*, Annals Math. **71**, 441 (1912).

[205] V. Guada, A. Ivanov, M. Nemevšek and L. Ubaldi, *work in progress*, (2021).

[206] S. R. Coleman and E. J. Weinberg, *Radiative Corrections as the Origin of Spontaneous Symmetry Breaking*, Phys. Rev. D **7**, 1888 (1973).

[207] R. Jackiw, *Functional evaluation of the effective potential*, Phys. Rev. D **9**, 1686 (1974).

[208] J. Iliopoulos, C. Itzykson and A. Martin, *Functional Methods and Perturbation Theory*, Rev. Mod. Phys. **47**, 165 (1975).

[209] A. Andreassen, W. Frost and M. D. Schwartz, *Consistent Use of Effective Potentials*, Phys. Rev. D **91**, 016009 (2015).

[210] M. Abramowitz and I. Stegun, *Handbook of Mathematical Functions: With Formulas, Graphs, and Mathematical Tables*, Applied mathematics series (Dover Publications, 1965).

[211] E. Elizalde, *An Asymptotic Expansion for the First Derivative of the Generalized Riemann Zeta Function*, Mathematics of Computation **47**, 347 (1986).

Appendix A

Appendix to Chapter 2

A.1 On $D = 2, 6, 8$ dimensions

Here we complete the treatment of the polygonal bounce construction for dimensions other than $D = 3, 4$, starting with the special instance of $D = 2$. The field solution is

$$\varphi_s(\rho) = v_s + 2a_s\rho^2 - b_s \ln \rho^2. \tag{A.1}$$

The b_1 expression in (3.4) remains the same, while v_1 is obtained from (3.4) by replacing

$$\frac{4}{D-2} R_s^2 \xrightarrow{D\to 2} 2R_s^2 \left(1 - \ln R_s^2\right). \tag{A.2}$$

Likewise, the expression for the final condition of b_{N-1} in (3.5) remains the same, and the same replacement of (A.2) should be used to obtain v_{N-1}. The resulting action is

$$\begin{aligned} \mathcal{S}_0^{D=2} =& \pi R_0^2 \left(\tilde{V}_1 - \tilde{V}_N\right) + 2\pi \sum_{s=1}^{N-1} \Bigg[6a_s^2\rho^4 + b_s^2 \ln(\rho^2) + \\ & \frac{\rho^2}{2} \left(8a_s(v_s - \tilde{\varphi}_s) + \tilde{V}_s - \tilde{V}_N - 8a_s b_s \ln(\rho^2)\right) \Bigg]_{R_{s-1}}^{R_s}, \end{aligned} \tag{A.3}$$

The matching conditions for $D = 2$ are slightly different

$$v_s + 2a_s R_s^2 - b_s \ln R_s^2 = \tilde{\varphi}_{s+1}, \tag{A.4}$$

$$v_{s+1} + 2a_{s+1} R_s^2 - b_{s+1} \ln R_s^2 = \tilde{\varphi}_{s+1}, \tag{A.5}$$

$$2\left(a_{s+1} - a_s\right) R_s^2 + b_s - b_{s+1} = 0, \tag{A.6}$$

and the recursion relations in (3.7) are modified by applying the replacement of (A.2) to v_s. The radii in two dimensions are solved by

$$R_s^2 = -\frac{b_s}{2a_s} W\left(-2\frac{a_s}{b_s} \exp\left(\frac{v_s - \tilde{\varphi}_{s+1}}{b_s}\right)\right), \tag{A.7}$$

where $W(z)$ is the product log function that returns the solution of w to the equation $z = w\, e^w$ for a given z.

The polygonal bounce setup for $D = 6, 8$ closely follows the procedure outlined in section §3.2 above, apart from the solution of the radii fewnomial in (3.8). Indeed, the two closed form solutions for $D = 6, 8$ are

$$\begin{aligned} D=6: \quad 2R_s^2 &= \frac{\delta_s}{a_s} + \left(\frac{\delta_s}{a_s}\right)^2 \frac{1}{\zeta} + \zeta, \\ \zeta^3 &= \sqrt{3}\sqrt{3\left(\frac{b_s}{a_s}\right)^2 - 2\left(\frac{\delta_s}{a_s}\right)^3 \frac{b_s}{a_s}} + \left(\frac{\delta_s}{a_s}\right)^3 - 3\frac{b_s}{a_s}, \end{aligned} \tag{A.8}$$

$$\begin{aligned} D=8: \quad 2R_s^2 &= \frac{\delta_s}{a_s} - \chi_1 - \sqrt{2\left(\frac{\delta_s}{a_s}\right)^2 - \frac{2\delta_s^3}{a_s^3\chi_1} - \frac{\sqrt[3]{2}}{3}\frac{4b_s + \sqrt[3]{2}a_s\chi_0^2}{a_s\chi_0}}, \\ \chi_1^2 &= \left(\frac{\delta_s}{a_s}\right)^2 + \frac{4\sqrt[3]{2}}{3}\frac{b_s}{a_s\chi_0} + \frac{\sqrt[3]{4}}{3}\chi_0, \\ \chi_0^3 &= \sqrt{81\left(\frac{\delta_s}{a_s}\right)^4\left(\frac{b_s}{a_s}\right)^2 - 32\left(\frac{b_s}{a_s}\right)^3} + 9\left(\frac{\delta_s}{a_s}\right)^2\frac{b_s}{a_s}. \end{aligned} \tag{A.9}$$

A.2 Multi-field $N = 3$ in D dimensions

The minimal multi-field case with $N = 3$ can be carried out analytically up to a single n_f^2 linear system. The initial conditions in (3.47) and (3.48) with recursion relations (3.43) and (3.44) give

$$v_{i2} = -\frac{4}{D-2}\big((a_{i1} + 2\bar{a}_{i1}r_{i0})\,R_0^2 + (a_{i2} - a_{i1})\,R_1^2\big) - \frac{1}{D-2}\,(\dot{\tilde{\varphi}}_{i2} - \dot{\tilde{\varphi}}_{i1})\,R_1, \tag{A.10}$$

$$b_{i2} = \frac{4}{D}\big((a_{i1} + D\bar{a}_{i1}r_{i0})\,R_0^D + (a_{i2} - a_{i1})\,R_1^D\big) + \frac{1}{2}\,(\dot{\tilde{\varphi}}_{i2} - \dot{\tilde{\varphi}}_{i1})\,R_1^{D-1}. \tag{A.11}$$

This leaves us with three equations for r_{i0}, r_{i2} and $\tilde{\zeta}_{i2}$

$$r_{i0} = \left(\frac{D-2}{8}R_1^{D-2}\tilde{\zeta}_{i2} - a_{i1}\big(\frac{D-2}{2D}R_1^D - \frac{R_0^2R_1^{D-2}}{2} + DR_0^D\big)\right)\frac{\big(R_0^D - R_0^2R_1^{D-2}\big)}{\bar{a}_{i1}}, \tag{A.12}$$

$$v_{i2} + \frac{2}{D-2}\frac{b_{i2}}{R_2^{D-2}} + \frac{4}{D}a_{i2}R_2^2 = 0, \tag{A.13}$$

$$r_{i2} = \frac{1}{\bar{a}_{i2}}\left(\frac{b_{i2}}{4R_2^D} - \frac{a_{i2}}{D}\right), \tag{A.14}$$

Inserting r_{i0} from (A.12) into (A.13) gives a linear system for $\tilde{\zeta}_{i2}$ that can be solved using the explicit form of $a_{i1,2}(\tilde{\zeta}_{i2})$ given in (3.41). Once $\tilde{\zeta}_{i2}$ is given, r_{i2} follows from (A.14), which concludes the calculation of ζ.

Remarkably, this simple estimate already gives a rather good approximation for the path in field space, the main inaccuracy in the bounce action is due to the poor estimate of the ρ dependence.

A.3 Real radii and root finding

Real radii. The radii solutions in Eqs. (A.7)-(A.9), as well as those in (3.9),(3.10) above, allow for a number of branches. The ones chosen above are such that the

resulting R_s are real and positive. Moreover, the slope of the potential a_s has to be appropriately factorized in the expressions above in order to maintain the reality of R_s during the transition through the maximum of V when a_s flips the sign. This choice of signs also ensures that the radii of segments below the initial φ_0 automatically remain 0, i.e. $R_s = 0$ for $\tilde{\varphi}_s < \varphi_0$.

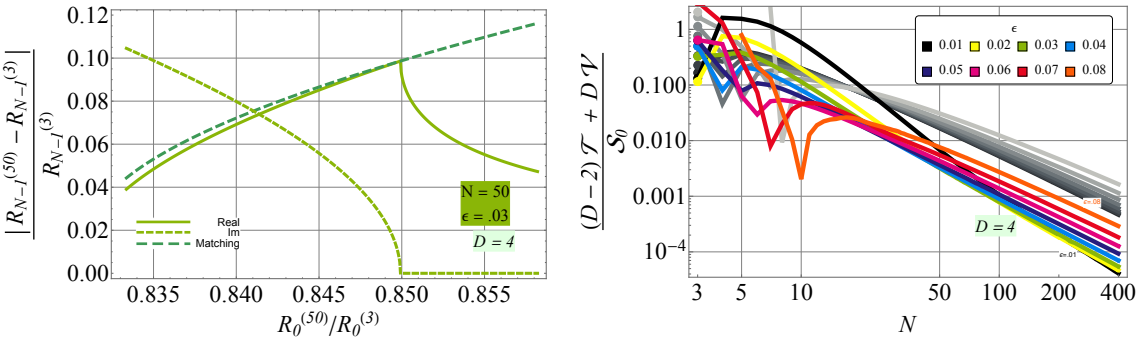

Figure A.1: Left: The final radius dependence on R_0 for $N = 50$ and $\varepsilon = 0.03$, showing the real and imaginary part, as well as the corresponding value obtained from R_{N-1} in the matching condition in (3.15). Right: The continuous version of Derrick's theorem (2.27) with $\mathcal{T}$ computed with the PB and $\mathcal{V}$ from the input potential in (3.18). The normalized quantity acts as a test of convergence and goodness of approximation.

Root finding. The starting point for root finding is to determine the real domains of the initial parameters φ_0 and R_0 for a) and b) cases, respectively. This defines the region of parameter space where a consistent solution can be searched for. To illustrate this point, we show the behavior of the final radius with respect to R_0 and φ_0 in fig. A.1. It is curious that the solution to the matching equation in (3.15) lies precisely on the edge of the real domain.

In order to implement the root searching numerically, one has to define a starting estimate for R_0 or φ_0. It turns out that for case a) the more stable option is to choose the initial estimate for φ_0 close to the false vacuum $\varphi_0 \simeq \tilde{\varphi}_1$, while in the case b) the $N = 3$ result gives a fairly reliable starting point. Moreover, the behavior of case b) root finding convergence is in general more stable with respect to case a).

The behavior of φ_0 that solves the polygonal bounce in case a), is shown on the left of fig. A.2, where the field is normalized to the position of the false minimum in $\tilde{\varphi}_1$. Notice that as ε decreases, the solution gets closer to $\tilde{\varphi}_1$ and eventually crosses over to case b). The smaller N approximation typically underestimates the final value and oscillates towards the limiting value, which is an artefact of the segmentation.

Note also that for $\varepsilon = 0.05(0.04)$, the solution for case a) does not exist until $N \gtrsim 10(70)$ when the segmentation becomes refined enough for the method to work and which is precisely when R_0 becomes non-zero in fig. 3.3. Another particularity related to the segmentation happens with $\varepsilon = 0.07$ in $D = 4$ where we start in case a) for $N = 3, 4$, switch to case b) and return back to a) at $N = 8$.

The right panel of fig. A.2 shows the extent of the non-trivial part of the bounce field solution in the ρ dimension, i.e. the final radius R_{N-1}, normalized to the $N = 3$ approximation. Above this radius, the bounce solution remains constant as

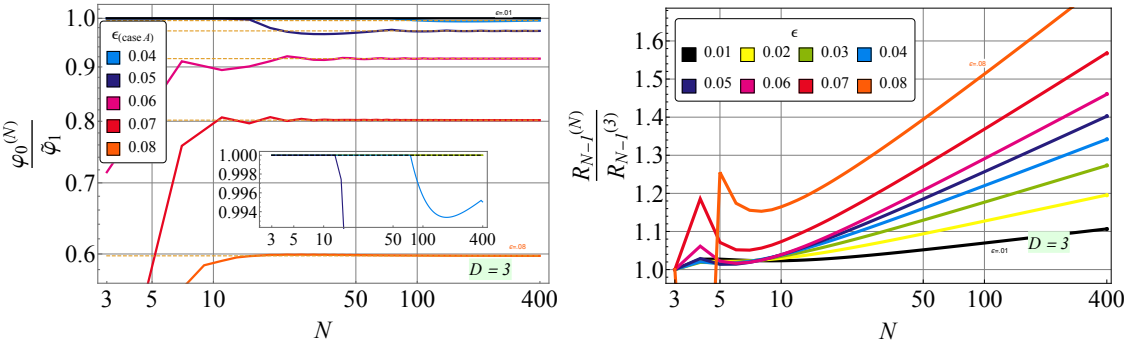

Figure A.2: Left: The initial field value φ_0 normalized to the position of the false minimum in $\tilde{\varphi}_1$. Right: The final radius R_{N-1}, normalized to the $N = 3$ approximation.

in fig. 3.1. As we expect to get back to (3.35) in the continuous limit, the R_{N-1} should go to infinity when N increases, which is evident from the right panel of fig. A.2.

As discussed above, the R_{N-1} is a finite and numerically well defined quantity that regulates the infinity of ρ. In particular, the extent to which the final radius grows is surprisingly small. Even for a large number of points $N \sim 400$ where the bounce action is already quite precise, the final radius is merely about 50% larger than the initial estimate from $N = 3$.

Appendix B

Appendix to Chapter 3

B.1 One-Loop effective potential

The calculation of the effective potential was first computed by Coleman and Weinberg [206] at one-loop and at higher loops by Jackiw and Iliopoulus, et al. [207, 208] at zero temperature. For finite temperatures excellent references are [169, 170], a review [171] and the textbook [172] For recent works on the consistent use of potentials, see [209]. The quantum and thermal results at one-loop order in the $\overline{\text{MS}}$ scheme are:

$$\text{Quantum: } \Delta V_1(\varphi) = \sum_i \pm \frac{n_i m_i^4(\varphi)}{64\pi^2}\left(\ln\frac{m_i^2(\varphi)}{\mu_R^2} - C_i\right), \tag{B.1}$$

$$\text{Thermal: } \Delta V_1(\varphi, T) = \sum_i \frac{n_i T^4}{2\pi^2} J_{B/F}\left(\frac{m_i^2(\varphi)}{T^2}\right), \tag{B.2}$$

where μ_R is the renormalization scale and $C_i = 3/2\,(5/6)$ for scalars and fermions (gauge bosons). The sum runs over all the species that couple to φ, where n_i and $m_i^2(\varphi)$ are the number of degrees of freedom and the field-dependent squared masses of the species i. The upper and lower sign corresponds to bosons (B) and fermions (F), respectively. The relevant thermal functions are given by

$$J_{B/F}\left(y^2\right) = \mp \int_0^\infty \mathrm{d}x\, x^2 \ln\left(1 \pm e^{-\sqrt{x^2+y^2}}\right), \tag{B.3}$$

and can be expanded at high temperatures, ($y^2 \ll 1$) such that

$$J_B(y^2) = -\frac{7\pi}{360} + \frac{\pi^2}{24}y^2 + \frac{y^4}{32}\ln\frac{y^2}{a} + \mathcal{O}\left(y^6\right), \tag{B.4}$$

$$J_F(y^2) = -\frac{\pi^6}{45} + \frac{\pi^2}{12}y^2 - \frac{\pi}{6}\left(y^2\right)^{\frac{3}{2}} - \frac{y^4}{32}\ln\frac{y^2}{16a} + \mathcal{O}\left(y^6\right), \tag{B.5}$$

with $a = \pi^2 e^{\frac{3}{2}-2\gamma_E}$.

B.2 Multi field potential parameters

The multi-field potential for comparison with other packages, shown in table 4.1, was taken from [80] and defined for each number of fields n_φ as

$$V(\varphi) = \frac{1}{10}\left(\varphi^4 - 8\varphi^3 + 10\varphi^2 + 8\right), \tag{B.6}$$

n_φ	c_i
3	0.68, 0.18, 0.30, 0.28
4	0.53, 0.77, 0.84, 0.01, 0.26
5	0.47, 0.23, 0.57, 0.14, 0.52, 0.66
6	0.34, 0.47, 0.23, 0.57, 0.14, 0.52, 0.66
7	0.52, 0.34, 0.47, 0.23, 0.57, 0.14, 0.52, 0.66
8	0.24, 0.52, 0.34, 0.47, 0.23, 0.57, 0.14, 0.52, 0.66
9	0.21, 0.24, 0.52, 0.34, 0.47, 0.23, 0.57, 0.14, 0.52, 0.66
10	0.12, 0.21, 0.24, 0.52, 0.34, 0.47, 0.23, 0.57, 0.14, 0.52, 0.66
11	0.23, 0.21, 0.21, 0.24, 0.52, 0.34, 0.47, 0.23, 0.57, 0.14, 0.52, 0.66
12	0.12, 0.11, 0.12, 0.21, 0.24, 0.52, 0.34, 0.47, 0.23, 0.57, 0.14, 0.52, 0.66
13	0.54, 0.47, 0.53, 0.28, 0.35, 0.27, 0.42, 0.59, 0.33, 0.16, 0.38, 0.35, 0.17, 0.41
14	0.39, 0.23, 0.26, 0.40, 0.11, 0.42, 0.41, 0.27, 0.42, 0.54, 0.18, 0.59, 0.13, 0.29, 0.58
15	0.21, 0.22, 0.22, 0.23, 0.39, 0.55, 0.43, 0.12, 0.16, 0.58, 0.25, 0.50, 0.45, 0.35, 0.45, 0.12
16	0.42, 0.34, 0.43, 0.22, 0.59, 0.41, 0.58, 0.41, 0.26, 0.45, 0.16, 0.31, 0.39, 0.57, 0.43, 0.10, 0.46
17	0.24, 0.35, 0.39, 0.56, 0.37, 0.41, 0.52, 0.31, 0.52, 0.22, 0.58, 0.39, 0.39, 0.17, 0.46, 0.30, 0.37, 0.43
18	0.18, 0.17, 0.30, 0.22, 0.38, 0.48, 0.11, 0.49, 0.43, 0.47, 0.21, 0.29, 0.32, 0.36, 0.30, 0.56, 0.46, 0.42, 0.44
19	0.40, 0.14, 0.10, 0.43, 0.39, 0.27, 0.33, 0.59, 0.48, 0.36, 0.24, 0.28, 0.51, 0.59, 0.40, 0.39, 0.24, 0.35, 0.20, 0.14
20	0.42, 0.11, 0.47, 0.13, 0.16, 0.24, 0.58, 0.53, 0.38, 0.44, 0.18, 0.46, 0.47, 0.27, 0.53, 0.24, 0.33, 0.40, 0.32, 0.29, 0.44

Table B.1: Multi-field potential parameters c_i that define the potential in (4.9).

for single field potentials and by Eq. (4.9) for multifields. The relevant parameters c_i for higher number of fields are given by the list in table B.1 with the corresponding actions listed in table B.2. Note that the last component of the parameters $c_{n_\varphi+1}$ controls the degeneracy of the vacua. Tiny values of this parameter corresponds to thin wall scenarios, which is the case for the potentials with 15 and 19 fields. There, the action is notably larger. Nevertheless, as shown in fig. 4.7, the computational time of the bounce action is practically independent of whether the bounce is computed in thin or thick wall regime.

Action							
n_φ	PB_{10}	PB_{30}	PB_{100}	n_φ	PB_{10}	PB_{30}	PB_{100}
1	52.1	52.6	52.4	11	78.3	78.3	78.2
2	20.8	20.8	20.8	12	80.2	80.0	79.0
3	20.8	20.7	20.7	13	274	271	271
4	57.9	56.2	55.8	14	154	155	155
5	16.3	16.3	16.3	15	2.90×10^3	2.87×10^3	2.87×10^3
6	24.6	24.5	24.5	16	358	355	355
7	36.9	36.7	36.7	17	472	468	468
8	46.4	46.1	46.0	18	439	435	435
9	56.1	55.7	55.6	19	3.96×10^3	3.93×10^3	3.93×10^3
10	63.8	63.4	63.3	20	565	560	560

Table B.2: The bounce action of the single and multi-field potential in Eq. (B.6) and (4.9), respectively computed using `FindBounce` with 10, 30 and 100 number of field points.

Appendix C

Appendix to Chapter 4

C.1 A example of the Gel'fand Yaglom theorem in a $D = 1$ potential well

In general, the computation of functional determinants represents a non-trivial problem, which requires the knowledge of all the eigenvalues of an operator. However, there is an elegant method that allows us to calculate this object without having to compute any of the eigenvalues. This is the well-known Gel'fand Yaglom theorem.

In this section, we would like to illustrate how this procedure works in a simple one dimensional operator O under a potential well $V'' = m^2$. First, let us consider the usual eigenvalue problem with the Dirichlet boundary conditions defined on a finite interval $[0, L]$ given by

$$\mathcal{O}\psi_n = -\frac{d^2\psi_n}{dx^2} + m^2\psi_n = \lambda_n\psi_n, \qquad \mathcal{O}^{\mathrm{FV}}\psi_n^{\mathrm{FV}} = -\frac{d^2\psi_n^{\mathrm{FV}}}{dx^2} = \lambda_n^{\mathrm{FV}}\psi_n^{\mathrm{FV}}. \tag{C.1}$$

Here, all the eigenvalues are well known: $\lambda_n = m^2 + \left(\frac{n\pi}{L}\right)^2$ and $\lambda_n^{\mathrm{FV}} = \left(\frac{n\pi}{L}\right)^2$. Thus the ratio of determinants can be computed directly as

$$\frac{\det\mathcal{O}}{\det\mathcal{O}^{\mathrm{FV}}} = \prod_{n=1}^{\infty}\frac{\lambda_n}{\lambda_n^{\mathrm{FV}}} = \prod_{n=1}^{\infty}\left(1 + \left(\frac{mL}{n\pi}\right)\right)^2 = \frac{\sinh(mL)}{mL}. \tag{C.2}$$

Now, let us calculate the same functional determinants by means of the Gel'fand Yaglom theorem. That is, we need to solve an initial value problem of the form

$$\mathcal{O}\psi_0 = 0, \quad \mathcal{O}\psi_0^{\mathrm{FV}} = 0, \quad \psi_0(0) = \psi_0^{\mathrm{FV}}(0) = 0, \quad \psi_0'(0) = \psi_0'^{\mathrm{FV}}(0) = 1, \tag{C.3}$$

whose solutions are

$$\psi_0(x) = \frac{\sinh(mx)}{mx} \qquad \text{and} \qquad \psi_0^{\mathrm{FV}}(x) = x. \tag{C.4}$$

The functional determinant computed in this approach reads as

$$\frac{\det\mathcal{O}}{\det\mathcal{O}^{\mathrm{FV}}} = \frac{\psi_0(L)}{\psi_0^{\mathrm{FV}}(L)} = \frac{\sinh(mL)}{mL}. \tag{C.5}$$

which gives the same result (C.2).

This case is a somewhat trivial example since all the eigenvalues are simple and well-known, but in general we would like to consider more complicated potentials. The eigenvalue approach is rarely possible to perform, while the Gel'fand Yaglom is a differential equation with simpler boundary conditions that can be solved numerically. A rigorous mathematical derivation of this theorem can be found in [110, 199, 200, 202]. For more examples see [201].

C.2 The prefactor for polygonal bounce

Let us apply the semi-analytic polygonal bounce solution presented in chapters §3 and §4 to obtain the loop contributions of the general renormalizable potential in $D = 4$, given in (3.18). This potential can be recast in term of dimensionless quantities [99] as in (4.1), whose second derivative is given by

$$V''(\rho) = 1 - 3\bar{\varphi}(\rho) + \frac{3\alpha}{2}\bar{\varphi}^2(\rho), \qquad V''_{FV} = 1. \tag{C.6}$$

The crucial component to compute $\mathcal{R}_l$ in (5.10) from (5.9) is of course the semi-classical bounce solution $\bar{\varphi}$ from (3.2). As the ρ dependance of the bounce is provided explicitly, the integrals in eq. (5.12) are straightforward to compute analytically.

The total pre-factor contribution is then given by the sum of the low (5.11) and high l (5.12) pieces. In fig. C.1 we show the resulting $\mathcal{R}_l$ using the precise numerical shooting solutions and the PB approximation with the minimal $N = 3$ and the more precise $N = 50$.

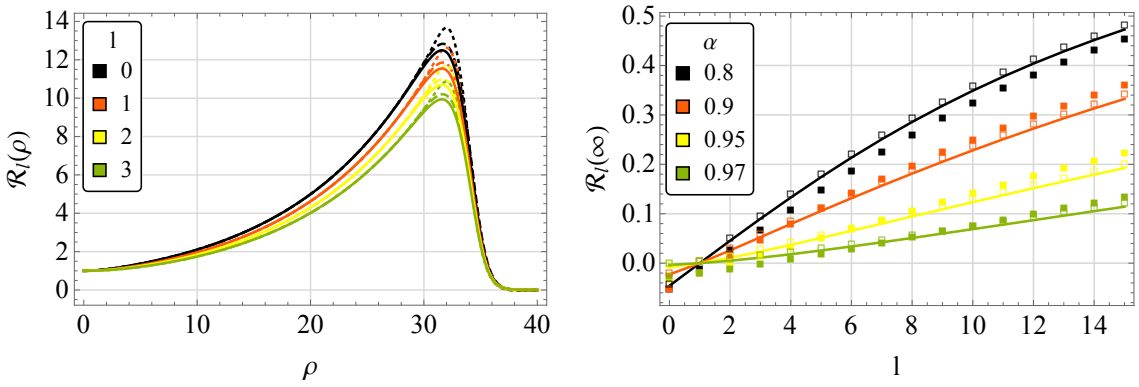

Figure C.1: The ratio of determinants $\mathcal{R}_l$ for a given multipole. Left: The ρ dependence for shooting in solid and the PB solution with $N = 3$ ($N = 50$) in dotted (dashed) lines. Right: The ratio at $\rho \to \infty$ with solid (empty) squares denoting the $N = 3$ ($N = 50$) PB approximation, while the solid line connects the results from the shooting procedure.

The values at infinity $\mathcal{R}_l(\infty)$ agree with the expectation of a single negative eigenvalue for $l = 0$, four-fold degenerate zero for $l = 1$ and the rest of $l \geq 2$ being positive. This is true for the precise shooting procedure, however the $N = 3$ PB bounce produces a number of negative eigenvalues, while for $N = 50$ the correct spectrum is recovered. This happens because the semi-classical solution is not approximating the exact potential with sufficient precision, the proof for one negative and multiple zero eigenvalues [187] (and the entire calculation of the fluctuations)

α	shooting	$N=3$	$N=10$	$N=50$	$N=100$
0.8	0.36	0.30	0.31	0.31	0.30
0.9	0.30	0.24	0.27	0.27	0.28
0.95	0.24	0.20	0.22	0.23	0.23
0.97	0.22	0.18	0.20	0.21	0.21

Table C.1: The total prefactor contribution at one-loop, computed using the numerical shooting procedure and compared with the polygonal method with $N = 3, 10, 50$ and 100 segmentation points. The rate is normalized to $(1-\alpha)^3$ and agrees with the analytical thin wall limit result that gives $9/32(1-2\pi/(9\sqrt{3})) \sim 0.17$.

relies on the fact that the semi-classical action is extremised. Nevertheless, blithely summing the absolute values of $\mathcal{R}_l(\infty)$ gives a rather precise (and very simple) estimate of the decay rate prefactor, as seen in table C.2.

The crude $N = 3$ approximation fails when $\alpha \ll 1$, however it works well in the thin wall limit when $\alpha \to 1$ and all of the approaches coincide, as shown on the right panel of fig. C.1.

C.3 Bessel, Saddle-point and Zeta function approximations

Bessel functions. To perform the high-l expansion in §5.4.2, we used the mathematical properties of the Bessel functions, which can be found on p. 378 of [210] eqs. (9.7.7) and (9.7.8). Expanding for large ν and ρ, while keeping ρ/ν fixed, we have up to $\mathcal{O}(\nu^{-4})$

$$I_\nu(\sqrt{\gamma}\rho)K_\nu(\sqrt{\gamma}\rho) = \frac{t}{2\nu} + \frac{t^3}{16\nu^3}\left(1 - 6t^2 + 5t^4\right) , \tag{C.7}$$

and up to $(1 + \mathcal{O}(\nu^{-1}))$

$$I_\nu^2(\sqrt{\gamma}\rho) = \frac{t}{2\pi\nu}e^{2\nu\eta} , \quad K_\nu^2(\sqrt{\gamma}\rho) \sim \frac{\pi\, t}{2\nu}e^{-2\nu\eta} , \tag{C.8}$$

with $\eta = t^{-1} + \ln\left(\sqrt{\gamma}\rho/\nu/\left(1 + t^{-1}\right)\right)$.

Saddle-point approximation can be found on p. 362 of [199, 200] eq. E.14. It can be used to expand the integrals in §5.4.2 in powers of $1/\nu$ when the leading contribution is dominated by the exponential high-l terms from (C.8). Expanding up to $\mathcal{O}(\nu^{-2})$

$$\int_0^\rho \mathrm{d}\rho_1 f(\rho_1)e^{\nu B(\rho_1)} = e^{\nu B(\rho)}\frac{f(\rho)}{\nu}\left(\frac{\mathrm{d}B(\rho)}{\mathrm{d}\rho}\right)^{-1} . \tag{C.9}$$

Generalized Riemann Zeta function. A useful asymptotic expansion of the derivatives of the generalized zeta function, is applicable in the TW limit $a \gg 1$ and

can be found in eqs. (18) and (19) of [211]

$$\zeta_R'(0,a) = \ln\Gamma(a) - \frac{\ln 2\pi}{2} \sim -a + a\log a - \frac{\log a}{2}, \tag{C.10}$$

$$\zeta_R'(-1,a) \sim -\frac{a^2}{4} + \frac{a^2\log a}{2} - \frac{a\log a}{2} + \frac{\log a}{12} + \frac{1}{12} - \sum_{k=1}^{\infty} \frac{B_{2k+2}a^{-2k}}{(2k+2)(2k+1)2k}, \tag{C.11}$$

$$\zeta_R'(-2,a) \sim -\frac{a^3}{9} + \frac{a^3\log a}{3} - \frac{a^2\log a}{2} + \frac{a}{12} + \frac{a\log a}{6} + \sum_{k=1}^{\infty} \frac{2B_{2k+2}a^{-(2k-1)}}{(2k+2)(2k+1)2k(2k-1)}, \tag{C.12}$$

where B_k are the Bernoulli numbers.

C.4 Derivation of the high-l expansion of f_l

This section is devoted to the derivation of $\ln f_l^a$ in (5.55) from the high-l expansion of $\ln f_l$ in (5.50) up to $\mathcal{O}(\nu^{-4})$, while keeping $\rho \to \infty$. For this purpose, let us first plug V'' from (5.54) into (5.50) and separate the integrals in three parts: the terms proportional to the delta function, to the Heaviside and the cross terms.

Delta function terms come purely from the discontinuity of the first derivative of the potential $\bar{\varphi}(R_T) = 0$. One can compute the integrals exactly and perform the high-l expansion from (C.7). This gives the terms proportional to $(\mu_V R_T)$ in (5.55), one for each insertion of V''. For instance, the last three terms of (5.50), which are of third order in V'' are

$$\ln f_l^a \supset -\frac{1}{3}\left(\mu_V R_T I_\nu(\sqrt{\gamma}\rho)K_\nu(\sqrt{\gamma}\rho)\right)^3 \sim -\frac{1}{3}\left(\frac{t}{2\nu}\mu_V R_T\right)^3, \tag{C.13}$$

where we kept all the terms up to $\mathcal{O}(\nu^{-4})$.

Heaviside terms belong to the continuous part of V''. They were first computed by [99, 100] and contribute to the first term of (5.55). Let us proceed to compute each term of (5.50) by neglecting the delta terms.

The leading order terms in V'' can be computed simply by using the Bessel expansions in (C.7). The second order terms in V'' can first be simplified by

$$\int_0^\infty \mathrm{d}\rho_1 \int_{\rho_1}^\infty \mathrm{d}\rho = \int_0^\infty \mathrm{d}\rho \int_0^\rho \mathrm{d}\rho_1\,, \tag{C.14}$$

since V'' is continuous, as shown in the Appendix E of [199, 200]. At $\mathcal{O}(\nu^{-4})$, this leads to

$$\ln f_l^a \supset \sum_s \int_0^\infty \mathrm{d}\rho\,\rho \int_0^\rho \mathrm{d}\rho_1 \rho_1 K_\nu^2(\sqrt{\gamma}\rho) V_s''(\rho)\, V_s''(\rho_1)\, I_\nu^2(\sqrt{\gamma}\rho_1) \tag{C.15}$$

$$\sim \frac{t^3}{8\nu^3}\sum_s \int_0^\infty \mathrm{d}\rho\,\rho^3 V_s''^2 H\left((-1)^s(\rho - R_T)\right), \tag{C.16}$$

where we used the exponential behavior of I_ν and K_ν in (C.8) and the saddle-point approximation (C.9) in the last step. Finally, the third order terms go as $\mathcal{O}(\nu^{-4})$

and do not contribute to f_l^a since each pair of Bessel functions (C.8) as well as the saddle-point approximation (C.7) come with a factor of $1/\nu$.

Cross terms require a careful treatment in the integration of the delta function since it brings a Heaviside that affects the limits of integration of the second integration. Then we perform the asymptotic expansion of the Bessel functions and the saddle-point approximation as in the previous calculations with (C.8) and (C.9). These correspond to the last two terms of (5.55). For example, the last term of (5.55) is given by

$$\begin{aligned}\ln f_l^a &\supset \sum_s \int_0^\infty \mathrm{d}\rho\rho K_\nu^2\left(\sqrt{\gamma}\rho\right) V_s''\left(\rho\right) \int_0^\rho d\rho_1\, \rho_1 \mu_V \delta\left(\rho - R_T\right) I_\nu^2\left(\sqrt{\gamma}\rho_1\right) \\ &= \mu_V R_T I_\nu^2\left(\sqrt{\gamma}R_T\right) \sum_s \int_{R_T}^\infty \mathrm{d}\rho\rho K_\nu^2\left(\sqrt{\gamma}\rho\right) V_s''\left(\rho\right) H(\rho - R_T) \\ &\sim \frac{1}{\mu_V^2}\left(\frac{t}{2\nu}\mu_V R_T\right)^3 V_2''\left(R_T\right) ,\end{aligned} \tag{C.17}$$

where in the second line, the integration limits has changed due to the previous integration of the delta function, which picks V_2'' [1] . Then we used the saddle point approximation that evaluates the potential at R_T and provides the last line.

The next to last term of (5.55) can be computed completely analogously, while the remaining terms in (5.50) cancel among themselves or go as $\mathcal{O}\left(1/\nu^4\right)$. After collecting all the results, we are left with the final expression given in (5.55).

[1] This actually depends on our convention of the Heaviside. We have chosen that $H(x) = 0$ when $x < 0$ but equivalently, we could have used $H(x) = 1/2$ when $x = 0$ and, after adding up all the cross terms in $\ln f_l^a$, we recover the same results.

Razširjeni povzetek

7.1 Uvod

V kvantni teoriji polja imamo lahko potencial z več nedegeneriranimi minimi, kot je prikazano na levem grafu na sliki 7.1, kjer je globalni minimum stabilno stanje, znano kot pravi vakuum (PV), medtem ko so ostali, ki so le lokalni, metastabilni. Slednji so lažna vakuumska (LV) stanja, saj bodo slej ko prej razpadli v bolj ugodno stanje nižje energije s procesom tuneliranja skozi bariero, analognim alfa razpadu v kvantni mehaniki.

Razpad povzročijo kvantne in termodinamske fluktuacije polj, pri katerih se sčasoma nekje v vesolju tvorijo mehurčki pravega vakuuma. Ko enkrat nastanejo, se širijo skoraj s svetlobno hitrosjo v vakuumu, oziroma z neko končno hitrostjo pri visokih temeperaturah, ob tem pa pretvorijo celoten prostor v novo fazo pravega vakuuma. Ta proces je znan kot fazni prehod prvega reda, zaradi nenandnih sprememb stanja ali spontanega nastajanja mehurčkov, kar je analogno vrenju pregrete/podhlajene tekočine ali nukleacijskemu procesu v statistični fiziki.

Razpad vakuuma igra pomembno vlogo v omejevanju mase Higgsovega bozona [3, 4, 5], zaradi izjemnih in fundamentalnih posledic pa je že bil deležen natančnih izračunov in posvečenih študij. Najnovejša dela so npr. v [6, 7, 8] in tamkajšnjih referencah, nudijo pa oceno življenske dobe našega vesolja, ki znaša $\sim 10^{139^{+102}_{-51}}$ let [9, 10]. Vendar pa se lahko ta slika dramatično spremeni [11] s fiziko, ki jo pričakujemo onkraj standardnega modela (SM) [12, 13, 14, 15, 16, 17, 18, 19, 20, 21, 22, 23, 24, 25]. Stabilnost vakuuma tako postavi nepogrešljive in morda fundamentalne omejitve, ki jih gre upoštevati v izdelavi kakršnekoli nove teorije.

Tega procesa se ne da opazovati v laboratoriju, lahko pa vodi do eksotičnih kozmoloških posledic, ki jih lahko zaznamo v prihodnjih eksperimentih. V zgodnjem vesolju delci tvorijo vročo plazmo, katere termalni učinki lahko sprožijo fazni prehod [26, 27, 28, 29]. Trk mehurčkov sprosti ogromno energije, zato predstavlja naraven vir gravitacijskih valov [30, 31, 32, 33, 34, 35, 36, 37] in prvobitnih magnetnih polj [38, 39, 40, 41, 42]. Poleg tega lahko dinamično proizvedejo opaženo prevlado materije nad antimaterijo, npr. v elektrošibki bariogenezi [43, 44, 45, 46, 47, 48, 49] (glej pregled v [50]).

Zaznava gravitacijskih valov leta 2015 [60] je prinesla novo obdobje astronomije in zanimivih možnosti v fiziki visokih energij. Trenutni aLIGO [61] in aVIRGO [62] observatoriji obratujejo pri frekvencah, ki povečini niso občutljive na fazne prehode prvega reda pri TeV skalah. Načrtuje pa se, da bodo detektorji gravitacijskih valov, kot so LISA [63], DECIGO [64] in BBO [65, 66], ki se bodo nahajali v vesolju, izstreljeni čez dobro desetletje in da bodo iskali dokaze za kozmološke fazne prehode. Nedaven pregled sposobnosti LISA najdemo v [63].

Fazni prehod lokalnega osnovnega stanja v QFT s tunelinranjem se preučuje že vse od pionirskih del [28, 30, 67, 68, 69]. V sklopu teh del so odkrili, da je razpadna verjetnost na enoto volumna prostorčasa dana z

$$\frac{\Gamma}{\mathscr{V}} = A\, e^{-\mathcal{S}_0/\hbar}\,(1 + \mathcal{O}(\hbar))\,, \tag{7.1}$$

v limiti, ko je $\hbar$ majhna. Evklidska akcija $\mathcal{S}_0$ je tu akcija v evklidskem prostoru, izvrednotena v odbojnem polju $\bar{\varphi}$, A pa je neka dimenzionalna količina.

Odbojno polje je netrivialna distribucija skalarnega polja, ki ekstremizira evklidsko akcijo in opiše fazni prehod med vakuumskimi stanji. Člen $\mathcal{S}_0$, običajno imenovan odbojna akcija, prevladuje v razpadni širini zaradi eksponentne odvisnosti in predstavlja glavni predmet tega dela. Koeficient A je povezan z enozančnimi izračuni in predstavlja prispevke višjega reda k razpadni širini. Ni močno odvisen od parametrov teorije, zato ga lahko ocenimo na podlagi dimenzijskih argumentov. Preden bi se spustili v podrobne račune, bi privzeli, da je približno podan z $A \approx v^4$, kjer je v neka karakteristična masna skala preučevane teorije.

Kot je pokazano v [111, 112], je rešitev $\bar{\varphi}$ invariantna na $O(D)$ rotacije za vse dimenzije $D > 2$. To pomeni, da lahko prepišemo in poenostavimo enačbo (2.9) s sfernimi koordinatami v D-razsežnem evklidskem prostoru, pri čemer postane φ funkcija samo radialne koordinate,

$$\varphi\,(t, \mathbf{x}) = \varphi\,(\rho) \qquad \text{with} \qquad \rho = \sqrt{(\tau - \tau_0)^2 + (\mathbf{x} - \mathbf{x_0})^2}\,, \tag{7.2}$$

po preostalih $D-1$ kotih pa se da takoj integrirati. Zato je

$$\mathcal{S}_0 = \frac{2\pi^{\frac{D}{2}}}{\Gamma\left(\frac{D}{2}\right)} \int_0^\infty \rho^{D-1} \mathrm{d}\rho \left(\frac{1}{2}\dot{\varphi}^2 + V\right) = \mathcal{T}_D + \mathcal{V}_D\,, \tag{7.3}$$

kjer pika predstavlja odvod po ρ, zadnja dva člena pa predstavljata posebej integrirana kinetični in potencialni del. Konfiguracije polja, ki ekstremizirajo akcijo, morajo rešiti enačbo

$$\frac{\delta \mathcal{S}_0}{\delta \varphi} = 0 \implies \ddot{\varphi} + \frac{D-1}{\rho}\dot{\varphi} = \frac{\partial V}{\partial \varphi}\,, \tag{7.4}$$

pri čemer mora rešitev zadoščati še (2.10) in biti analitična funkcija pri $\rho = 0$. Tako so ustrezni robni pogoji

$$\varphi(0) = \varphi_0, \qquad \varphi\,(\infty) = \varphi_+, \qquad \dot{\varphi}\,(0) = \dot{\varphi}\,(\infty) = 0\,. \tag{7.5}$$

Zaradi teh pogojev se rešitev te enačbe imenuje **odboj**.

Začetna vrednost polja φ_0 predstavlja vrednost skalarnega polja v središču mehurčka, nahajajočega se pri $(\tau_0, \mathbf{x_0})$ kot definirano v (7.2). Sicer dopušča trivialno rešitev $\varphi_0 = \varphi_+$, pri kateri vrednost polja ostaja konstantna, relevantna pa je tista, pri kateri je φ_0 nekje blizu PV, pod lokalnim minimom energije, kot je prikazano na levem grafu na sliki 7.1. V principu je to vmesno začetno vrednost možno najti numerično do poljubne natančnosti s **strelsko** metodo. Vendar pa ima ta numerični pristop več pomanjkljivosti glede odbojnega polja, ki so natančno naštete v §2.2.

Vse te težave naslovimo z novim pristopom, imenovanim Poligonski odboj (PO), ki se izogne strelski metodi in izračuna odbojno akcijo za poljubno število polj.

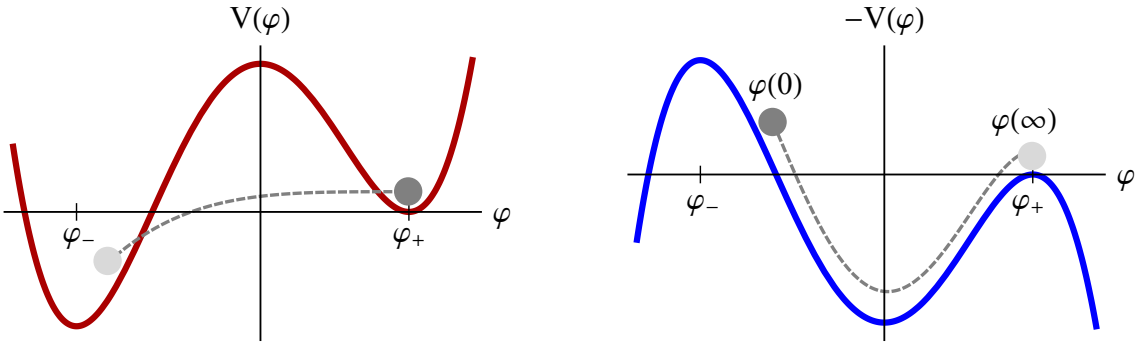

Slika 7.1: Levo: Primer potenciala z dvema minima z nestabilnim lažnim vakuumskim stanjem pri φ_+ in stabilnim pravim pri φ_-. Desno: Potencial z leve po analitičnem nadaljevanju v evklidski prostor. Polje začne v netrivialni vrednosti φ_0, tako da v neskončnosti doseže pravi vakuum.

7.2 Poligonski odboj

Ta pristop je semi-analitična metoda, ki izračuna razpadno širino lažnega vakuumskega stanja za poljubno število skalarnih polj in prostorskočasovnih dimenzij. Osnovan je na naboru poljubnega števila linearnih segmentov, ki opiše potencial z več minimi. Točni razvoji polja za vsak segment so združeni v popoln opis konfiguracije odbojnega polja. Z večanjem števila segmentov lahko odbojno akcijo izvrednotimo do željene natančnosti, pri čemer dobljene ujemalne enačbe rešimo kvazi-analitično.

Bolj eksplicitno, generičen potencial z dvema minima $V(\varphi)$ aproksimiramo z odsekoma linearnimi potenciali, kot je prikazano s črtkano črto na sliki 7.2. Indeksi segmentov za vrednosti polja $\tilde{\varphi}_s, s = 1, \ldots, N$, so taki, da je PV pri $\tilde{\varphi}_1$ in LV pri $\tilde{\varphi}_N$, vrednosti potenciala pa označimo z $\tilde{V}_s = V(\tilde{\varphi}_s)$.

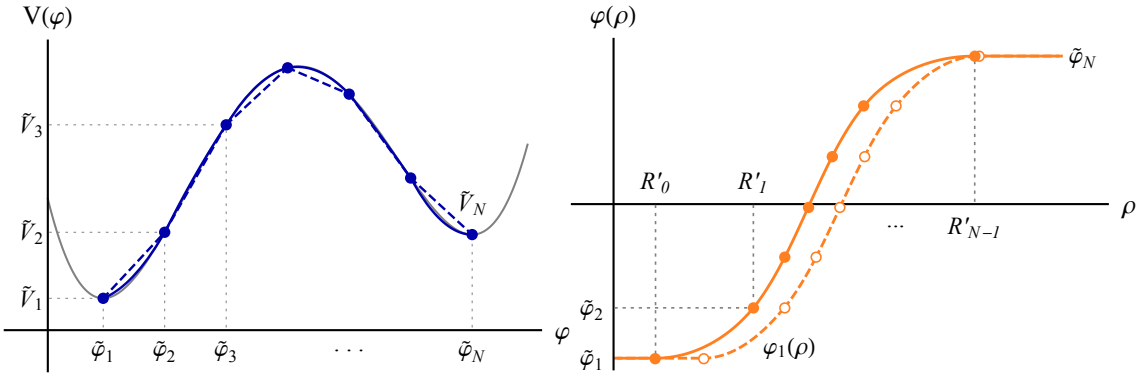

Slika 7.2: Levo: Linearno zamaknjen kvartični potencial v sivem, linearna poligonska aproksimacija $N = 7$ v črtkano modrem in kvadratični popravki drugega reda v polnem modrem. Desno: Rešitev polja v aproksimaciji PO v črtkanem oranžnem in izboljšana rešitev drugega reda v polnem oranžnem.

Linearni segmenti in njihove rešitve enačbe (7.4) v $D > 2$ prostorskočasovnih

dimenzijah so podane preprosto z

$$V_s(\varphi) = \underbrace{\left(\frac{\tilde{V}_{s+1} - \tilde{V}_s}{\tilde{\varphi}_{s+1} - \tilde{\varphi}_s}\right)}_{8\,a_s} (\varphi - \tilde{\varphi}_s) + \tilde{V}_s, \quad \varphi_s(\rho) = v_s + \frac{4}{D} a_s \rho^2 + \frac{2}{D-2} \frac{b_s}{\rho^{D-2}}. \quad (7.6)$$

Z zahtevo, da je odboj, tako kot črtkana črta na desnem grafu na sliki 7.2, v celoti gladka rešitev, dobimo tri pogoje za vsak segment: dva za vrednost polja, ki se mora ujemati z začetno segmentacijo pri R_s, in še enega za njen odvod:

$$\varphi_s(R_s) = \tilde{\varphi}_{s+1} = \varphi_{s+1}(R_s), \qquad \dot{\varphi}_s(R_s) = \dot{\varphi}_{s+1}(R_s). \quad (7.7)$$

Ko je segmentacija $\{\tilde{\varphi}_s\}$ vzpostavljena, so parameteri a_s določeni s (7.6), medtem ko so ostali odbojni parametri, v_s, b_s in radiji R_s, $s = 0, \ldots, N-1$, določeni z ujemalnimi pogoji (7.7). V splošnem se dá vse parametre, razen radijev R_{in}, dobiti analitično, neodvisno od števila segmentov. Nazadnje lahko poljubno večamo število segmentov brez uvedbe dodatnih prostih parametrov in sistematično najdemo odbojno akcijo z željeno natančnostjo.

Lahko gremo še korak dlje in razvijemo splošen postopek dodajanja nelinearnih popravkov k PO, ki je predstavljen s polno črto na sliki 7.2. To storimo tako, da vzpostavimo sistematičen postopek, osnovan na Taylorjevem razvoju potenciala, ki zgradi celotno obojno rešitev, razvito okoli PO, kot $\varphi = \varphi_{\mathrm{PB}} + \xi$. Tako je popravek potenciala izvrednoten na PB ozadju in odbojna enačba postane

$$\ddot{\varphi} + \frac{D-1}{\rho}\dot{\varphi} = 8\,(a + \alpha) + \delta dV\,(\rho)\,, \qquad \ddot{\xi} + \frac{D-1}{\rho}\dot{\xi} = 8\alpha + \delta dV(\rho), \quad (7.8)$$

kjer je α poljuben linearen del, $\delta dV(\rho)$ pa je majhna perturbacija potenciala. Po linearizaciji potenciala okoli $\tilde{\varphi}_s$ je rešitev odbojne enačbe ξ dana kot

$$\xi = \nu + \frac{2}{D-2}\frac{\beta}{\rho^{D-2}} + \frac{4}{D}\alpha\rho^2 + \mathcal{I}_D. \quad (7.9)$$

Tu se nehomogeni del popravka za $D = 3, 4$ izvrednoti kot

$$\mathcal{I}_3 = \partial^2\tilde{V}\left(\frac{v - \tilde{\varphi}}{6}\rho^2 + b\rho + \frac{a}{15}\rho^4\right), \quad \mathcal{I}_4 = \partial^2\tilde{V}\left(\frac{v - \tilde{\varphi}}{8}\rho^2 + \frac{b}{2}\ln\rho + \frac{a}{24}\rho^4\right).$$

Koeficienti ν_s, β_s in novi ujemalni radiji so izračunani s pomočjo zahteve, da je rešitev zvezna in odvedljiva, tako kot v primeru PO v enačbi (7.7).

Rešitev PO je formalno točna, ko gre $N \to \infty$, a nelinearni popravki izboljšajo konvergenco akcije, odvisno od potenciala in reda, do katerega delamo. Odbojna akcija za splošen renormalizabilen potencial v $D = 4$ prostorskočasovnih dimenzijah je dana na sliki 7.3, kjer parameter ϵ teče od skoraj degeneriranega minima pri $\epsilon = 0.01$ do velike separacije skal pri $\epsilon = 0.08$. Nižje obarvane črte ustrezajo popravljeni akciji, višje sive pa kažejo vodilni red PO za primerjavo.
Verjetnost za razpad lažnega osnovnega stanja v modelu s poljubnim številom realnih skalarnih polj φ_i je prav tako sorazmerna evklidski akciji $\mathcal{S}_0$ in je dana z (7.1). Kot so nedavno pokazali v [112], ohranja odboj v prisotnosti večih skalarnih polj $O(D)$ invarianco, zato se evklidska akcija (7.3) naravno posploši na več polj,

$$\mathcal{S}_0 = \frac{2\pi^{\frac{D}{2}}}{\Gamma\left(\frac{D}{2}\right)} \int_0^\infty \rho^{D-1}\,\mathrm{d}\rho \left(\frac{1}{2}\sum_i^{n_\varphi} \dot{\varphi}_i^2 + V(\varphi_i)\right), \quad (7.10)$$

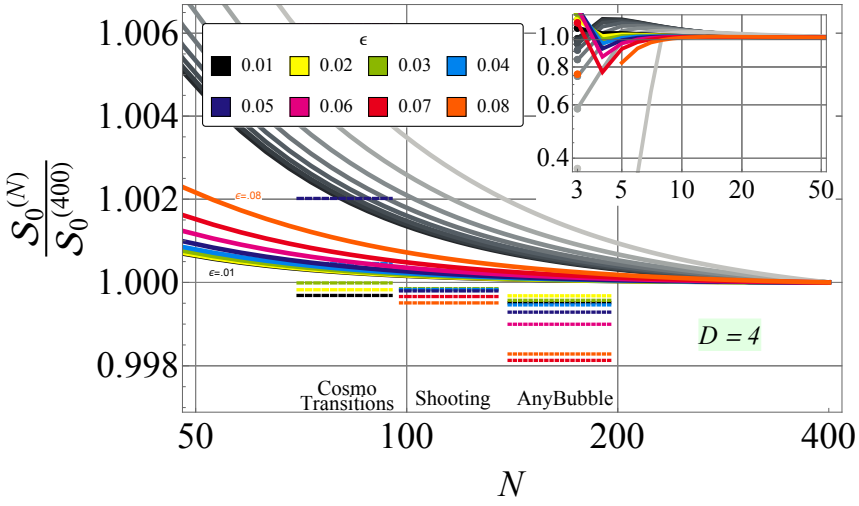

Slika 7.3: Odbojna akcija izboljšanega izračuna odboja, ki vključuje popravke drugega reda.

kjer n_φ pomeni število polj. Odbojna polja rešijo Euler-Lagrangeovo enačbo in robne pogoje

$$\ddot{\varphi}_i + \frac{D-1}{\rho}\dot{\varphi}_i = \partial_i V, \qquad \varphi_i(0) = \varphi_{i0}, \qquad \varphi_i(\infty) = \tilde{\varphi}_{iN}, \qquad \dot{\varphi}_i(0,\infty) = 0, \tag{7.11}$$

kjer je $\partial_i V$ odvod V po φ_i. Obravnava odboja potencialov z večimi polji je mnogo težja, saj moramo integrirati sklopljen sistem diferencialnih enačb polja. Izhodišče je začetna ocena rešitve,

$$\bar{\varphi}_{is} = \bar{v}_{is} + \frac{2}{D-2}\frac{\bar{b}_{is}}{\rho^{D-2}} + \frac{4}{D}\bar{a}_{is}\rho^2, \tag{7.12}$$

kjer je i indeks polja, $i = 1, \ldots, n_f$, in $s = 1, \ldots, N$ segmentna točka. Potem si ogledamo razvoj okoli začetne ocene, da je $\varphi_{is}(\rho) = \bar{\varphi}_{is} + \zeta_{is}$. To vodi do nabora sklopljenih odbojnih enačb za vsako smer polja

$$\underbrace{\ddot{\bar{\varphi}}_{is} + \frac{D-1}{\rho}\dot{\bar{\varphi}}_{is}}_{8\bar{a}_{is}} + \underbrace{\ddot{\zeta}_{is} + \frac{D-1}{\rho}\dot{\zeta}_{is}}_{8a_{is}} = \frac{dV}{d\varphi_i}\left(\bar{\varphi} + \zeta\right). \tag{7.13}$$

Ideja je, da poiščemo rešitev razvoja polja ζ, ki je poligonskega tipa

$$\zeta_{is} = v_{is} + \frac{2}{D-2}\frac{b_{is}}{\rho^{D-2}} + \frac{4}{D}a_{is}\rho^2, \tag{7.14}$$

kjer a_{is} ustreza vodilni konstanti razvoja gradienta potenciala okoli neke deformirane poti, definirane z $\tilde{\varphi}_{is} + \tilde{\zeta}_{is}$. To je glavna razlika od primera z enim poljan: položaj v prostoru polj ni fiksiran a priori, zato moramo dopustiti, da se segmentacija premika v prostoru polj.

Parametre gradienta a_{is} lahko lineariziramo v premiku $\tilde{\zeta}_{js}$ s simetričnim povprečjem

$$8a_{is} \simeq \frac{dV}{d\varphi_i}\left(\tilde{\varphi}_{is} + \tilde{\zeta}_{is}\right) - 8\bar{a}_{is}, \qquad \frac{dV}{d\varphi_i} \simeq \frac{d_i\tilde{V}_s + d_i\tilde{V}_{s+1} + d_{ij}^2\tilde{V}_s\tilde{\zeta}_{js} + d_{ij}^2\tilde{V}_{s+1}\tilde{\zeta}_{js+1}}{2},$$

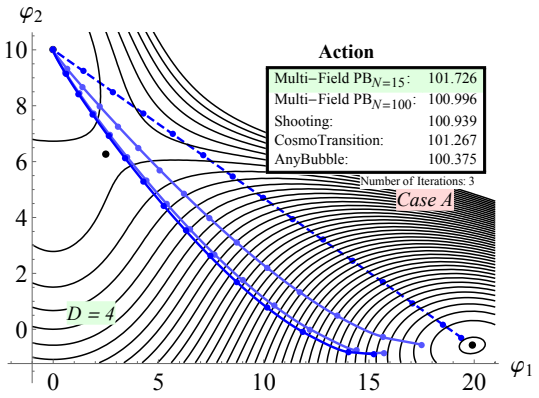

Slika 7.4: Levo: Primer potenciala z dvema poljema, trajektorija odboja v modrem in njena projekcija na dnu. Rdeča črtkana črta je pot, izračunana brez interakcij med polji, polna rdeča črta pa je pot, ki minimizira potencial. Polna modra črta predstavlja večpoljsko poligonsko rešitev v $D = 4$ z $N = 15$ segmentacijskimi točkami. Desno: Nivojnice potenciala na levi. Ravna črtkana črta je izhodiščni nastavek, ki povezuje dva minima s sedlom. Oba minima in sedlo so označeni s črnimi pikami, polne črte so kasnejše iteracije, ki konvergirajo h končni poti, ki reši odbojne enačbe. Vstavljena tabela prikazuje akcijo v primerjavi z drugimi pristopi.

kjer je potencial razvit preko vodilnega reda do $\mathcal{O}(\tilde{\zeta})$, da vključuje tudi drugi odvod potenciala, ki je potreben za pravilen opis ukrivljenih poti v prostoru polj. Robni pogoji prinesejo nabor izrazov $\zeta_{is}(R_s) = \tilde{\zeta}_{is+1}$, ki se lahko zapiše kot sistem linearnih enačb za novo pot, tega pa se dá hitro in učinkovito rešiti. To pot lahko uporabimo kot novo izboljšano oceno za deformacijo poti in postopek ponavljamo, dokler se trajektorija v prostoru polj neha spreminjati, torej je $\tilde{\zeta}_{is} \simeq 0$. To je enostavno doseči po konstrukciji, saj smo ohranili (7.14) v poligonski obliki v ρ.

Da ponazorimo večpoljsko metodo PO, smo si ogledali enostaven dvopoljski potencial $V(\varphi_i) = \sum_{i=1}^{2}(-\mu_i^2\varphi_i^2 + \lambda_i^2\varphi_i^4) + \lambda_{12}\varphi_1^2\varphi_2^2 + \tilde{\mu}^3\varphi_2$, ki ima več rešitev za vakuumske pričakovane vrednosti $\langle\varphi_i\rangle = v_i$, ki zlomijo simetrijo. Metastabilni minimi so različnih globin $V(v_1) \neq V(v_2)$, kar omogoča lokalnemu lažnemu vakuumu, da razpade v globalni minimum s premikanjem vzdolž odbojne rešitve v prostoru polj. Rešitev v prostoru polj je prikazana na sliki 7.4, kjer je začetni nastavek ravna črta z $N = 15$, ki povezuje minima. Rešitev PO konvergira k pravi vrednosti izjemno hitro, z $\mathcal{O}(1)$ iteracijami, kot je razvidno s slike 7.4.

Iz vložene tabele na sliki 7.4 je jasno, da je akcija PO kar točna tudi že za $N = 15$ in doseže promilsko natančnost z $N = 100$. Glavni pogoj za izboljševanje točnosti akcije je večanje števila segmentov za natančnejši opis longitudinalne odvisnosti. Oblika poti v prostoru polj je manj pomembna in se ne spreminja dosti z večanjem N. Vsi gornji rezultati so podobni za $D = 3$.

7.3 FindBounce: Paket za večpoljsko odbojno akcijo

Na osnovi konstrukcije PO smo ustvarili robusten in uporabniku prijazen `Mathematica` paket, imenovan `FindBounce`, ki implementira našo metodo. Ker je zasnovan na pod-

lagi semi-analitične strukture, njegova računska zahtevnost raste linearno s številom polj in številom segmentov. Predstavili bomo nekaj aplikacij in primerjav z drugimi orodji, pri katerih je izvajalni čas v grobem maj kot 1 (2) sekundi za 10 (20) polj z 0.5% natančnostjo akcije.

Paket `FindBounce` je izdan v datotečnem formatu `.paclet`, ki vsebuje vso kodo, dokumentacijo in druge potebne vire. Najnovejša različica datoteke `.paclet` je na voljo na zbirališčni "releases" strani (`https://github.com/vguada/FindBounce/releases`), namesti pa se jo tako, da se koda požene z `Mathematica`.

```
In[1]:= PacletInstall["full/path/to/FindBounce-X.Y.Z.paclet"]
```

To bo namestilo paket `FindBounce` v `$UserBasePacletsDirectory`. Ko je enkrat nameščen, ga naložimo z `Needs`.

```
In[2]:= Needs["FindBounce`"]
```

Za dostop do dokumentacije lahko v vmesniku zvezka odpremo pomočniško okno in poiščemo `FindBounce`. Kot enostaven primer si oglejmo naslednji potencial:

```
In[3]:= V[x_]:= 0.5 x^2 + 0.5 x^3 + 0.12 x^4;
```

```
In[4]:= extrema = x/.Sort@Solve[D[V[x],x]==0];
```

Odboj s funkcijo `FindBounce` doblimo kot

```
In[5]:= bf = FindBounce[V[x],x,{extrema[[1]],extrema[[3]]}]
```

kjer je vrstni red minimov poljuben.

```
Out[5]= BounceFunction[  Action: 73500.
                        Dimension: 4 ]
```

Vse opcije imajo privzete vrednosti, rezultate pa lahko izvlečemo takole:

```
In[6]:= bf["Action"]
```

```
Out[6]= 73496.
```

Preučujemo lahko tudi poljubne čisto polilinearne potenciale, tako da priskrbimo množico točk in njihovih vredosti potenciala $\{\tilde{\varphi}, V(\tilde{\varphi})\}$:

```
FindBounce[{{x1,V1},{x2,V2},...}]
```

Za večpoljske potenciale izvrednotenje izvršimo s sledečo sintakso:

```
FindBounce[V[x,y,...],{x,y,...},{m1,m2}]
```

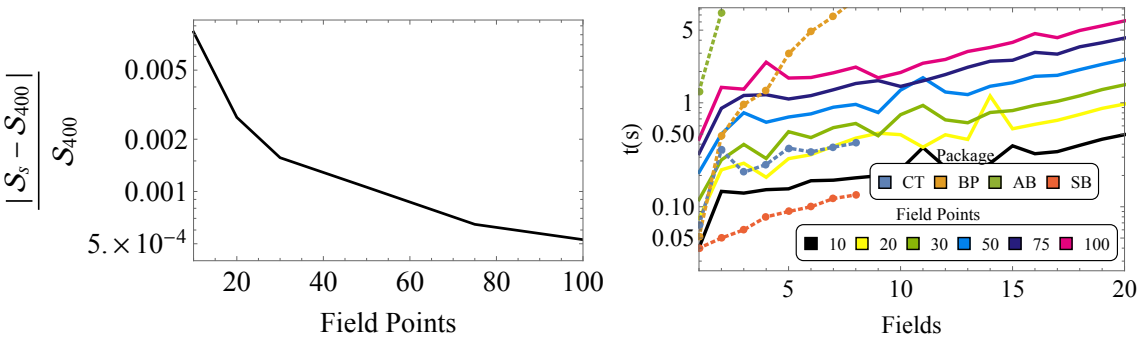

Slika 7.5: Levo: Povprečje večpoljske odbojne akcije $\mathcal{S}_s$, normalizirano na povprečje z $N = 400$ točkami polja. Desno: Meritve časa v večpoljskem primeru v odvisnosti od števila polj za več točk polja. Polne črte smo dobili s `FindBounce` z `"ActionTolerance"` $\to 10^{-4}$. Črtkane črte s pikami so meritve časa za druga obstoječa orodja, glej besedilo za podrobnosti.

kjer sta $m_{1,2}$ večpoljska minima.

Da lahko bolj cenimo učinkovitost metode, smo izračunalni odbojno akcijo za različna števila oz. segmentov, kot je predstavljeno na desnem grafu na sliki 7.5. Odbojno akcijo smo izpovprečili za različne parametre potenciala in polj ter jo normirali na tisto z $N = 400$ točkami polja. Ugotovimo, da je izračunana akcija natančna do približno 1% za 31 točk polja, kar je standardna nastavitev. Vendar pa je mogoče prilagoditi privzete nastavitve `FindBounce`, kot so `"FieldPoints"` in `"ActionTolerance"`, da dobimo odbojno akcijo poljubno natančno za katerikoli tip potenciala, kot je prikazano na desnem grafu na sliki 7.5.

Nato smo število polj višali od enega do dvajset, da smo ocenili računski čas, kot je prikazano na levem grafu na sliki 7.5. Za primerjavo tu vključujemo rezultate drugih metod, na voljo v literaturi: `CosmoTransition`(CT) [82], `AnyBubble`(AB) [86], `BubbleProfile`(BP) [88] in `SimpleBounce`(SB) [177]. Računski čas `FindBounce` narašča linearno s številom polj n_φ, kot je prikazano s polnimi črtami, katerih barve pomenijo različna števila točk polja. Še več, časovna zahtevnost `FindBounce` glede na število točk polja narašča linearno tudi s številom polj.

Časovna primerjava z drugimi orodji je odvisna od sposobnosti CPU in optimizacijske učinkovitosti implementacije v danem programskem jeziku. V naši postavitvi se izkaže, da je računski čas `FindBounce` za 10(20) polj manj kot 1(2) sekundi za privzeto vrednost z 31 točkami polja. Izračun je bil opravljen z uporabo standardnih `Mathematica` funkcij `AboluteTiming` in `RepeatedTiming` na namiznem sistemu iMac 10.12.6, opremljenim s procesorjem Intel Core i7 (procesorska hitrost 3.4 GHz) in 16 GB DDR3 RAM-a (obratujočega pri 1.6 GHz).

Za druge implementacije so bile infomacije o časovnih meritvah vzete iz [88] in [177]. Ugotovili smo, da je `FindBounce` primerljiv s temi orodji, kar se hitrostne izvedbe tiče, to pa je prikazano tudi na desnem grafu na sliki 7.5. Posebej je časovna zahtevnost z $N = 10$ točkami polja primerljiva z vrednostmi, citiranimi v `SimpleBounce` in `CosmoTransition`. Treba je opozoriti, da so gornja orodja implementirana v `C++` in `Python`, medtem ko je `FindBounce` napisan v `Mathematica` brez bistvene numerične optimizacije.

7.4 Kvantne fluktuacije

V tej disertaciji prav tako opišemo postopek, ki izračuna prispevke višjega reda k razpadni širini za vse gladke potenciale. To metodo tudi razširimo, da zaobjame potenciale z nezveznimi prvimi odvodi, in eksplicitno izvrednotimo točno razpadno širino na nivoju ene zanke za realno in kompleksno skalarno polje v bikvartičnem potencialu z dvema minima na drevesnem redu.

Glavni namen tega razdelka je, da na kratko opišemo, kako izpeljati te rezultate, začenši z dobro znanim eksplicitnim izrazom za razpadno širino vakuuma na nivoju ene zanke [30, 69, 92, 93, 185, 186]

$$\frac{\Gamma}{\mathscr{V}} = \left(\frac{\mathcal{S}_0}{2\pi}\right)^2 \mathrm{Im}\sqrt{\frac{\det\mathcal{O}_{\mathrm{LV}}}{\det'\mathcal{O}}}\, e^{-\mathcal{S}_0}\left(1+\mathcal{O}\left(\hbar\right)\right), \tag{7.15}$$

kjer črtica v det' nakazuje, da so ničelni lastni načini izpuščeni, števec pa je v normalizaciji LV. Odbojno akcijo $\mathcal{S}_0$ bikvartičnega potenciala je enostavno izraziti v zaključeni obliki.

Izpeljava je podobna metodi PO, pri kateri združimo dve kopiji dobro znane čisto kvartične rešitve, kot je to podrobno izvedeno v razdelku §2.5.2. Nato za izračun determinante iščemo produkt lastnih vrednosti $\gamma_{\mathbf{n}}$ operatorja $\mathcal{O}$:

$$\mathcal{O} = -\Box + V''\left(\overline{\varphi}\right), \qquad \mathcal{O}\psi_{\mathbf{n}} = \gamma_{\mathbf{n}}\psi_{\mathbf{n}}, \tag{7.16}$$

Tu je $\Box$ Laplaceov operator v ravnem 4D Evklidskem prostorčasu, $V''(\rho)$ drugi odvod potenciala, izvrednoten pri odboju, $\mathbf{n}$ pa skupni indeks za relevantna kvantna števila, ki se pojavijo ob zadostitvi robnih pogojev $\psi_{\mathbf{n}}(0) = \psi_{\mathbf{n}}(\infty) = 0$.

Ker je $V''(\overline{\varphi}(\rho))$ simetričen na 4D rotacije, lahko ločimo radialni in orbitalni del $\psi_{\mathbf{n}}$, pri čemer je slednji opisan s hipersferičnimi harmoniki. Ti so lastne funkcije operatorja celotne orbitalne vrtilne količine s kvantnimi števili $l = 0, \ldots, \infty$, ki so $(l+1)^2$-krat degenerirana [110].

Izkaže se, da se je namesto iskanja lastnih vrednosti $\gamma_{\mathbf{n}}$ lažje opreti na Gel'fand-Yaglomov teorem [194], ki poveže razmerje determinant z razmerjem lastnih funkcij, izvrednotenih v limiti $\rho \to \infty$. Najti moramo torej lastne načine fluktuacijskega operatorja

$$\mathcal{O}_l\psi_l = -\ddot{\psi}_l - \frac{3}{\rho}\dot{\psi}_l + \frac{l(l+2)}{\rho^2}\psi_l + V''\left(\overline{\varphi}\right)\psi_l = 0, \tag{7.17}$$

ki dajo logaritem razmerja determinant

$$\ln\left(\frac{\det\mathcal{O}}{\det\mathcal{O}^{\mathrm{LV}}}\right) = \sum_{l=0}^{\infty}\left(l+1\right)^2 \ln\mathcal{R}_l\left(\infty\right), \qquad \mathcal{R}_l \equiv \frac{\psi_l}{\psi_l^{\mathrm{LV}}}, \tag{7.18}$$

kjer lahko robne pogoje za ψ prepišemo kot $\mathcal{R}_l(0) = 1$ in $\mathcal{R}_l'(0) = 0$.

Diferencialna enačba (7.17) je preprosta in enostavno numerično integrabilna za vsak kotni način l. A vseh ne moremo naivno izračunati numerično, saj se v l raztezajo do neskončnosti in potrebujemo vse, da lahko izvedemo renormalizacijo ultravijoličnih divergenc. V literaturi so numerične metode, ki razrešijo te težave za katerikoli renormalizabilen in gladek potencial [69, 97, 98, 99, 100, 101]. Obstajajo tudi zaključeni izrazi za predfaktor, a le za nekaj zelo posebnih primerov: limito tankega zidu [102, 103] (glej tudi [104]) in potencial kvartičnega tipa [9, 105].

Mi prispevamo k skromnemu naboru zaključenih rešitev z analitičnim izračunom rešitve bikvartičnega potenciala in tako najdemo prvo analitično rešitev potenciala z dvema ločenima minima na drevesnem redu. Ta rešitev dá enostaven rezultat za fluktuacijsko determinanto

$$\mathcal{R}_l(\infty) = \frac{(l-1)(l^3 + c_2 l^2 + c_1 l + c_0)}{(l+1)(l+2)^2(l+3)}\,, \tag{7.19}$$

s tremi koeficienti c_i, ki so odvisni le od brezdimenzijskih razmerij x in y: $c_0 = \frac{12(1+x)^2x^4y(1+x^3y)^2}{(x^4y-1)^3}$, $c_1 = \frac{2x\big(1+(1+2x)x^2y\big)\big(2+3x+(3+4x)x^3y\big)}{(x^4y-1)^2}$, $c_2 = \frac{1+4x+(4+7x)x^3y}{x^4y-1}$.

Vsi c_i so realni in pozitivni, saj je $x^4y > 1$, kar sledi iz konstrukcije potenciala. Kot smo že omenili pri enačbi (7.15), predfaktor vključuje reducirano determinanto in moramo odstraniti štiri ničelne lastne vrednosti, ki ustrezajo translacijski invarianci. Reducirani prispevek načinov z $l = 1$ je definiran kot

$$\mathcal{O}_l\psi_l = \gamma_n\psi_l \implies \mathcal{R}_1'(\infty) = \frac{\prod_{n=2}^{\infty}\gamma_n}{\prod_{n=1}^{\infty}\gamma_n^{\mathrm{LV}}}\,. \tag{7.20}$$

Ta postopek je enostavno izvesti, ko so γ_n znane za glavna kvantna števila n, a z Gel'fand-Yaglomovim pristopom so lastne vrednosti razvrščene glede na orbitalne l načine. Zaradi tega je treba ničlo, ki izhaja iz translacij, previdno odstraniti, saj pomnoži vse druge lastne vrednosti pri $l = 1$. To se lahko izvede perturbativno [9, 182, 183, 193], tako da zamaknemo fluktuacijski potencial z majhnim dimenzionalnim parametrom μ_ε^2 in poiščemo pripadajoče lastne funkcije:

$$\left(\mathcal{O}_1 + \mu_\varepsilon^2\right)\psi_1^\varepsilon = 0\,. \tag{7.21}$$

Potem je razmerje determinant namesto padanja proti 0 podano z

$$\mathcal{R}_1^\varepsilon(\infty) = \frac{\psi_1^\varepsilon(\infty)}{\psi_{\mathrm{LV}1}(\infty)} \simeq \frac{(\mu_\varepsilon^2+\gamma_1)\prod_{n=2}^{\infty}\gamma_n}{\prod_{n=1}^{\infty}\gamma_n^{\mathrm{LV}}} = \mu_\varepsilon^2\mathcal{R}_1'(\infty)\,, \tag{7.22}$$

saj zamik μ_ε^2 ne spremeni $\gamma_{n>1}$ in γ_n^{LV}. Reducirani prispevek je tako

$$\mathcal{R}_1'(\infty) = \lim_{\mu_\varepsilon^2\to 0}\frac{1}{\mu_\varepsilon^2}\mathcal{R}_1^\varepsilon(\infty) = \frac{R_2^2}{24}\left(\frac{3\lambda}{8\pi^2}\right)\mathcal{S}_0x^6y^2\,, \tag{7.23}$$

kjer je R_2 znan iz odbojnega polja, izračunanega v (2.41).

Zdaj, ko smo odstranili ničlo pri $l = 1$, lahko nadaljujemo in določimo končni del $\mathcal{R}_l$ iz (7.18) ter renormaliziramo pričakovano ultravijolično obnašanje za velike l. V ta namen obravnavajmo generično obliko $\mathcal{R}_l$, dano z razmerjem polinomov reda n kot

$$\mathcal{R}_l(\infty) = \prod_{i=1}^{n}\frac{l+1-a_i}{l+1-b_i}\,, \tag{7.24}$$

ki krije rezultate iz (7.19) dokaj splošno. Števili ničel in polov morata biti enaki zaradi normalizacije LV v (7.18). Da določimo končni del (7.18), najprej poiščimo asimptotsko obnašanje $\mathcal{R}_l$ z razvojem logaritma determinante za velike l. Faktor degeneracije raste kot l^2, zato moramo $\ln\mathcal{R}_l$ razviti do reda $1/l^3$, da upoštevamo kvadratične, linearne in logaritemske divergence.

Izkaže se, da bo asimptotika zeta funkcije, uporabljene za renormalizacijo, dana v potencah $\nu = l + 1$, zato je priročno definirati $\mathcal{R}_l^a$ z razvojem (7.18) v $1/\nu$ do $\mathcal{O}(\nu^{-3})$. To odštejemo od (7.18) in dobimo

$$\Sigma_f = \sum_{\nu=1}^{\infty} \nu^2 \left(\ln \mathcal{R}_l(\infty) - \ln \mathcal{R}_l^a(\infty)\right), \tag{7.25}$$

kar je konvergentno in izrazljivo v zaključeni obliki

$$\begin{aligned}\Sigma_f = \sum_{i=1}^{n} \Bigg(& \frac{a_i^3}{3}\gamma_E - \frac{a_i}{12}\left(1 + 3a_i - 6a_i^2\right) - \zeta_R'\left(-2, 3 - a_i\right) - 2a_i\zeta_R'\left(-1, 3 - a_i\right) \\ & - a_i^2\zeta_R'\left(0, 3 - a_i\right) - (a \to b)\Bigg) + \ln \mathcal{R}_0(\infty) + 4 \ln \mathcal{R}_1'(\infty)\,.\end{aligned} \tag{7.26}$$

Tu je $\zeta_R'(s, a)$ odvod generalizirane Riemannove zeta funkcije po s, γ_E pa je Eulerjeva konstanta.

Sedaj moramo najti asimptotske člene $\mathcal{R}_l^a$, ki smo jih odšteli v (7.25). V ta namen uporabimo regularizacijo z zeta funkcijo [110, 196, 197, 198, 199, 200, 201], pri kateri je renormalizacija izvedena z analitičnim nadaljevanjem te funkcije, ki izhaja iz njene analitičnosti. Ta postopek poveže logaritem funkcijske determinante z odvodom zeta funkcije kot

$$\ln\left(\frac{\det \mathcal{O}}{\det \mathcal{O}_{\mathrm{LV}}}\right) = -\zeta'(0) = -\zeta_f'(0) - \zeta_a'(0)\,. \tag{7.27}$$

Končni člen bikvartičnega potenciala smo že izvrednotili v (7.26): $-\zeta_f'(0) = \Sigma_f$, asimptotski renormalizirani člen $\zeta_a'(0)$ pa je dan z

$$\begin{aligned}\zeta_a'(0) = & \sum_s \frac{1}{8}\int_0^{\infty} \mathrm{d}\rho\, \rho^3 V_s''^2 \left(\ln\left(\frac{\mu\rho}{2}\right) + \gamma_E + 1\right) H\left((-1)^s(\rho - R_T)\right) \\ & - \frac{\left(\mu_V R_T\right)^2}{16} + \frac{\left(\mu_V R_T\right)^3}{24}\left(1 - \frac{3}{\mu_V^2}\left(V_1'' + V_2''\right)\Big|_{R_T}\right)\left(\ln\left(\frac{\mu R_T}{2}\right) + \gamma_E + 1\right).\end{aligned} \tag{7.28}$$

kjer je μ renormalizacijska skala. Odvod bikvartičnega potenciala tu sledi iz (2.40):

$$V'' = V_s''(\rho) H\left((-1)^s(\rho - R_T)\right) - \mu_V \delta(\rho - R_T)\,, \tag{7.29}$$

kjer je $V_s'' = 3(\lambda_s(\overline{\varphi} - (-1)^s v_s)^2)$, $\overline{\varphi}_s = (-1)^s v_s + \sqrt{8/\lambda_s} R_s/\left(R_s^2 - \rho^2\right)$ in $\mu_V = \left(\lambda_1 v_1^3 + \lambda_2 v_2^3\right)/\dot{\overline{\varphi}}(R_T)$. Delta funkcija tukaj pride iz nezveznosti V' v izhodišču. Ti rezultati se strinjajo z (5.12) za zvezen V'' z $\mu_V = 0$ in $V_{\mathrm{LV}}'' = 0$ ter tudi poustvarijo SM [9] v primeru navadnega kvartičnega potenciala. To pokaže, da se pristop s Feynmanovimi diagrami ujema s formalizmom zeta funkcije.

Netrivialen način za kontrolo pravilnosti rezultatov se tiče krajšanja divergenc, zato preverimo, da se v Σ_f, podani s (7.26), členi, ki so sorazmerni γ_E, res odštejejo s tistimi v $\zeta_a'(0)$ zgoraj.

Končni rezultat za celotno rapadno širino na enoto 4D volumna je

$$\frac{\Gamma}{\mathscr{V}} = \left(\frac{\mathcal{S}_0}{2\pi}\right)^2 e^{-\mathcal{S}_0 + \frac{1}{2}\zeta'(0)}\,, \tag{7.30}$$

kjer $\mathcal{S}_0$ pride iz (2.42), $\zeta'(0)$ pa je vsota (7.26) in (7.28). Zaključena oblika tega rezultata je posebej uporabna pri študiju obnašanja razpadne širine v limiti tanke stene, pa tudi za separacijo $x \gg 1$ pri velikih skalah, ki ustreza dokaj ploščatemu potencialu.

7.5 Sklepne opombe

V tej disertaciji smo razširili razumevanje razpada lažnega vakuuma v treh vidikih, tako konceptualnih kot praktičnih. Vsebuje novo metodo za izračun odbojev v večpoljskih potencialih, uporabniku prijazen `Matematica` paket in izvrednotenje prispevkov višjega reda k predfaktorju z rezultatom v zaključeni obliki.

Metoda poligonskih odbojev nudi analitičen vpogled v večpoljske fazne prehode vakuuma in predfaktorja. Njen robusten pristop se izogne običajni popolnoma numerični strelski metodi z uporabo nabora analitičnih rešitev, ki aproksimirajo potencial do željene natančnosti, zato je izračun odboja bolj stabilen kot z drugimi paketi, ki so na voljo v literaturi, še posebej v limiti tanke stene, kjer popolnoma numerične metode odpovedo.

Izdali smo `Mathematica` paket, imenovan `FindBounce`, ki izračuna odbojno akcijo pri natančnosti 1% v 3 sekundah za potencial z 20 polji. Konkurečen je drugim programom, ki so na voljo, nudi pa izgled in občutek okolja `Mathematica` ter vsebuje zbirko enostavnih primerov in primerjalnih ter časovnih merilnih orodij. Semi-analitične izhodne podatke paketa `FindBounce` lahko izkoristimo, da tudi predfaktor in poznejši razvoj mehurčka dobimo semi-analitično.

Na koncu smo se osredotočili na kvantne korekcije razpadne širine vakuuma. Ugotovili smo, da je treba vključiti prispevke, da dobimo konsistenten in natančen izračun mehurčka nukleacije. Predstavili smo prvi popoln analitičen rezultat do nivoja ene zanke za razpadno širino v potencialu z dvema minima na drevesnem redu z uporabo bikvartičnega potenciala. Pokazali smo, da izračun prefaktor za nekatere razpone parametrov postane neperturbativen, ko imamo opravka z veliko separacijo skal.

Zgornji rezultati so fundamentalni v mojem trenutnem napredovanju proti splošni semi-analitični metodi izračuna predfaktorja za poljuben potencial in razširitvi paketa `FindBounce` s funkcionalnostjo za izračun spektra gravitacijskih valov v širokem naboru modelov onkraj SM.

List of publications related to this doctoral thesis

Articles:

1. **V. Guada**, A. Maiezza and M. Nemevšek, "MultiField Polygonal Bounce," Phys. Rev. D **99**, no. 5, 056020 (2019), doi:10.1103/PhysRevD.99.056020, [arXiv:1803.02227 [hep-th]].
2. **V. Guada**, M. Nemevšek and M. Pintar, "FindBounce: package for multifield bounce actions," Comput. Phys. Commun. **256** (2020), 107480, doi:10.1016/j.cpc.2020.107480, [arXiv:2002.00881 [hep-ph]].
3. **V. Guada**, and M. Nemevšek, "An exact false vacuum decay rate," Phys. Rev. D **102** (2020), 125017 doi:10.1103/PhysRevD.102.125017 [arXiv:2009.01535 [hep-th]].

Conferences:

1. **V. Guada**, "Multifield False Vacuum Decay: Polygonal Bounce," Acta Phys. Polon. B **50**, 1859 (2019), doi:10.5506/APhysPolB.50.1859.